

Numerisk modellering af formfyldning ved støbning i selvkompakterende beton

Spangenberg, Jon; Geiker, Mette Rica; Hattel, Jesper Henri; Stang, Henrik

Publication date:
2012

Document Version
Også kaldet Forlagets PDF

[Link back to DTU Orbit](#)

Citation (APA):

Spangenberg, J., Geiker, M. R., Hattel, J. H., & Stang, H. (2012). Numerisk modellering af formfyldning ved støbning i selvkompakterende beton. Kgs. Lyngby: Technical University of Denmark (DTU).

DTU Library

Technical Information Center of Denmark

General rights

Copyright and moral rights for the publications made accessible in the public portal are retained by the authors and/or other copyright owners and it is a condition of accessing publications that users recognise and abide by the legal requirements associated with these rights.

- Users may download and print one copy of any publication from the public portal for the purpose of private study or research.
- You may not further distribute the material or use it for any profit-making activity or commercial gain
- You may freely distribute the URL identifying the publication in the public portal

If you believe that this document breaches copyright please contact us providing details, and we will remove access to the work immediately and investigate your claim.

Preface

This work was carried out at the Department of Mechanical Engineering (MEK) at the Technical University of Denmark (DTU), during the period 2009-2012. The work was funded by the Danish Agency for Science Technology and Innovation (project 09-065049/FTP: Prediction of flow induced inhomogeneities in self-compacting concrete). The work was supervised by Professor Jesper H. Hattel (MEK)(DTU), co-supervised by Professor Mette R. Geiker, Department of Civil Engineering (BYG)(DTU) and Department of Structural Engineering, Norwegian University of Science and Technology, and Professor Henrik Stang (BYG)(DTU).

I would like to express my deepest gratitude to Professor Hattel for his excellent guidance, for his motivating talks, and for his helpfulness throughout my entire study. I would also like to thank Professor Geiker for the fruitful discussions and Professor Stang for his support during all my studies at DTU.

A special thanks go to Professor Nicolas Roussel from Laboratoire Central des Ponts et Chaussées, Université Paris Est, who undoubtedly has been my fourth unofficial supervisor. His indispensable contributions improved significantly the quality of this work. Moreover, I would like to express my special gratitude to Dr. Cem C. Tutum for being highly inspirational and helpful from first encounter.

My thanks goes also to the other people involved in the FTP-project: Prediction of flow induced inhomogeneities in self-compacting concrete. Furthermore, I would like to thank Dr. Jesper Thorborg and Jens Ole Frandsen for helping out with any kind of support and the rest of my colleagues in the process modelling group at (MEK) for providing an incredible working environment.

Finally, I would like to thank my family, friends and girl friend, without your support this work would never have been possible.

Abstract

The present thesis deals with numerical modelling of form filling with Self-Compacting Concrete (SCC). SCC differs from conventional concrete by its increased fluidity, which enables it to fill out the form work without any vibration. The benefits of casting with SCC as compared to conventional concrete may be a decreased construction time and a better working environment if the SCC is managed properly. However, also obstacles may arise from casting with SCC such as issues related to robustness, form work pressure, static segregation and flow induced aggregate migration, thus numerical modelling of form filling with SCC includes a lot of topics. In this thesis it is chosen to focus on the following three topics by the usage of Finite Difference Method (FDM) / Finite Volume Method (FVM) based Computational Fluid Dynamics (CFD) models developed in both FLOW-3D and MATLAB.

The first investigation focussed on the complications involved with modelling a yield stress fluid with a bi-viscosity material model, which is a typical material model used when capturing the non-Newtonian flow behaviour of SCC. The study was carried out by comparing the numerical result and the yield stress based analytical solution of the LCPC-box test. The comparison showed that a relatively good agreement was obtained for both the FLOW-3D and MATLAB model. In addition, the study identified that the agreement improved when the initial viscosity was increased, thus it was impossible for the applied numerical models to be in full agreement with the analytical solution. Based on the investigation it was also found that the LCPC-box test is a highly recommended test to carry out in order to get a better understanding of the numerical settings' implication for a given CFD solver.

Following this, two numerical approaches were developed to investigate their capability of predicting gravity induced aggregate migration in SCC castings. The two FDM/FVM based CFD models differentiated from each other by their aggregate representation, which was a discrete approach (one way momentum coupling) for one of them and a scalar approach for the other. It was found that it was less complicated to implement criteria for the model with the scalar aggregate representation. Subsequently, experimental results from an SCC-like model fluid casting and a real SCC casting were compared with numerical results from the model with the scalar aggregate representation and showed a good agreement. In the case of the SCC though, it was found out that a coupling back from the aggregates to the rheological parameters of the SCC was needed. The study showed also an obstacle for the scalar approach which was the need of a parameter dictating the viscosity of the surrounding fluid in which the aggregate settled. The parameter did not seem to change when changing the casting velocity, but only a future study will show how it changes with different mix compositions of the SCC and thereby finally judge the potential of numerically predicting gravity induced aggregate migration with this scalar

approach.

Finally, a single objective genetic algorithm was coupled to the numerical model with the scalar aggregate representation in order to investigate its applicability. Two studies were carried out with the objective to obtain a homogeneous aggregate distribution in a beam SCC casting. The primary difference between the two studies was the implementation of constraints that enabled more realistic and usable casting scenarios to be found. In both studies non-trivial casting scenarios were obtained, which indicated that the coupling between a numerical model capable of predicting gravity induced aggregate migration and an optimization algorithm can be a useful tool. An obstacle for the numerical model used in this study is the calculation time. In the case of evaluating a large vertical casting it was found that the simulation most likely would be too time consuming to finish the optimization study in a reasonable time, but that an algorithm which splits the pressure and velocity calculation may give the necessary calculation speed up.

Resumé

Denne afhandling omhandler numerisk modellering af formfyldning med Selv Kompakterende Beton (SKB). SKB er mere flydende end konventionel beton, hvilket gør at den fylder formen ud uden nogen form for vibration. Fordelene ved at støbe med SKB i forhold til konventionel beton er at konstruktionstiden kan reduceres og arbejdsmiljøet forbedres, hvis SKBen bliver korrekt behandlet. Forhindringer relateret til robusthed, formtryk, statisk separation og separation under flydning kan dog også opstå, når der støbes med SKB, og det betyder, at numerisk modellering af formfyldning med SKB i realiteten dækker over mange emner. I denne afhandling er der fokuseret på tre af dem ved hjælp af Finite Difference Method (FDM) / Finite Volume Method (FVM) baserede Computational Fluid Dynamics (CFD) modeller udviklet i både FLOW-3D og MATLAB.

Den første undersøgelse fokuserer på de komplikationer der er knyttet til at modellere en flydespændings fluid med en bi-viskositets materiale model, som er den typiske materiale model der benyttes til at simulere den ikke Newtonske flyde opførsel af SKB. Studiet blev udført ved at sammenligne numeriske resultater med den flydespændingsbaserede analytiske løsning for LCPC-box testen. Sammenligningen viste, at der kunne opnås en relativ god overensstemmelse for både FLOW-3D og MATLAB Modellen. Ydermere fandt studiet, at overensstemmelsen blev forbedret når begyndelses viskositeten, blev forøget, hvilket derved umuliggjorde at de numeriske modeller kunne være i fuld overensstemmelse med den analytiske løsning. På basis af undersøgelsen kunne det også konkluderes, at det kan anbefales at udføre denne test for at få en bedre forståelse for hvilke numeriske indstillinger, som virker for en given CFD løser.

Derefter blev to numeriske metoder udviklet for at undersøge deres evne til at forudsige separation under fyldning i SKB støbninger. De to FDM/FVM baserede CFD modeller afviger fra hinanden via deres tilslags repræsentation, som var en diskret metode (envejs momentum kobling) for den første og en skalar metode for den anden. Det viste sig, at det var mindst omfattende at implementere et maksimum tilslags krav og en tilbage kobling fra tilslaget til de rheologiske parametre for modellen med skalar tilslags representationen. Dernæst blev eksperimentelle resultater fra en SKB lignende fluid støbning og en rigtig SKB støbning sammenlignet med numeriske resultater fra modellen med skalar tilslags repræsentation og sammenligningen viste en god overensstemmelse. For den rigtig SKB støbning blev det vist at det var nødvendigt at anvende en tilbagekobling fra tilslaget til de rheologiske parametre af SKB'en. Studiet viste også en komplikation for den skalar baserede metode, som var behovet for at anvende en parameter der dikterer viskositeten af den omkringliggende fluid, hvori tilslaget flyder. Parameteren ændrede sig ikke med støbehastigheden, men kun et fremtidigt studie vil vise hvordan den ændrer sig med skiftende SKB blandinger og derved endeligt afgøre potentialet for den numeriske model, der regner på separation under flydning med skalar metoden.

Endeligt, blev en genetisk algoritme koblet med den numeriske model med skalartilslagsmetoden for at undersøge dens anvendelighed. To studier blev udført med målsætningen om at opnå en homogen tilslagsfordeling i en SKB bjælke støbning. Den primære forskel mellem de to studier var implementeringen af restriktioner som gjorde de undersøgte støbescenarier mere realistiske. I begge studier blev ikke-trivielle støbe scenarier fundet, der derved indikerede at koblingen mellem en numerisk model som kan forudse separation under formfyldning og en optimeringsalgoritme kan være et brugbart redskab. En udfordring for den numeriske model anvendt i dette studie er beregningstiden. Det blev konkluderet, at det var for tidskrævende at simulere store vertikal støbninger, men at en algoritme som splittede tryk og hastighedsudregningen højst sandsynligt ville give den fornødne forøgelse af beregningshastigheden.

Table of Contents

1	Introduction	1
1.1	Self-Compacting Concrete	1
1.2	Numerical Methods for Modelling Flow of fresh concrete/SCC	4
1.2.1	Homogeneous Approach	4
1.2.2	Discrete Approach	4
1.3	Objective	5
1.4	Structure of the Thesis	7
2	Theory	9
2.1	Governing Equations	9
2.1.1	Mass Conservation	9
2.1.2	Momentum Conservation	10
2.1.3	Pressure Equation	11
2.2	Rheological Models	11
2.2.1	Bingham Material Model	12
2.2.2	Bi-viscosity Material Model	12
2.2.3	Herschel-Bulkley Material Model	13
2.3	Aggregate Settling Equation	14
2.3.1	Single Spherical Particle in Newtonian Fluid	14
2.3.2	Single Spherical Particle in non-Newtonian Fluid	16
2.4	The Aggregate Volume Fraction's Effect on Rheological Parameters	16
3	Modelling	19
3.1	FLOW-3D Models	19
3.1.1	Solver	19
3.1.2	Free Surface Algorithm	21
3.1.3	Settling Calculation	22
3.1.3.1	FLOW-3D Model #1	22
3.1.3.2	FLOW-3D Model #2	23
3.2	MATLAB Model	25
3.2.1	Solver	25
3.2.2	Free Surface Algorithm	27
3.2.3	Settling Calculation	29
3.2.4	Rheological Parameter Calculation	29
4	Single Fluid Analysis	31
4.1	LCPC-Box Test	31
4.2	Three Dimensional Analytical Solution	32

4.3	2D Analytical Solution	33
4.4	FLOW-3D Model	34
4.4.1	Comparison with Analytical Solution	35
4.4.2	Material Law and Convergence Test	36
4.4.2.1	Mesh Density Analysis	36
4.4.2.2	Time Step Analysis	37
4.4.2.3	Initial Viscosity Analysis	37
4.5	MATLAB Model	38
4.5.1	Comparison with Analytical Solution	38
4.5.2	Material Law and Convergence Test	39
4.5.2.1	Mesh Density Analysis	39
4.5.2.2	Time Step Analysis	39
4.5.2.3	Initial Viscosity Analysis	39
4.6	Remarks on LCPC-Box Test	40
5	Applications with Aggregate Migration	41
5.1	Discrete Aggregate Representation (FLOW-3D Model #1, Paper I)	41
5.2	Scalar Aggregate Representation	44
5.2.1	Carbopol Test (FLOW-3D Model #2, Paper II)	44
5.2.2	SCC Test (MATLAB Model, Paper III)	48
5.3	Optimization	55
5.3.1	Feasibility Study (FLOW-3D Model #2, Paper IV)	56
5.3.2	Case Study (MATLAB Model, Technical Report - II)	60
6	Summary of Appended Papers	65
6.1	Paper - I	65
6.2	Paper - II	65
6.3	Paper - III	66
6.4	Paper - IV	66
6.5	Technical Report - I	66
6.6	Technical Report - II	66
7	Conclusion and Future Work	69
	Bibliography	71
	Appendixes	75
A	PAPER-I	77
B	PAPER-II	87
C	PAPER-III	99
D	PAPER-IV	135
F	TECHNICAL REPORT-I	145
F	TECHNICAL REPORT-II	167

Chapter 1

Introduction

This chapter presents an introduction to the thesis: Numerical simulation of form filling with Self-Compacting Concrete (SCC). In order to understand what SCC is, how it deviates from conventional concrete and which practical applications it is used for, a short presentation of these topics are given in section 1.1. Afterwards, a short review of the numerical methods previously used to model SCC in different applications are presented in section 1.2, and this is naturally followed by the objective and numerical approach of this thesis, in section 1.3. Finally, section 1.4 gives an overview of the structure of the thesis by a brief description of each of the included chapters.

1.1 Self-Compacting Concrete

Today concrete is the most important construction and building material of the planet with an estimated annual production in excess of 6 billion cubic metres (rilem.net, 2012). Concrete is produced by sand, stones, water, cementitious binders, and in some cases fly ash and silica fume. A reaction between the water and the binders enables the mixture to harden into a stone like material. Chemical admixtures may as well be added to control e.g. the workability, early strength development, and the air void distribution. Casting of conventional concrete includes a placement and a vibration process. The vibration process is performed to force the coarse aggregates into a closer configuration and to avoid entrapped air. Thereby, it ensures the hardened concrete to meet its requirements regarding material properties such as strength and durability (Neville, 1995).

According to Okamura and Ouchi (2003), in the 1980s the durability of the concrete structures was of special interest in Japan, since the number of skilled workers able to perform the adequate compaction by vibration were gradually decreasing. It was found that a solution to the durability problem which was independent on construction work was the usage of a new type of concrete called SCC. The SCC was capable of filling the formwork fully under its own weight without any vibration compaction.

The primary difference between SCC and conventional concrete is the increased fluidity, which today is obtained by the addition of a so called superplasticizer. The attractive forces between cement particles in water are reduced by the addition of superplasticizers, which act by a combination of electrostatic forces and steric hindrance (Houst et al., 2008). The increased fluidity entails both benefits and obstacles.

The benefits of applying SCC instead of conventional concrete:

- The risk of getting non-filled zones, poor compaction, and inhomogeneous air void structure is lower (Thrane, 2007).
- The number of workers needed for the casting process is reduced if the SCC is managed properly. The workers no longer required for casting can perform other production tasks instead of vibrating the concrete (Simonsson, 2011).
- The working environment improves, since the elimination of the vibration process reduces the noise level and the need for lifting of heavy equipment (Simonsson, 2011). These prevention efforts are important in Denmark where thousands of construction workers are injured every year (Spangenberg, 2010).
- The structural designs can be more geometrically challenging, since there is no need for vibration in inaccessible areas of the form (Thrane, 2007).

The obstacles for applying SCC instead of conventional concrete:

- The increased workability may result in large formwork pressures in vertical applications (Billberg, 2003).
- SCC is more susceptible to static segregation than conventional concrete (Shen et al., 2009). Static segregation is the physical phenomenon occurring when the aggregates settle while the concrete is at rest.
- The dynamic segregation resistance is also an obstacle for SCC (Geiker, 2008). Dynamic segregation is an expression which refers to when aggregates settle during flow of the concrete. In the rest of the thesis this physical phenomenon is referred to as "flow induced aggregate migration".
- The robustness is also a critical topic for SCC. The robustness in terms of SCC is the insensitivity against fluctuations of the concrete components, mixing procedure and transport conditions (Simonsson, 2011).

The practical applications SCC can be used for are similar to the ones of conventional concrete, cf. Fig. 1.1. However, SCC is especially suitable for some casting applications such as vertical casting (walls or columns) since workers are not forced to climb into the form to perform the vibration process, which may be the case when using conventional concrete (voscc.net, 2012). Even though the applications are the same and the benefits of using SCC are many, the obstacles are still limiting the usage. According to Simonsson (2011), the market share of SCC in EU as a whole is less than 10%. In Denmark specifically, the market share is approximately 25%, which is quite high as compared to other countries like Sweden or France where it is about 10% and 3%, respectively. When comparing the SCC market share in pre-cast production with the market share in in-situ castings, the former is greater than the latter in most countries. One of the reasons for that is the elimination of the transportation (less robustness issues').



Figure 1.1: *Different applications with SCC, courtesy of Bernt Kristiansen.*

1.2 Numerical Methods for Modelling Flow of fresh concrete/SCC

There are several different numerical methods which have been used for modelling of flow of fresh concrete or SCC and in the next two subsections some of them are presented. Undoubtedly, each one of them have advantages and drawbacks, however, these are not presented and commented here, primarily because the most fair comparison would need the programming know-how for each of the approaches. Nevertheless, this brief review puts the numerical simulations presented in this thesis into perspective. As seen in the following, the numerical methods are divided into the categories; homogeneous approaches and discrete approaches. The homogeneous approaches include methods where the fresh concrete/SCC is considered as a homogeneous fluid, while the discrete approaches cover methods where particles are included either for discretization purposes or for representation of aggregates.

1.2.1 Homogeneous Approach

Finite Element Method (FEM)

- The FEM typically uses weighted residual methods together with shape functions to discretize a continuous flow problem. Thrane (2007) used the software FIDAP which solves the Navier Stokes equations with a variant of FEM to simulate the L-box test, but also to investigate flow patterns inside a full scale SCC casting of a wall. Also, Dufour and Pijaudier-Cabot (2005) used the FEM with Lagrangian integration points to model the L-box test.

Finite Difference Method (FDM) / Finite Volume Method (FVM)

- In classical FDM the methodology is to replace the derivatives with finite differences found from typically Taylor series expansion, while in FVM the discretized equation is obtained by integration over the volume it is valid for and applying linear schemes for derivatives. With the right assumption it is often possible to reach the same final discretized equation for both methods, therefore it is not always explicitly specified in commercial software which method is used in a given case. Roussel (2006c) developed numerical models to study multi-layer casting phenomena, to simulate slump test (Roussel and Coussot, 2005), and to investigate the minimum fluidity in a high strength concrete pre-cambered composite beam (Roussel et al., 2007b) in the software FLOW-3D¹ which uses FDM/FVM. Recently, Vasilic et al. (2011) studied flow of fresh concrete through steel bars with a porous medium analogy with the software Fluent.

1.2.2 Discrete Approach

Discrete Element Method (DEM)

- According to Roussel et al. (2007a), the DEM includes the calculation of the contact forces between solid particles and the motion of each particle by the usage of Newton's second law. The DEM was originally developed for analysing the behaviour of granular material, but has afterwards also been used to simulate different concrete

¹FLOW-3D is a registered trademark of Flow Science

applications, e.g. Noor and Uomoto (1999) used the method to simulate rheological tests for SCC, such as the slump flow, L1-box, U-box and V-funnel test. Also, Gram and Silfwerbrand (2011) used the DEM to simulate different application for instance investigation of blocking in SCC by modelling of the J-Ring.

Dissipative Particle Dynamics (DPD)

- The DPD captures the behaviour of non-Newtonian fluids by mesoscopic particles which represent clusters of molecules. The total force acting on each particle is obtained by a sum of the contributing forces from the surrounding particles. E.g. when relating to SCC these particles represent the mortar, while several particles "frozen" together represent individual aggregates. Martys and Ferraris (2002) used this stochastic simulation technique to simulate SCC flow around reinforcement bars, while Ferraris and Martys (2003) used it for investigating fresh concrete viscosity in different rheometers.

Viscoplastic Suspension Element Method (VSEM)

- Mori and Tanigawa (1992) demonstrated the applicability of VSEM to simulate the flow of fresh concrete with a three dimensional simulation of a model fluid in a simple test set-up. In addition, two dimensional numerical models were used to simulate the slump flow test, an L-type flow test, a vibrating box test, a casting into a reinforced concrete beam form work (height-width cross section), and a casting into a reinforced concrete wall form work (height-width cross section). The applied numerical method calculated the suspending phase with rheological parameters of mortar and the interaction between solid spherical particles (aggregates) with a viscoplastic formulation.

Lattice Boltzmann Method (LBM)

- Recently, Skocek et al. (2011) developed a numerical model with the use of the LBM to predict the casting process of SCC. The model considered the suspending fluid with LBM which treats the fluid as individual molecules discretized by a set of discrete particle distribution functions and provides rules for their mutual collisions and propagation. The macroscopic quantities can then be computed as moments of the distribution functions. The fluid-particle (aggregate) interaction was taken into account by a force equilibrium which is derived based on the assumption that at the intersection point of the fluid and the particle, they both have the same velocity. In addition, sub-stepping within a time step and an additional force equilibrium where constant forces in each sub-step are assumed, enable the model to consider interaction between particles.

1.3 Objective

In the present thesis, the numerical models are based on the FDM/FVM and they basically include three investigations. In the first investigation the SCC is considered with the homogeneous approach, while in the other two investigations the SCC is considered as a suspension where the aggregates are represented either with a discrete or a continuous (a scalar) representation. In the following the motivation and objective for the three investigations are presented.

Even though several of numerical simulations of flow of fresh concrete/SCC have been successively used to investigate different physical phenomena as seen in the previous section, there are still several undiscovered topics left within the field of 'Numerical simulation of flow of fresh concrete/SCC', e.g. the complication involved with modelling a yield stress material with a bi-viscosity material model. In addition, no 'official' benchmark test for validation of CFD-solvers with regards to flow of concrete/SCC exist. These two facts lead to the objectives of the first investigation:

- 1.1 To analyse the difference between the numerical result of the LCPC-box test when using the FDM/FVM together with a bi-viscosity material model and the analytical solution of the LCPC-box test (Roussel, 2007), which is based on a yield stress material.
- 1.2 To detect the sensitivity of the numerical result of the LCPC-box test by variation of the mesh density, time step, and initial viscosity.
- 1.3 To discuss the LCPC-box test's ability of being a benchmark test in the field of numerical simulation of SCC flow.

The second investigation considers another still unresolved issue which is the numerical prediction of flow induced aggregate migration in SCC form fillings. Flow induced aggregate migration involves shear induced aggregate migration, gravity induced aggregate migration and granular blocking, of which the gravity induced aggregate migration is the dominating source of heterogeneities induced by flow in industrial castings. In this thesis the problem relating to gravity induced aggregate migration is tackled with a simple numerical approach as compared to the fully coupled multi-phase flows. The objective of this investigation is:

- 2 To evaluate the possibility of predicting gravity induced aggregate migration in SCC form fillings both with the usage of an FDM/FVM based numerical model coupled with a discrete aggregate representation (the aggregate 'feels' the fluid, but the fluid does not 'feel' the aggregates) and the usage of an FDM/FVM based numerical model coupled with a scalar aggregate representation.

As a note to this investigation it needs to be mentioned that this thesis includes three numerical models. Two carried out in the commercial software FLOW-3D: one with a discrete aggregate representation called FLOW-3D model #1 and one with a scalar aggregate representation called FLOW-3D model #2. The third numerical model is programmed in the technical computer language MATLAB² and it uses also the scalar aggregate representation. The primary difference between FLOW-3D model #2 and the MATLAB model is that the latter includes the aggregate volume fraction's effect on the rheological parameters. The main reason for developing a model in MATLAB which only differs from the FLOW-3D model by taking one extra physical phenomenon into account is the increased flexibility obtained when working with one's own code.

²MATLAB is a registered trademark of MathWorks

The last investigation is with regards to optimization of form filling with SCC. Numerical models for a wide variety of other processes are coupled with optimization algorithms in order to find best solutions or pattern recognition. Therefore, the objective of the third investigation is:

- 3 To analyse the potential of coupling an optimization code with a numerical model capable of predicting the gravity induced aggregate migration in SCC.

1.4 Structure of the Thesis

This thesis features seven chapters, four papers and two technical reports. The content of the chapters is as follows:

Chapter 1: Introduction

- This chapter gives an introduction to the thesis, by first describing SCC and its application. Afterwards, shortly reviewing the numerical models previously used to analyse different fresh concrete/SCC applications and finally describing the objectives of the three investigations included in this thesis.

Chapter 2: Theory

- The theory chapter presents all the equations the numerical models are based on: The governing equations for the flow simulation, the expressions for the relevant material models, the equations for an aggregate settling in a non-Newtonian fluid, and also the relationships for the aggregate volume fraction's effect on the rheological parameters.

Chapter 3: Modelling

- In this chapter the solver, the formulation of the free surface, and the implementation of the settling calculation for the three FDM/FVM based numerical models are presented. In addition, the implementation of the aggregates volume fraction's effect on the rheological parameters is described for the MATLAB model.

Chapter 4: Single Fluid Analysis

- This chapter includes the results of the first investigation of this thesis where the numerical result and the analytical solution of the LCPC-box test are compared. However, first the derivation of the analytical solutions for the LCPC-box in three and two dimensions are presented. Then, the comparison is carried out both for the FLOW-3D model and MATLAB model along with a mesh density, time step, and initial viscosity analysis. Finally, the potential of the LCPC-box test being a benchmark test for flow of SCC is discussed.

Chapter 5: Applications with Aggregate Migration

- In this chapter the investigation regarding developing a numerical model capable of predicting the gravity induced aggregate migration is described, by presenting the key numerical results in Paper - I (Spangenberg et al., 2010), Paper - II (Spangenberg et al., 2012b), and Paper - III (Spangenberg et al., 2012a). Afterwards, the optimization investigation is presented by introducing the most important points from Paper - IV (Spangenberg et al., 2011) and Technical Report - II.

Chapter 6: Summary of Appended Papers

- A short summary of the four appended papers and the two technical reports are given in this chapter.

Chapter 7: Conclusion and Future Work

- The final chapter of the thesis sums up the conclusions of the three investigations and presents a description of the future perspectives within the field of numerically predicted gravity induced aggregate migration and optimization of SCC form fillings.

Chapter 2

Theory

This theory chapter presents the equations which the three numerical models are based on. First, the governing equations for the flow simulation and the relevant material models are presented. Afterwards, the equations for a simple aggregate (spherical particle) settling in a non-Newtonian fluid is given and finally the relationships for the aggregate volume fraction's effect on the rheological parameters are described.

2.1 Governing Equations

The flow of SCC is non-Newtonian and the governing equations which have to be considered when capturing this flow behaviour for all simulations involved in the present thesis are the mass conservation equation also known as the continuity equation and the momentum conservation equations. In the following three sections, these governing equations are presented and processed in order to obtain the final equations for the velocities and pressure, which are the one actually solved by the CFD-solver. A more detailed description of the governing equations and their different processing procedures are described in (Bingham et al., 2009) and (Hattel, 2005).

2.1.1 Mass Conservation

Conservation of mass means that the mass of a considered volume does not change in time. Mathematically that can be written as:

$$\frac{d}{dt} \int_{\Omega} \rho \, d\Omega = 0. \quad (2.1)$$

Where t is the time, Ω is the volume, and ρ is the density. Applying Reynolds Transport Theorem on Eqn. (2.1) yields:

$$\int_{\Omega} \left\{ \frac{\partial \rho}{\partial t} + \frac{\partial}{\partial x_j} (\rho u_j) \right\} d\Omega = 0 \quad (2.2)$$

Where x_j is the spatial component vector, j is the notation denoting the direction, and u_j is the velocity vector. Eqn. (2.2) is the integral form of the mass conservation. However, the volume size is arbitrary, therefore, the law must also hold point wise in the fluid. Consequently, this leads to the mass conservation on differential form:

$$\frac{\partial \rho}{\partial t} + \frac{\partial}{\partial x_j} (\rho u_j) = 0. \quad (2.3)$$

Eqn. (2.3) can also be written as:

$$\frac{\partial \rho}{\partial t} + u_j \frac{\partial \rho}{\partial x_j} + \rho \frac{\partial u_j}{\partial x_j} = 0 \quad (2.4)$$

In literature it is shown that SCC can be treated as an incompressible fluid, cf. Gram (2009) and Thrane (2007). This assumption is also applied for all simulations involved in this thesis, meaning that the density of the fluid does not change in space and time. The assumption makes Eqn. (2.4) simplify into the divergence of the velocities:

$$\frac{\partial u_j}{\partial x_j} = 0 \quad (2.5)$$

Eqn. (2.5) is used to obtain the equations for the velocities in section 2.1.2 by simplifying the momentum conservation equations and it is also used when deriving an equation for the pressure in section 2.1.3.

2.1.2 Momentum Conservation

Conservation of momentum states that the rate of change of fluid momentum must be balanced by the total force applied to the fluid. The total force is the sum of the contributions from the pressure, the viscous stresses and the gravitational force. The momentum conservation equations thus express a force equilibrium:

$$\frac{d}{dt} \int_{\Omega} \rho u_i \, d\Omega = \int_S T_{ij} n_j \, dS + \int_{\Omega} S_i \, d\Omega \quad (2.6)$$

Where S is the surface, T_{ij} is the stress tensor, and S_i is the gravitational force vector ($S_i = [0, 0, -\rho g]$). Here, the notation i typically denotes a scalar equation for each of the three dimensions. The equations express conservation of momentum along each of the coordinate directions. In order to obtain the momentum conservation equations on differential form, Reynolds Transport Theorem is applied on the left hand side of Eqn. (2.6), which yields:

$$\int_{\Omega} \left\{ \frac{\partial(\rho u_i)}{\partial t} + \frac{\partial}{\partial x_j}(\rho u_i u_j) \right\} d\Omega = \int_S T_{ij} n_j \, dS + \int_{\Omega} S_i \, d\Omega \quad (2.7)$$

Furthermore, the divergence theorem is used to convert the stress term from a surface integral into a volume integral:

$$\int_{\Omega} \left\{ \frac{\partial(\rho u_i)}{\partial t} + \frac{\partial}{\partial x_j}(\rho u_i u_j) \right\} d\Omega = \int_{\Omega} \frac{\partial T_{ij}}{\partial x_j} \, d\Omega + \int_{\Omega} S_i \, d\Omega \quad (2.8)$$

Finally, the same argument as in the previous section regarding the arbitrary volume is used to transform the mass conservation equation from integral to differential form:

$$\frac{\partial(\rho u_i)}{\partial t} + \frac{\partial}{\partial x_j}(\rho u_i u_j) = \frac{\partial T_{ij}}{\partial x_j} + S_i \quad (2.9)$$

The stress tensor includes the pressure and the viscous stresses:

$$T_{ij} = - \left(p + \frac{2}{3} \mu \frac{\partial u_k}{\partial x_k} \right) \delta_{ij} + \mu \left(\frac{\partial u_i}{\partial x_j} + \frac{\partial u_j}{\partial x_i} \right) \quad (2.10)$$

Where $k = 1, 2, 3$ and δ_{ij} is the Kronecker delta function. Eqn. (2.10) simplifies into the following when applying the statement that the divergence of the velocities is equal to zero, see Eqn. (2.5):

$$T_{ij} = -p\delta_{ij} + \mu \left(\frac{\partial u_i}{\partial x_j} + \frac{\partial u_j}{\partial x_i} \right) = -p\delta_{ij} + \tau_{ij} \quad (2.11)$$

Where the viscous stresses are:

$$\tau_{ij} = \mu \left(\frac{\partial u_i}{\partial x_j} + \frac{\partial u_j}{\partial x_i} \right) \quad (2.12)$$

The momentum conservation equations can now be rewritten into:

$$\rho \frac{\partial u_i}{\partial t} + \rho \frac{\partial (u_i u_j)}{\partial x_j} = -\frac{\partial p}{\partial x_i} + \frac{\partial \tau_{ij}}{\partial x_j} + S_i \quad (2.13)$$

Eqns. (2.13) form the equations which after the discretization process allow for the velocities to be obtained.

2.1.3 Pressure Equation

As mentioned in the previous section the momentum equations are a set of three equations. However, they involve four unknowns; three velocities (one for each dimension) and the pressure. Therefore, it is of interest to find the pressure by another equation. The procedure enabling the pressure to be found in the case of the MATLAB model is presented in this section, whereas the procedure used for the FLOW-3D models is shortly described in section 3.1.1. The pressure equation is found by taking the divergence of the momentum equations and invoking continuity. Note that Eqns. (2.13) is divided by ρ and that all the terms are moved to the left hand side.

$$\frac{\partial}{\partial x_i} \left(\frac{\partial u_i}{\partial t} + \frac{\partial u_i u_j}{\partial x_j} - \frac{1}{\rho} \frac{\partial \tau_{ij}}{\partial x_j} + \frac{1}{\rho} \frac{\partial p}{\partial x_i} - \frac{1}{\rho} S_i \right) = 0 \quad (2.14)$$

By assuming that the velocities are continuous functions of time the spatial and temporal derivatives can be interchanged to eliminate the time derivative terms using the statement that the divergence of the velocities are equal to zero, cf. (Bingham et al., 2009). Eqn. (2.14) simplifies to the following:

$$\frac{\partial}{\partial x_i} \left(\frac{\partial u_i u_j}{\partial x_j} - \frac{1}{\rho} \frac{\partial \tau_{ij}}{\partial x_j} + \frac{1}{\rho} \frac{\partial p}{\partial x_i} - \frac{1}{\rho} S_i \right) = 0 \quad (2.15)$$

After the discretization process of Eqn. (2.15) it is possible to find the pressure.

2.2 Rheological Models

Rheology is the science of the deformation and flow of matter and it is expressed with relationships between stress and strain or/and stress and rates of strain, see (Bird et al., 1987). The rheological behaviour of SCC is determined by a rheometer and it is typically described with the Bingham or Herschel-Bulkley material model. The SCC involved in this thesis though is described with rheological parameters from the Bingham material model. However, since the numerical simulations based on "pure" CFD solvers are not

capable of handling the Bingham material model, it is approximated with the bi-viscosity model when treated numerically. In section 2.2.1, the Bingham material model is described, while the bi-viscosity model as well as the reason for the approximation are presented in section 2.2.2. The Herschel-Bulkley material model is as earlier mentioned not used to describe the rheological behaviour of the SCC itself, but it is used in the settling calculation in section 3.1.3. The Herschel-Bulkley material model is therefore presented in this section together with the other material models.

2.2.1 Bingham Material Model

Mathematically the Bingham material model is described by the following expression in the case of a one dimensional stress state:

$$\begin{aligned} \dot{\gamma} &= 0 & \text{for } \tau < \tau_0 \\ \tau &= \tau_0 + \mu_p \dot{\gamma} & \text{for } \tau \geq \tau_0 \end{aligned} \quad (2.16)$$

Where $\dot{\gamma}$ is the strain rate, τ is the shear stress, τ_0 is the yield shear stress, and μ_p is the plastic viscosity. Basically, fluids described by the Bingham material model start to flow when the threshold value (the yield stress) is exceeded. As soon as this takes place, the fluid flows according to the plastic viscosity and it stops again when the yield stress is no longer exceeded. In Fig. 2.1 the Bingham material model is illustrated.

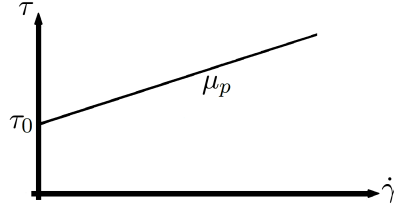


Figure 2.1: *The relationship between the shear stress and the shear rate for the Bingham material model, Gram (2009).*

2.2.2 Bi-viscosity Material Model

In order to use a Bingham material model for a numerical simulation one would have to program a solver capable of analysing one part of the domain as a solid and the remaining part as a fluid. Such a solver is very extensive to program and the calculation is computational heavy. Therefore, the flow of SCC is in most cases simulated with a "pure" CFD solver. However, by doing so it is no longer possible to simulate a Bingham material model, since the part of the domain which is supposed to be simulated as a solid is now simulated as a fluid with an infinitely high viscosity. As a result of this choice, the CFD solver encounters an insoluble problem when trying to handle the Bingham material model which is the infinite high viscosities that occur when the shear rate approaches zero (the part of the domain which is supposed to be simulated as a solid). Consequently, the CFD solver is using a bi-viscosity material model to approximate the Bingham material model. The approximation consists of introducing a very high initial viscosity μ_{init} , see Fig. 2.2, which is active for reference shear rates $\dot{\gamma}^{ref}$ below the threshold value $\dot{\gamma}_0^{ref}$.

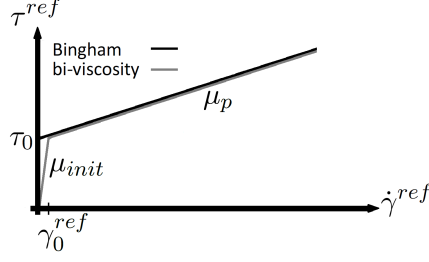


Figure 2.2: *The bi-viscosity model approximating the Bingham material model.*

The initial viscosity enables the CFD solver to simulate the part of the domain, which is supposed to be simulated as a solid, with a very high viscosity so that this part of the domain almost does not move and at the same time the initial viscosity ensures that the CFD solver does not encounter infinite high viscosities. The drawback from introducing the initial viscosity is that the simulated material which in this case is SCC does not stop flowing before being completely shear stress free. Therefore, it is necessary to introduce a stop criterion into the CFD solver when using the bi-viscosity model in order for it to be capable of mimicking a yield stress material such as SCC. The stop criterion is presented in section 4.4. Mathematically the bi-viscosity material model is described by the following expression:

$$\begin{aligned} \tau^{ref} &= \mu_{init} \dot{\gamma}^{ref} & \text{for } \dot{\gamma}^{ref} < \dot{\gamma}_0^{ref} \\ \tau^{ref} &= \tau_0 + \mu_p \dot{\gamma}^{ref} & \text{for } \dot{\gamma}^{ref} \geq \dot{\gamma}_0^{ref} \end{aligned} \quad (2.17)$$

In Fig. 2.2 and Eqn. (2.17) the shear rates and shear stresses are described as reference shear rates and reference shear stresses, respectively, because it is a material law which is valid for a multi-dimensional stress state. The CFD solver couples to the material law based on the Von Mises yield criterion:

$$\tau^{ref} = \sqrt{\frac{3}{2} \tau_{ij} \tau_{ij}} \quad , \quad \dot{\gamma}^{ref} = \sqrt{\frac{1}{2} \dot{\gamma}_{ij} \dot{\gamma}_{ij}} \quad (2.18)$$

2.2.3 Herschel-Bulkley Material Model

The Herschel-Bulkley material model is used as constitutive law when calculating the settling of the aggregates, cf. section 3.1.3. Mathematically it can be expressed in the case of a one dimensional stress state as:

$$\begin{aligned} \dot{\gamma} &= 0 & \text{for } \tau < \tau_0 \\ \tau &= \tau_0 + K \dot{\gamma}^n & \text{for } \tau \geq \tau_0 \end{aligned} \quad (2.19)$$

Where the quantity K and the exponent n are experimentally found. In Fig. 2.3 a sketch of the Herschel-Bulkley material model is illustrated.

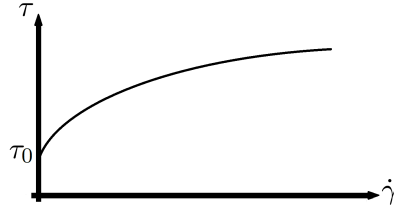


Figure 2.3: The relationship between the shear stress and the shear rate for the Herschel-Bulkley material model.

2.3 Aggregate Settling Equation

All three numerical models developed in this thesis apply a settling calculation which uses an analytical solution for a single spherical particle settling in a non-Newtonian fluid to predict the settling of the aggregates inside the SCC. Therefore, the analytical solution is presented in this section, however, in order to understand the physics involved in the solution the analytical solution for a single spherical particle settling in a Newtonian fluid is described first.

2.3.1 Single Spherical Particle in Newtonian Fluid

The settling of a single spherical particle in an unbound Newtonian fluid is well understood, cf. (Batchelor, 1967). When a single spherical particle is suspended at rest in a Newtonian fluid, it experiences two opposing forces: the gravitational force F_G and buoyancy force F_B , as seen in Fig. 2.4.

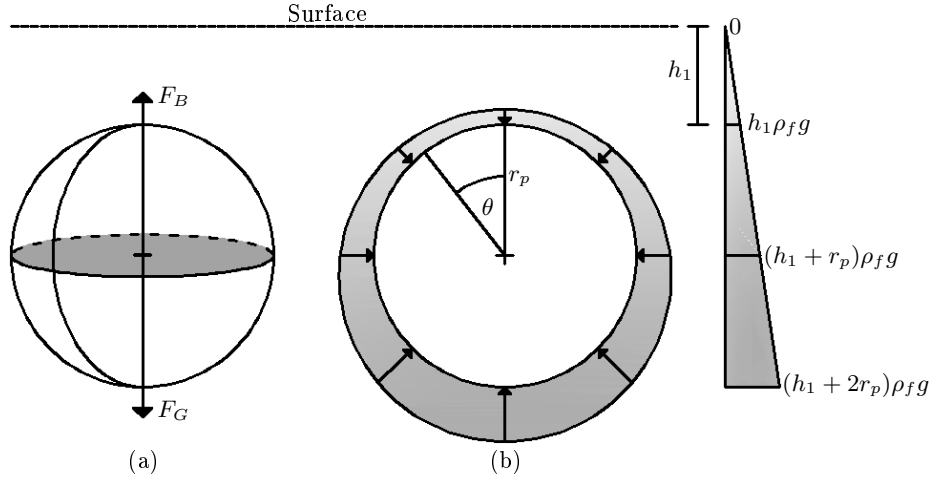


Figure 2.4: Illustration of (a) forces and (b) pressure acting on a particle, at rest.

The gravitational force acting on the particle is given by

$$F_G = m_p g = V_p \rho_p g = \frac{4}{3} \pi r_p^3 \rho_p g = \frac{\pi d_p^3 g \rho_p}{6} \quad (2.20)$$

Where m_p , V_p , ρ_p , r_p and d_p are the mass, the volume, density, radius and diameter of the particle, respectively. It is the pressure difference between the upper and lower part of the particle as shown in Fig. 2.4 that causes the upward acting force also known as the buoyancy force. In order to obtain a mathematical expression for this buoyancy force,

the pressure P as a function of the angle θ for a circle is first found, see Eqn. (2.21). Note that θ is 0 at the top of the circle and π at the bottom.

$$P(\theta) = -\rho_f g r_p \cos \theta + (h_1 + r_p) \rho_f g \quad (2.21)$$

The subscript f represents the surrounding fluid. In Eqn. (2.21) the pressure has the direction towards the center of the circle. However, since it is the vertically acting pressure that needs to be evaluated, the pressure is projected onto the vertical axis:

$$P_z(\theta) = (-\rho_f g r_p \cos \theta + (h_1 + r_p) \rho_f g) \cos \theta \quad (2.22)$$

The objective is a pressure expression for a sphere instead of a circle, therefore Eqn. (2.22) is multiplied by the θ dependent perimeter of a sphere:

$$P_z(\theta) = (-\rho_f g r_p \cos \theta + (h_1 + r_p) \rho_f g) \cos \theta 2\pi r_p \sin \theta \quad (2.23)$$

The buoyancy force is obtained by integration of Eqn. (2.23) from 0 to π . Note that when integrating over an arclength the Jacobi determinant is applied.

$$\begin{aligned} F_B &= \int_0^\pi P_z(\theta) d\theta = \int_0^\pi (-\rho_f g r_p \cos \theta + (h_1 + r_p) \rho_f g) \cos \theta 2\pi r_p \sin \theta r_p d\theta \\ &\Rightarrow \\ F_B &= \int_0^\pi P_z(\theta) d\theta = -\frac{4}{3}\pi r_p^3 \rho_f g = -\frac{\pi d_p^3 g \rho_f}{6} \end{aligned} \quad (2.24)$$

The buoyancy force is negative due to the definition of the angle θ and it is equal to the mass times gravity of the fluid displaced by the particle exactly as Archimedes principle states. A comparison between Eqn. (2.20) and (2.24) shows that if the density of the particle and the fluid is equal, the resulting force is zero. However, if the density of the particle is greater than the density of the fluid, there is a net downward force:

$$F_G + F_B = \frac{\pi d_p^3 g (\rho_p - \rho_f)}{6} \quad (2.25)$$

When the particle starts to move downwards, an upwards drag force is introduced as illustrated in Fig. 2.5.

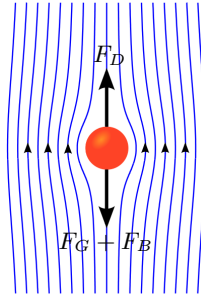


Figure 2.5: Illustration of downward and drag force acting on particle (en.wikipedia.org, 2012).

The drag force expression used in this study is based on Stokes law, which basically expresses the frictional force acting on the interface between the fluid and the particle. Stokes drag force is given by:

$$F_D = 3\pi d_p \mu_f V^s \quad (2.26)$$

Where μ_f is the viscosity of the fluid and V^s is the settling velocity of the particle. Stokes law is valid for small Reynolds numbers only. When the Reynolds number is below 0.3 the flow is streamlined and if that is the case it is possible to set Eqn. (2.25) equal to Eqn. (2.26) in order to obtain the settling velocity of a single spherical particle in a Newtonian fluid. Note that the settling velocity in Eqn. (2.27) is the velocity arising when the drag, buoyancy, and gravitational force are in equilibrium.

$$V^s = \frac{d_p^2 g (\rho_p - \rho_f)}{18\mu_f} \quad (2.27)$$

2.3.2 Single Spherical Particle in non-Newtonian Fluid

Three different analytical solutions for the settling velocity of a spherical particle in a non-Newtonian yield stress fluid such as SCC are investigated in this study. In chapter 5, it is specified which analytical solution is used in each of the three numerical models settling calculation.

Basically, all three analytical solutions are established by substituting the surrounding fluid's viscosity in Eqn. (2.27) with an alternative viscosity. The first analytical solution seen in Eqn. (2.28) is based on the Bingham/bi-viscosity material model and substitutes the viscosity with the plastic viscosity from Eqn. (2.16)/(2.17).

$$V^s = \frac{d_p^2 g (\rho_p - \rho_f)}{18\mu_p} \quad (2.28)$$

The second analytical solution is presented in (Roussel, 2006b) and (Shen et al., 2009). The solution is seen in Eqn (2.30) and is also obtained considering a Bingham/bi-viscosity material model, but instead of substituting the viscosity with the plastic viscosity, the viscosity is substituted with the apparent viscosity μ_{app} :

$$\mu_{app} = \frac{\tau_0}{\dot{\gamma}} + \mu_p \quad (2.29)$$

$$V^s = \frac{d_p^2 g (\rho_p - \rho_f)}{18\mu_{app}} \quad (2.30)$$

The final analytical solution seen in Eqn. (2.32) is based on the Herschel-Bulkley material model. It substitutes the viscosity with the tangential viscosity presented in Eqn. (2.31). Note that Eqn. (2.31) is Eqn. (2.19) differentiated with respect to the shear rate.

$$\mu_{tan} = nK(\dot{\gamma})^{n-1} \quad (2.31)$$

$$V^s = \frac{d_p^2 g (\rho_p - \rho_f)}{18\mu_{tan}} \quad (2.32)$$

2.4 The Aggregate Volume Fraction's Effect on Rheological Parameters

In the MATLAB model, the aggregate volume fraction's effect on the rheological parameters is taken into account. Unfortunately, no literature on the aggregate volume fractions' effect on rheological parameters is available for a suspension with different sizes of aggregates such as SCC. Therefore, the dependency is approximated with semi-empirical

relationships based on studies with mono-sized particles. The semi-empirical relationship describing the effect of the volume fraction of mono-sized particles on the yield stress originates from (Chateau et al., 2008) and (Mahaut et al., 2008) and is seen in Eqn. (2.33).

$$\frac{\tau_0(\phi)}{\tau_0(0)} = \sqrt{(1 - \phi) \left(1 - \frac{\phi}{\phi_m}\right)^{-2.5\phi_m}} \quad (2.33)$$

Where ϕ is the aggregate volume fraction and ϕ_m is the dense packing fraction. In Eqn. (2.34) the corresponding mono-sized particle volume fractions' effect on the plastic viscosity is shown, cf. (Krieger and Dougherty, 1959).

$$\frac{\mu_p(\phi)}{\mu_p(0)} = \left(1 - \frac{\phi}{\phi_m}\right)^{-2.5\phi_m} \quad (2.34)$$

Chapter 3

Modelling

This chapter presents first the solver, free surface, and implementation of the settling calculation for the two FLOW-3D models. Afterwards, the three same topics are described for the MATLAB model along with a presentation of the implementation of the aggregate volume fraction's effect on the rheological parameters.

3.1 FLOW-3D Models

FLOW-3D is a general-purpose computer program which can be executed in parallel. Using input data, the user can select different physical options to represent a wide variety of fluid flow phenomena. The program can be operated in several modes corresponding to different limiting cases of the governing equations in section 2.1. The details for the numerical methods used to model flow of SCC with FLOW-3D are described in the following subsections.

3.1.1 Solver

The governing equations presented in section 2.1 are solved using the Finite Difference Method (FDM) or Finite Volume Method (FVM) in FLOW-3D. The FLOW-3D manual (www.flow3d.com, 2010) does not specify which method it uses when choosing a specific solver, but in the present case it is most likely the FVM, since it handles non-constant material parameters easier than the FDM. The SCC is modelled as a single incompressible fluid, as mentioned in section 2.1.1. In FLOW-3D it is possible to specify how the pressure and the viscous stress are supposed to be solved and for the FLOW-3D simulations in this thesis the pressure and viscous stress are chosen to be solved implicitly with the Generalized Minimum RESidual (GMRES) method. The GMRES is an iterative solver which is highly accurate and efficient for a wide range of problems according to (www.flow3d.com, 2010). The solver uses more memory than the Successive Over-Relaxation (SOR) and Alternating Direction Implicit (ADI) method, but it possesses good convergence, symmetry and speed properties. In (Yao, 2004) more details about the GMRES solver are presented. As mentioned in section 2.1.3, FLOW-3D does not solve the presented pressure equation, but it solves the pressure with the pressure change equation in Eqn. (3.3). The derivation of the pressure change equation is carried out in (Yao, 2004). The algorithm used by FLOW-3D to advance the solution through one increment of time with the specified settings consists of the following steps. Note that t , $t + \Delta t$, and $*$ represent the old, new, and intermediate time level, respectively.

1. The intermediate velocity fields u_i^* are found explicitly by the use of the momentum equations in section 2.1.2 on discretized form. Eqn. (3.1) shows at which time level the different terms are considered.

$$\rho^t \frac{u_i^* - u_i^t}{\Delta t} + \rho^t \frac{\partial(u_i u_j)}{\partial x_j} \Big|_t = - \frac{\partial p}{\partial x_i} \Big|_t + \frac{\partial}{\partial x_j} \left(\mu^t \left(\frac{\partial u_i}{\partial x_j} + \frac{\partial u_j}{\partial x_i} \right) \right) \Big|_t + S_i \Big|^{t+\Delta t} \quad (3.1)$$

2. The velocity fields at the new time level $u_i^{t+\Delta t}$ are found by solving one system of equations with the GMRES solver. Note that the superscript Δt means the difference between the values at time t and $t + \Delta t$.

$$\rho^t \frac{u_i^{t+\Delta t} - u_i^*}{\Delta t} = \frac{\partial}{\partial x_j} \left(\mu^t \left(\frac{\partial u_i}{\partial x_j} + \frac{\partial u_j}{\partial x_i} \right) \right) \Big|^{t+\Delta t} \quad (3.2)$$

3. The pressure change p' is equal to $p^{t+\Delta t} - p^t$ and it is found by the pressure change equation, which is solved as a system of equations with the GMRES solver:

$$\frac{\partial u_i^{t+\Delta t}}{\partial x_i} - \frac{\Delta t}{\rho^t} \frac{\partial^2 p'}{\partial x_i^2} = 0 \quad (3.3)$$

4. The pressure at the new time level is updated based on the pressure change and the pressure at the old time level.
5. The free-surface is updated based on the velocities at the new time level, see section 3.1.2.
6. The densities and viscosities are updated based on the new position of the free surface and the velocities at the new time level.
 - Additional steps for the settling calculation in FLOW-3D model #1
7. The position of the discrete spherical particles which represent the aggregates are calculated, see section 3.1.3.1.
 - Additional steps for the settling calculation in FLOW-3D model #2
7. The volume fraction scalar ϕ which represent the aggregates is advected based on the velocities at the new time level, see section 3.1.3.2. The advection procedure enables the volume fraction scalar to follow the streamlines of the global flow.
8. The settling of the volume fraction scalar is calculated based on the new position of the free surface and the velocities at the new time level, see section 3.1.3.2.

Note that step #1 to 6 are the only steps taken into account when simulating the LCPC-box test in section 4.4, since the gravity induced aggregate migration is not considered in that study.

When modelling flow of SCC it is essential to treat the diffusive velocity terms implicitly, since this prevents the time step to be limited by the diffusive explicit stability limit in Eqn. (3.4). This limit is an approximate expression which is valid only for the limited case of a uniform grid and constant material parameters. Nevertheless, the expression

indicates that the critical diffusive time step Δt_D decreases when the viscosity increases, cf. (Hattel, 2005).

$$\Delta t_D < \frac{\rho \Delta x^2}{6\mu} \quad (3.4)$$

In Eqn. (3.5) the critical diffusive time step is calculated with typical values when the fluid is affected by the initial viscosity of the bi-viscosity material model (Control Volume (CV) size of 0.01 m):

$$\Delta t_D < \frac{2500 \text{ kg/m}^3 \cdot (0.01 \text{ m})^2}{6 \cdot 10^6 \text{ Pas}} \approx 4 \cdot 10^{-8} \text{ s} \quad (3.5)$$

A critical diffusive time step of $4 \cdot 10^{-8} \text{ s}$ means that it is necessary to use $2.5e9$ time steps if a form filling takes 100 s, which from a calculation time point of view is an unrealistic amount of time steps. Therefore, it is crucial to treat the diffusive velocity terms implicitly.

In Eqn. (3.6) the convective explicit stability limit is shown. The FLOW-3D solver needs to comply with this limitation in order not to obtain oscillating velocity fields, since it considers the convective terms at the old time step. Treating the non-linear convective terms at the old time step is a convenient way to linearise a non-linear problem, which otherwise needs to be solved with a heavy iterative process. The stability condition states that, at the convective limit, fluid cannot be fluxed by more than one cell per time-step. Consequently, the higher the velocity, the lower the critical convective time step Δt_C , cf. (Hattel, 2005).

$$\Delta t_C < MIN \left[\left| \frac{\Delta x_i}{u_i} \right| \right] \quad (3.6)$$

The highest velocity experienced in an SCC casting is typically at the inlet and it is of the order 1 m/s. In that case the critical convective time step yields (CV size of 0.01 m):

$$\Delta t_C < MIN \left[\left| \frac{0.01 \text{ m}}{1 \text{ m/s}} \right| \right] = 0.01 \text{ s} \quad (3.7)$$

The order of magnitude calculations of the critical time step in Eqns. (3.5) and (3.7) illustrate that the convective stability limit by far is not as critical as the diffusive one when modelling flow of SCC. Therefore, from a stability view point it is not problematic to consider the convective terms at the old time step as the FLOW-3D solver does.

3.1.2 Free Surface Algorithm

In FLOW-3D there are four different algorithms to track a sharp interface. The Volume Of Fluid (VOF) advection algorithm used for all the FLOW-3D models involved in this thesis is based on the donor-acceptor approach first introduced by (Hirt and Nichols, 1981). At this place it is appropriate to mention that C.W. Hirt is the founder of Flow Science, which is the software company producing FLOW-3D. The used VOF method is the default choice when modelling a single incompressible fluid. It tracks the free surface based on the fluid fraction function F , which is defined to be equal to 1.0 in the fluid and 0.0 in the void surrounding the fluid. A value in between appears if a given cell contains an interface between the fluid and the void region, as seen in Fig. 3.1.

0.00	0.00	0.02	0.33
0.00	0.02	0.72	1.00
0.00	0.57	1.00	1.00
0.70	1.00	1.00	1.00

Figure 3.1: *Fluid fraction values for an arbitrary interface Kalland (2008).*

Eqn. (3.8), from (Barkhudarov, 2004), describes the evolution of the free surface:

$$V_f \frac{\partial F}{\partial t} + \frac{\partial(a_i^t u_i^{t+\Delta t} F^t)}{\partial x_i} = 0 \quad (3.8)$$

where V_f and a_i are the volume and area fractions describing the geometrical constraints of the flow. The algorithm computes the volumetric fluxes by geometrically reconstructing the interface using the values of the fluid fraction function at the old time step in and around a given CV. By doing so, the numerical solution of Eqn. (3.8) is prevented from unphysical distortion of the interface and preservation of its sharpness. Consequently, the interface between fluid and void is no more than one cell wide. In addition, the algorithm uses operator splitting, meaning, that it splits up the advection calculation, one for each direction. According to (Barkhudarov, 2004), the evaluation of volume fluxes in a given direction with the applied VOF advection algorithm is at least as high as that attributed to the piecewise linear interface calculation (PLIC) method. In section 3.2.2, the PLIC method is described in more detail.

3.1.3 Settling Calculation

As mentioned in chapter 1 two different numerical approaches are used to capture the gravity induced aggregate migration with FLOW-3D. The approaches are described in the next two subsections.

3.1.3.1 FLOW-3D Model #1

The first numerical method for capturing the gravity induced aggregate migration is a discrete approach and it is applied in Paper - I (Spangenberg et al., 2010). In FLOW-3D the model is called "Mass Particles" and it allows for multiple particles to be included into the fluid simulation, (www.flow3d.com, 2010). The dynamics of each of the particles

is described by:

$$\frac{du_p}{dt} = -\frac{1}{\rho_p}\Delta P + g + K\beta(u - u_p)|u - u_p|\frac{\rho}{\rho_p} \quad (3.9)$$

$$\beta = \frac{3}{4d} \left(\frac{24}{Re} + \frac{6}{1 + \sqrt{Re}} + 0.4 \right) \quad (3.10)$$

$$Re = \frac{d\rho|u - u_p|}{\mu} \quad (3.11)$$

Where u_p and ρ_p are the velocity and the density of the particle, respectively, u and P are velocity and pressure of the fluid, β is the drag coefficient divided by the particle mass and the quantity K is a drag force multiplier. For small Reynolds numbers the drag force in Eqn. (3.10) approaches the Stokes analytical solution for a viscous laminar flow around a sphere, cf. section 2.3.1.

3.1.3.2 FLOW-3D Model #2

The second numerical method for capturing the gravity induced aggregate migration is a continuum approach and it is used in Paper - II (Spangenberg et al., 2012b) and Paper - IV (Spangenberg et al., 2011). The migration is captured by an advection and a settling calculation of the volume fraction scalar ϕ , which respectively are performed by a "standard" scalar advection solver in FLOW-3D and by a programmed subroutine. The advection procedure is carried out by solving the transport equation in Eqn. (3.12) and it allows the volume fraction scalar to follow the streamlines of the global flow.

$$\frac{\partial \phi}{\partial t} + \frac{\partial(\phi u_i)}{\partial x_i} = 0 \quad (3.12)$$

The advection is explicitly calculated by a split numerical scheme which is at least second-order accurate. The explicitly updated advection introduces a time step limitation, which is similar to the convective explicit stability limit in Eqn. (3.6). The equation for the settling part of the volume fraction evaluation is derived based on a mass change consideration; see Eqn. (3.13) and the illustration in Fig. 3.2.

$$\frac{\partial M_k}{\partial t} = \dot{M}_{in} - \dot{M}_{out} \quad (3.13)$$

Where M_k is the mass of the particles in the evaluated cell, and \dot{M}_{in} and \dot{M}_{out} are the mass fluxes in and out of the evaluated cell, respectively.

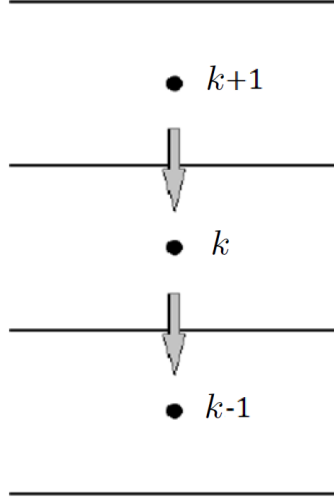


Figure 3.2: *Mass flux illustration.*

The mass and mass fluxes seen in Eqn. (3.13) can be rewritten to Eqn. (3.14) for a two dimensional case with a structured mesh.

$$\frac{\partial(F_k \phi_k \rho_a \Delta x \Delta y)}{\partial t} = F_{k+1} \phi_{k+1} \rho_a V_{k+1}^s \Delta x - F_k \phi_k \rho_a V_k^s \Delta x \quad (3.14)$$

Where $\Delta x/\Delta y$ are the lengths of the CV in each direction. Note that only the settling in the y-direction is considered, due to the fact that gravity is the driving force. Applying the explicit Euler scheme on Eqn. (3.14) for the time derivative it is possible to obtain Eqn. (3.15) which describes the volume fraction of the aggregates at the new time step.

$$\phi_k^{t+\Delta t} = \phi_k \left(1 - V_k^s \frac{\Delta t}{\Delta y} \right) + \phi_{k+1}^t + V_{k+1}^s \frac{\Delta t}{\Delta y} \frac{F_{k+1}}{F_k} \quad (3.15)$$

The expression for the settling velocity is described in section 2.3.2. The volume fraction subroutine is as mentioned calculated with an explicit scheme which thereby introduces a time step criterion for stability. The time step criterion automatically drops out of Eqn. (3.15). The expression in the bracket of the first term on the right hand side does not give any physical meaning if it has a negative value. Therefore, the time step criterion can be written as seen in Eqn. (3.16).

$$\Delta t < \frac{\Delta y}{V_k^s} \quad (3.16)$$

In order to get an order of magnitude for the time step criterion in Eqn. (3.16) the following values are used; a CV length of $\Delta y = 0.01$ m, a diameter of the aggregates of 0.015 m, a density difference between the aggregates and the surrounding fluid of 400 kg/m^3 , and viscosity of the surrounding fluid of 10 Pas (which is a low assessment).

$$\Delta t < \frac{18 \cdot 0.01 \text{ m} \cdot 10 \text{ Pas}}{(0.015 \text{ m})^2 \cdot 9.82 \text{ m/s}^2 \cdot 400 \text{ kg/m}^3} \approx 2 \text{ s} \quad (3.17)$$

The calculation of the critical time step in Eqn. (3.17) shows that it is more than the critical convective stability limit in Eqn. (3.7).

3.2 MATLAB Model

In the following subsections the numerical model developed in the technical computing language MATLAB is described. The MATLAB model has a lot of similarities with the FLOW-3D models, but some of the programmed numerical techniques deviate and especially those are described in detail.

3.2.1 Solver

The two dimensional two-phase CFD-solver programmed in MATLAB solves the pressure and the velocity equations presented in section 2.1. The discretization of the equations is documented in the Technical Report #1. The discretization is carried out with the Finite Volume Method (FVM) on a staggered grid. An illustration of a staggered grid, where the velocities are calculated for the points lying on the faces of the pressure CVs, is illustrated in Fig. 3.3. The staggered grid formulation is an elegant discretization method whose benefits are e.g. elimination of checkerboard pressure fields, cf. (Patankar, 1980).

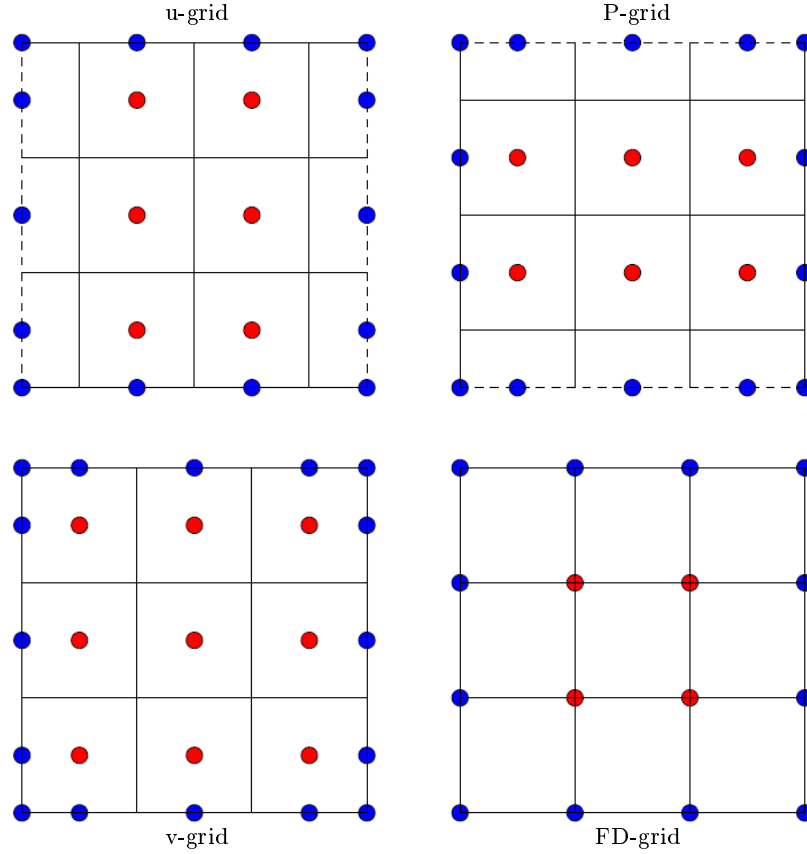


Figure 3.3: *The staggered grid arrangement in two dimensions, (Bingham et al., 2009).*

The MATLAB solver is programmed to consider the pressure and viscous stresses implicitly, whereas the convective term is taken explicitly into account. The viscous stresses are implicitly calculated as in the FLOW-3D models in order not to be limited by the strict diffusive stability limit specified in Eqn. (3.4). The system of equations is solved

by the direct solver in MATLAB and the algorithm advances the solution through one increment of time by the following steps.

1. The new pressure and velocity fields are found by the pressure and momentum equations in section 2.1 on discretized form. They are solved in one system of equations with MATLAB's direct solver:

$$\frac{\partial}{\partial x_i} \left(\frac{\partial u_i u_j}{\partial x_j} \right) \Big|_t - \frac{1}{\rho^t} \frac{\partial}{\partial x_j} \left(\mu^t \left(\frac{\partial u_i}{\partial x_j} + \frac{\partial u_j}{\partial x_i} \right) \right) \Big|^{t+\Delta t} + \frac{1}{\rho^t} \frac{\partial p}{\partial x_i} \Big|^{t+\Delta t} - \frac{1}{\rho^t} S_i \Big|^{t+\Delta t} = 0 \quad (3.18)$$

$$\rho^t \frac{u_i^{t+\Delta t} - u_i^t}{\Delta t} + \rho^t \frac{\partial(u_i u_j)}{\partial x_j} \Big|_t = - \frac{\partial p}{\partial x_i} \Big|^{t+\Delta t} + \frac{\partial}{\partial x_j} \left(\mu^t \left(\frac{\partial u_i}{\partial x_j} + \frac{\partial u_j}{\partial x_i} \right) \right) \Big|^{t+\Delta t} + S_i \Big|^{t+\Delta t} \quad (3.19)$$

2. The free-surface is updated based on the velocities at the new time level, see section 3.2.2.
3. The densities are updated based on the new position of the free surface, see section 3.2.2.
4. The volume fraction scalar which represents the aggregates is advected based on the velocities at the new time level, see section 3.2.3. The advection procedure enables the volume fraction scalar to follow the streamlines of the global flow.
5. The viscosities are updated based on the new position of the free surface, the velocities at the new time level and the volume fraction scalar.
6. The settling of the volume fraction scalar is calculated based on the new position of the free surface and viscosities, see section 3.2.3.

Note that steps/effects related to the gravity induced aggregate migration are not taken into account when simulating the LCPC-box test in section 4.5.

One difference between the FLOW-3D solver described in section 3.1.1 and the MATLAB solver described here is that the first splits up the pressure and velocity calculation and uses an iterative solver, while the latter solves the pressure and velocities together in one system of equations with a direct solver. Especially for large domains it may be of interest to use the FLOW-3D algorithm from a calculation time point of view, although the more explicit nature of the algorithm may introduce a more strict time step criterion as compared to the one for the MATLAB solver. Another difference between the two solvers is that the MATLAB solver considers two phases; the SCC and the surrounding air, whereas the FLOW-3D solver only considers one phase; the SCC. From a calculation time point of view the latter mentioned method is beneficial, since it decreases the system of equations, however, the implementation is also more complex, because it is necessary to apply explicit pressure and velocity boundary conditions at the free surface.

3.2.2 Free Surface Algorithm

The MATLAB model uses a VOF method much like the one used in FLOW-3D to track the free surface. The implementation is carried out based on the work in Kalland (2008) and it is shortly reviewed in this section. The fluid fraction function is used to distinguish between the two phases. The function has a value of 1.0 for the SCC phase, 0.0 for the air phase and a value in between if the given cell is containing an interface between the two phases, see Fig. 3.1. The MATLAB solver uses the PLIC technique, which approximates the interface as a straight line within a cell separating the two phases. In Fig. 3.4 the approximate interface is shown for the fluid fraction values in Fig. 3.1. The figure illustrates how the discontinuous interface is a part of the PLIC technique.

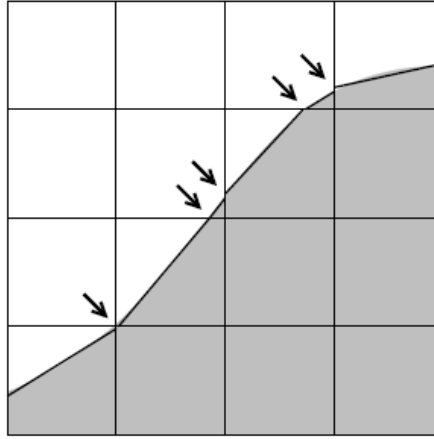


Figure 3.4: *Piecewise linear interface construction, (Kalland, 2008). Discontinuities are marked with arrows.*

The linear interface within each cell can be represented by the linear equation:

$$ax + by + c = 0 \quad (3.20)$$

where $[a, b]^T$ is the line's unit normal vector pointing away from the SCC phase and c is the distance from the line to the point p , which is defined as the center of the cell, see Fig. 3.5.

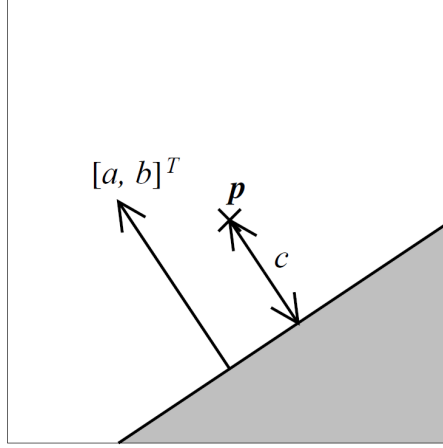


Figure 3.5: *The scalars for the line equation representing the linear interface, (Kalland, 2008).*

The MATLAB model uses the Efficient Least Squares Volume of fluid Interface Reconstruction Algorithm (ELSVIRA) introduced by (Pilliod, 1992) to predict the normalized normal and it has second order accuracy according to (Pilliod Jr. and Puckett, 2004) . The steps involved in advancing the free surface through one increment of time is:

1. A 3x3 block of cells around the interface containing cell is used to find six unit normal vectors, by applying the forward, backward and central difference schemes on the column and row sums of the fluid fraction function.
2. The distance c in Eqn. (3.20) is found for each of the six unit normal vectors, by mathematical manipulation of the piecewise second degree polynomial describing the volume fraction in a cell, cf. (Kalland, 2008).
3. The best unit normal vector and appurtenant distance c is found by the lowest Euclidean norm, see Eqn. (3.21). Where \hat{F} is the fluid fraction of each of the nine cells when extending the linear interface to the edges of the entire 3x3 block. An illustration of the calculation is shown in Fig. 3.6.

$$E = \left(\sum_{k=1}^3 \sum_{l=1}^3 (\hat{F}_{k,l} - F_{k,l})^2 \right)^{\frac{1}{2}} \quad (3.21)$$

4. The donating/accepting regions for the x-direction advection are found based on the horizontal velocities and the best unit normal vector and appurtenant distance c .
5. The intermediate fluid fractions are found by advecting in the x-direction. The advection is carried out based on the horizontal velocities, the donating/accepting regions and the volume fraction in the old time step.
6. Steps #1-3 are redone.
7. The donating/accepting regions for the y-direction advection are found based on the vertical velocities and the new best unit normal vector and appurtenant distance c .

8. The fluid fractions in the new time step are found by advecting in the y-direction. This advection is carried out based on the vertical velocities, the new donating/accepting regions and the fluid fractions in the intermediate time step.
9. The fluid fraction function is used to find the density and viscosity of all the cells in the domain by linear interpolation:

$$\rho = \rho_{air}(1 - F) + \rho_{scc}F, \quad (3.22)$$

$$\mu = \mu_{air}(1 - F) + \mu_{scc}F \quad (3.23)$$

Note that in every second time step the order of the two advection directions are interchanged in order not to favour one direction.

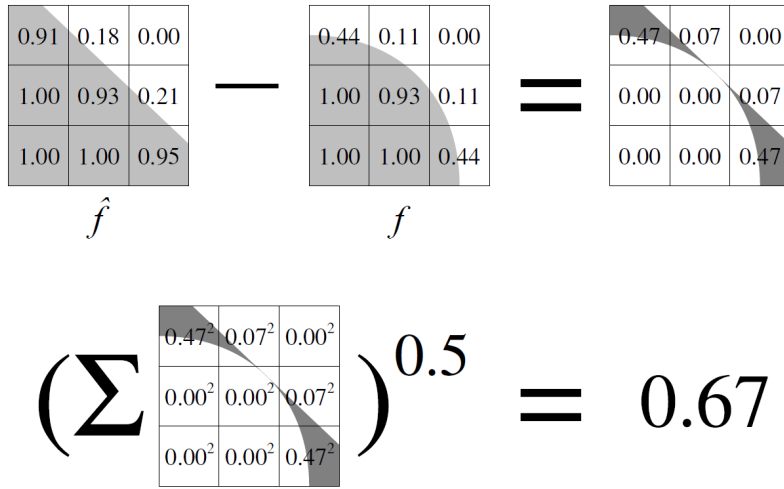


Figure 3.6: An example of the Euclidean norm calculation for determination of the best normalized normal and appurtenant distance c , (Kalland, 2008).

The time step limitation introduced by the explicit update of the free surface is similar to the convective explicit stability limit in Eqn. (3.6) and the overall critical time step does therefore not have to be decreased.

3.2.3 Settling Calculation

In the MATLAB model the settling calculation is implemented much similarly to the implementation for the FLOW-3D model #2, see section 3.1.3.2. The migration of the aggregates is also captured by a volume fraction and the evaluation is carried out with an advection and a settling procedure. The advection calculation in the MATLAB model is as for the FLOW-3D model #2 carried out with an operator splitting numerical scheme. This technique is chosen, since the operators are also split in the free surface algorithm, which therefore eases the advection calculation at the free surface, because the donate/accept regions can be reused.

3.2.4 Rheological Parameter Calculation

The aggregate's effect on the yield stress and plastic viscosity is implemented explicitly based on Eqns. (2.33) and (2.34). The only change in the equations are that they are

made relative to the initial (homogeneous) volume fraction.

$$\frac{\tau_0(\phi)}{\tau_0(\phi_{ini})} = \frac{\sqrt{(1-\phi)(1-\phi/\phi_{max})^{-2.5\phi_{max}}}}{\sqrt{(1-\phi_{ini})(1-\phi_{ini}/\phi_{max})^{-2.5\phi_{max}}}} \quad (3.24)$$

$$\frac{\mu_p(\phi)}{\mu_p(\phi_{ini})} = \frac{(1-\phi/\phi_{max})^{-2.5\phi_{max}}}{(1-\phi_{ini}/\phi_{max})^{-2.5\phi_{max}}} \quad (3.25)$$

Chapter 4

Single Fluid Analysis

This chapter first describes the LCPC-box test together with the derivation of its three and two dimensional analytical solution. Then, the chapter presents the results of the first investigation of this thesis where the numerical result and the analytical solution of the LCPC-box test are compared. The comparison is carried out both for the FLOW-3D model and MATLAB model along with a mesh density, time step, and initial viscosity analysis. Finally, the potential of the LCPC-box test being used as a benchmark test for flow of SCC is discussed.

4.1 LCPC-Box Test

The LCPC-box test was invented by (Roussel, 2007) at Laboratoire Central des Ponts et Chaussées (LCPC) in Paris, France (www.lcpc.fr), hence its name. The LCPC-box test consists of pouring 6l of SCC into a mould and measuring the final height at the pouring end and spread length of the concrete. The measurements together with the analytical solution presented in section 4.2 enable for the yield stress to be found. The test is highly applicable, since it is cheap, fast, and can be carried out at the construction site. In Fig. 4.1 the LCPC-box test is shown for an arbitrary SCC. The dimensions of the LCPC-box are a length of 1.2 m, a height of 0.15 m, and a width of 0.2 m. The analytical solution has



Figure 4.1: *LCPC-Box test for an arbitrary SCC. The SCC is slowly poured at one end of the box, (Roussel, 2007).*

a second functionality and this is that it can be used to compare with numerical results, which is what it is used for in this chapter. The derivation of the analytical solution in three and two dimensions is carried out in the following two subsections.

4.2 Three Dimensional Analytical Solution

The derivation for the three dimensional analytical solution is based on (Nguyen et al., 2006). The solution assumes that the stress tensor simplifies into a scalar shear stress close to the walls and bottom. In addition, the flow stoppage takes place when the shear stress equals the yield stress in these zones, meaning that the analytical solution is valid for a yield stress material only. In Fig. 4.2 an elementary volume for which the differential equation is based is illustrated.

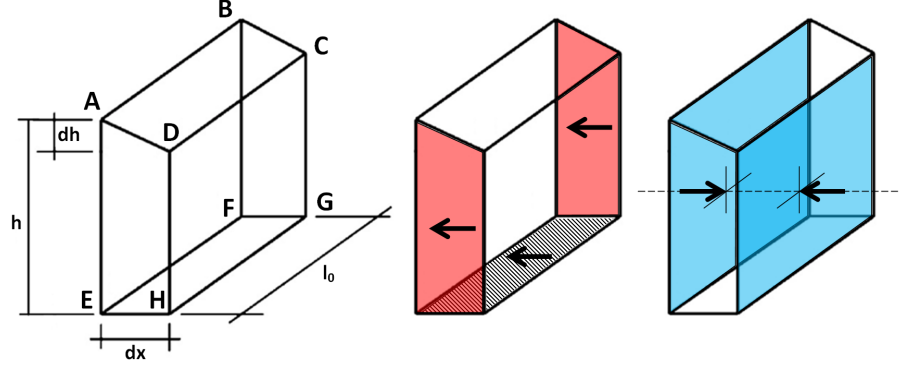


Figure 4.2: An elementary volume in the sample at stoppage, inspired by (Nguyen et al., 2006).

Eqn. (4.1) expresses the force equilibrium on the elementary volume on Fig. 4.2.

$$\left(\rho g l_0 \frac{h^2}{2}\right)_{ABFE} - \left(\rho g l_0 \frac{(h+dh)^2}{2}\right)_{DCGH} - (\tau_0 l_0 dx)_{EFGH} - (2\tau_0 h dx)_{ADHE+BCGF} = 0. \quad (4.1)$$

By conserving only first order terms:

$$\rho g h \frac{dh}{dx} = -\tau_0 - 2\tau_0 \frac{h}{l_0} \quad (4.2)$$

Eqn. (4.2) can be rewritten into the following:

$$\begin{aligned} h \frac{dh}{dx} &= -\left(\tau_0 + 2\tau_0 \frac{h}{l_0}\right) \frac{1}{\rho g} \Rightarrow \\ \frac{2h}{l_0} \frac{dh}{dx} &= -\left(1 + 2\frac{h}{l_0}\right) \frac{2\tau_0}{\rho g l_0} \Rightarrow \\ \frac{\frac{2h}{l_0}}{1 + 2\frac{h}{l_0}} \frac{dh}{dx} &= -\frac{2\tau_0}{\rho g l_0} \Rightarrow \\ \frac{\frac{2h}{l_0}}{1 + 2\frac{h}{l_0}} \frac{d\frac{2h}{l_0}}{dx} &= -\frac{2\frac{2\tau_0}{\rho g l_0}}{l_0} \end{aligned} \quad (4.3)$$

The differential equation in Eqn. 4.4 appears when substituting $A = \frac{2\tau_0}{\rho g l_0}$ and $u = \frac{2h}{l_0}$ in Eqn. (4.3):

$$\frac{u}{1+u} \frac{du}{dx} = -\frac{2A}{l_0} \quad (4.4)$$

Eqn. (4.4) is solved by the following mathematical operations. Note that C_1 , C_2 , and C_3 are arbitrary constants.

$$\begin{aligned}
\int \frac{u}{1+u} du &= \int -\frac{2A}{l_0} dx \Rightarrow \\
u - \ln(u+1) + C_1 &= -\frac{2A}{l_0} x + C_2 \Rightarrow \\
u - \ln(u+1) + C_3 &= -\frac{2A}{l_0} x \Rightarrow \\
\frac{2h}{l_0} - \ln\left(\frac{2h}{l_0} + 1\right) + C_3 &= -\frac{2A}{l_0} x \Rightarrow \\
-h + \frac{l_0}{2} \ln\left(\frac{2h}{l_0} + 1\right) - \frac{l_0}{2} C_3 &= Ax
\end{aligned} \tag{4.5}$$

The constant C_3 is found by inserting $x = 0$ when $h = h_0$:

$$-\frac{l_0}{2} C_3 = h_0 - \frac{l_0}{2} \ln\left(\frac{2h_0}{l_0} + 1\right) \Rightarrow \tag{4.6}$$

$$C_3 = -\frac{2h_0}{l_0} + \ln\left(\frac{2h_0}{l_0} + 1\right) \tag{4.7}$$

The solution to the differential equation in Eqn. (4.4) is therefore:

$$Ax = -h + \frac{l_0}{2} \ln\left(\frac{2h}{l_0} + 1\right) - \frac{l_0}{2} \left(-\frac{2h_0}{l_0} + \ln\left(\frac{2h_0}{l_0} + 1\right)\right) \Rightarrow \tag{4.8}$$

$$Ax = h_0 - h - \frac{l_0}{2} \ln\left(\frac{2h+l_0}{2h_0+l_0}\right) \tag{4.9}$$

When assuming the final spread length L is shorter than the length of the box it is possible to compute h_0 (hidden in u_0) based on Eqn. (4.10), which expresses the total volume V of the sample.

$$V = l_0 \int_0^{h_0} x dh = \frac{l_0^3}{4A} \left(\ln(l + u_0) + \frac{u_0(u_0 - 2)}{2} \right) \tag{4.10}$$

As h_0 is no longer unknown it is possible to obtain the final expression for x as a function of h , by dividing by and substituting A .

$$x = \frac{\left(h_0 - h - \frac{l_0}{2} \ln\left(\frac{2h+l_0}{2h_0+l_0}\right)\right) \rho g l_0}{2\tau_0} \tag{4.11}$$

Also the final spread length can be found by inserting $x = L$ when $h = 0$.

$$L = \frac{\left(h_0 - \frac{l_0}{2} \ln\left(\frac{l_0}{2h_0+l_0}\right)\right) \rho g l_0}{2\tau_0} \tag{4.12}$$

4.3 2D Analytical Solution

The differential equation in Eqn. (4.2) for the three dimensional case simplifies into Eqn. (4.13) for the ideal two dimensional case where there is no influence from the front and back lateral walls ($l_0 \rightarrow \infty$).

$$\rho g h \frac{dh}{dx} = -\tau_0 \tag{4.13}$$

Eqn. (4.13) is solved by the following mathematical operations.

$$\int \rho g h \, dh = \int -\tau_0 \, dx \Rightarrow \quad (4.14)$$

$$\rho g \frac{h^2}{2} + C_1 = -\tau_0 x + C_2 \Rightarrow \quad (4.15)$$

$$\rho g \frac{h^2}{2} = -\tau_0 x + C_3 \Rightarrow \quad (4.16)$$

$$h(x) = \sqrt{\frac{2(-\tau_0 x + C_3)}{\rho g}} \quad (4.17)$$

Where the arbitrary constant C_3 is found from the boundary condition $h(L) = 0$.

$$h(L) = 0 = \sqrt{\frac{2(-\tau_0 L + C_3)}{\rho g}} \Rightarrow \quad (4.18)$$

$$C_3 = \tau_0 L \quad (4.19)$$

The final expression for x as a function of h is given by:

$$x = L - \frac{\rho g h^2}{2\tau_0} \quad (4.20)$$

The spread length is found by inserting $x = 0$ when $h = h_0$.

$$L = \frac{\rho g h_0^2}{2\tau_0} \quad (4.21)$$

Since the area Ar is known, h_0 can be found:

$$\frac{V}{l_0} = Ar = \int_0^{h_0} x dh = \int_0^{h_0} \left(\frac{\rho g h_0^2}{2\tau_0} - \frac{\rho g h^2}{2\tau_0} \right) dh \Rightarrow \quad (4.22)$$

$$h_0 = \left(\frac{3\tau_0 A}{\rho g} \right)^{\frac{1}{3}} \quad (4.23)$$

By Eqns. (4.20), (4.21), and (4.23) it is now possible to find the final shape for a given yield stress.

4.4 FLOW-3D Model

The numerical model developed in FLOW-3D to simulate the LCPC-box test takes step #1 to 6 as described in section 3.1.1 into account when executed. In the LCPC-box test the SCC is slowly poured into the formwork as seen in Fig. 4.1. However, in the FLOW-3D model the SCC is initially situated with the length 0.3 m and the height 0.1 m, see Fig. 4.3. The different initial positions of the SCC do not affect the final shape and spread length, which are the objectives of the analysis, since the inertia forces are negligible.

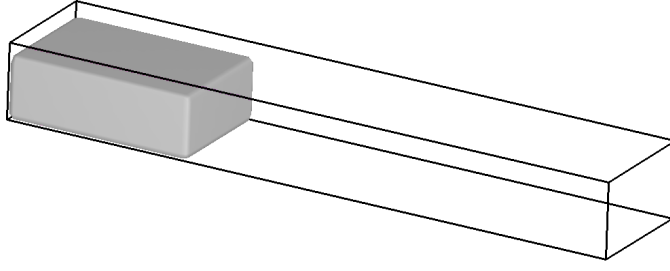


Figure 4.3: *Initial condition for the FLOW-3D model.*

In Fig. 4.3 the grey color represents the fluid and the black box illustrates the domain in which the fluid flows. The boundary condition for all six boundaries is a wall condition (no slip), meaning the velocity in the three directions are zero at the boundary. The mesh used in this investigation is a structured uniform mesh. From a calculation time point of view it could be of interest to use a graded mesh, for instance making the mesh finer at the bottom of the flow domain, where the velocity gradients are the highest. However, since one of the objectives of this investigation is to analysis different mesh densities' effect on the results, it is chosen to use a structured uniform mesh with cubic CVs.

The analytical solution is as earlier mentioned based on a yield stress fluid, while the material model used in the FLOW-3D model is a bi-viscosity material model as described in section 2.2. The bi-viscosity material model is as earlier pointed out only capable of approximating a yield stress fluid by simulating the part of the fluid domain which does not flow with a very high initial viscosity. Consequently, with a bi-viscosity material model the flow of the fluid does not stop before the whole fluid domain is shear stress free. Therefore, it is necessary to terminate the simulation at some point in order to compare it with the analytical solution. In this investigation the simulations are terminated when the spread length of the analytical solution is obtained and the comparison consist afterwards in comparing the final shape.

The numerical results presented in the next two subsections are obtained with an SCC with a density of 2300 kg/m³, a yield stress of 50 Pa, and a plastic viscosity of 50 Pas.

4.4.1 Comparison with Analytical Solution

In Fig. 4.4 the numerical result at the termination point is shown, when a CV length of 0.01 m, a maximum time step of 0.05 s, and an initial viscosity of 1000 Pas are used.

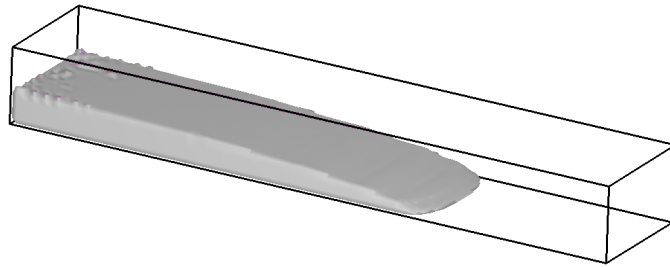


Figure 4.4: *The numerical results at the termination point. The numerical model used a CV length of 0.01 m, a maximum time step of 0.05 s, and an initial viscosity of 1000 Pas.*

In order to compare the numerical results shown in Fig. 4.4 with the analytical solution in Eqn. (4.11), one needs to extract the fluid fraction values in the x-z plane from the middle of the LCPC-box. In Fig. 4.5 the two final shapes are compared.

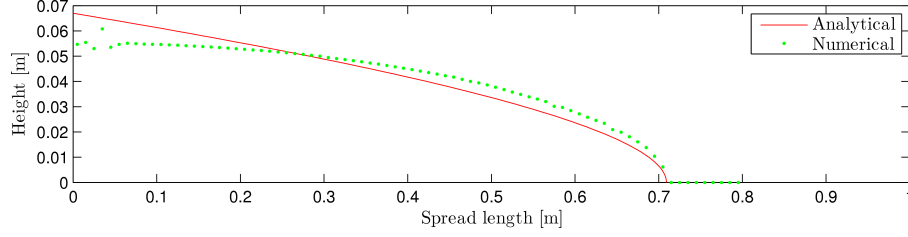


Figure 4.5: *The final shape of the FLOW-3D result and analytical solution.*

There is a fairly good agreement between the numerical result and the analytical solution, cf. Fig. 4.5. At a spread length close to zero the numerical result lies a bit below the analytical solution and at a spread length close to the final spread length the numerical result lies a bit above the analytical solution. In the next subsection it is investigated if a change in the mesh density, time step, or initial viscosity decreases the difference between the two final shapes.

4.4.2 Material Law and Convergence Test

Three different analyses are carried out in this section; a mesh density analysis, a time step analysis, and an initial viscosity analysis. These analyses are performed in order to investigate the sensitivity of the numerical results and to understand which parameters are decreasing the difference between the numerical result and the analytical solution. The evaluation of the numerical results are conducted qualitatively by a visual comparison between the final shapes.

4.4.2.1 Mesh Density Analysis

The final shape for three numerical results with different mesh densities and the analytical solution are shown in Fig. 4.6. The three mesh densities are obtained with a CV length of 0.02 m, 0.01 m, and 0.005 m. In addition, it should be noted that the three simulations are carried out with a maximum time step of 0.05 s and an initial viscosity of 1000 Pas.

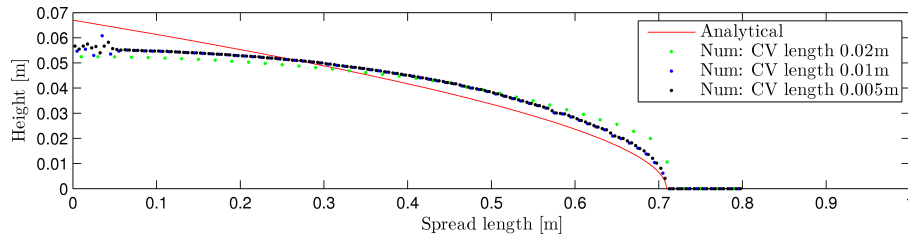


Figure 4.6: *The final shapes of the FLOW-3D results with different CV lengths and the analytical solution.*

The numerical result when using a CV length of 0.02 m seems to lose a bit of accuracy as compared to the other two simulations, see Fig. 4.6. However, the two numerical results with the highest mesh density are almost the same, which indicates that the solution is already converged when using a CV length of 0.01 m. This is an interesting observation,

since one would think that the numerical results would approach the analytical when increasing the mesh density.

4.4.2.2 Time Step Analysis

The time step analysis is carried out with the maximum time steps; 0.05 s, 0.01 s, and 0.005 s. In Fig. 4.7 the three numerical results with different time steps are shown together with the analytical solution. The length of the CVs used in the three simulations is 0.01 m, while the initial viscosity is 1000 Pas.

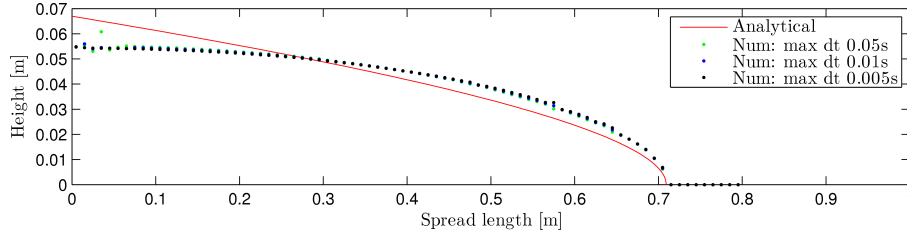


Figure 4.7: *The final shapes of the FLOW-3D results with different maximum time steps and the analytical solution.*

Fig 4.7 shows that the numerical results are already converged when a maximum time step of 0.05 s is used. Furthermore, it shows that the small bumps close to a spread length of zero can be eliminated if the maximum time step is decreased, however, this increased accuracy should be held up against the increased calculation time, which is half an hour when using 0.05 s and seven hours when using 0.005 s. Finally, it should be mentioned that decreasing the time step does not make the numerical result approach the analytical solution.

4.4.2.3 Initial Viscosity Analysis

An initial viscosity of 100 Pas, 1000 Pas and 10 000 Pas are used in this analysis. In Fig. 4.8 the three numerical results with different initial viscosities are shown together with the analytical solution. The three simulations are executed with a CV length of 0.01 m and a maximum time step of 0.05 s.

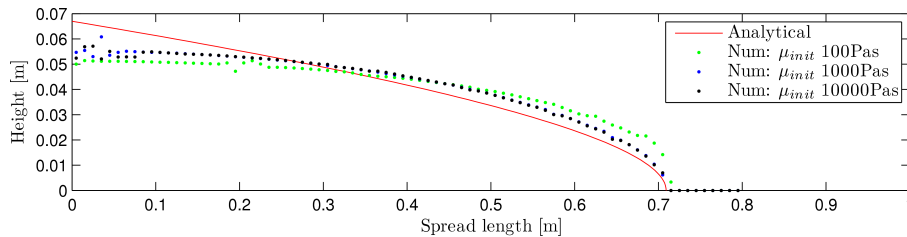


Figure 4.8: *The final shapes of the FLOW-3D results with different initial viscosities and the analytical solution.*

The numerical results approach the analytical solution when increasing the initial viscosity from 100 Pas to 1000 Pas, see Fig. 4.8. However from 1000 Pas to 10 000 Pas it is difficult to see any difference. The calculation time of the simulation with an initial viscosity of 10 000 Pas is 6 hours and a simulation with an even higher initial viscosity is therefore not performed, since the calculation would be too long. The calculation time grows when increasing the initial viscosity, because the maximum time step seems to be unaffected

by this, while the calculation real time before reaching the final spread length where the simulation is terminated, increases. The fact that the maximum time step stays more or less the same may be due to the more explicit nature of the FLOW-3D algorithm as compared to the one used in the MATLAB model.

4.5 MATLAB Model

The MATLAB model simulates the LCPC-box test by taking the relevant steps as described in section 3.2.1 into account when executed. The geometry of the calculation domain is a rectangle as shown in Fig. 4.9, where the initial position of the SCC is also illustrated.

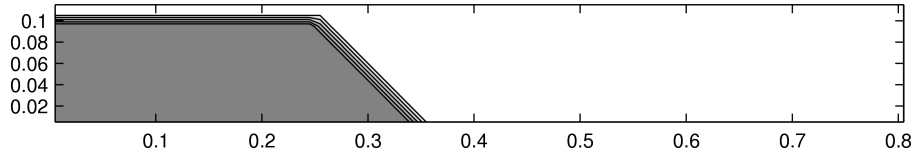


Figure 4.9: *Illustration of calculation domain and initial position of the SCC.*

The boundary condition is as before for the FLOW-3D model a wall condition and also here a structured uniform mesh is used. The numerical results produced by the MATLAB model and presented in the next two subsections are obtained for an SCC with a density of 2500 kg/m³, a yield stress of 50 Pa, and a plastic viscosity of 50 Pas.

4.5.1 Comparison with Analytical Solution

A contour plot of the numerical result is shown in Fig 4.10 when using a CV length of 0.01 m, a time step of 0.01 s, and an initial viscosity of 10 000 Pas.

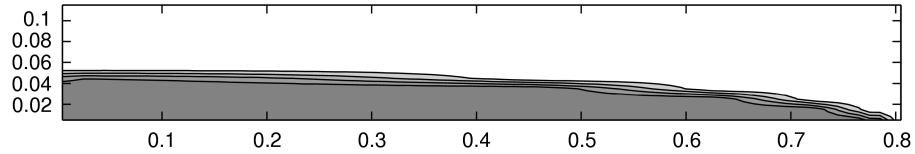


Figure 4.10: *A contour plot of the numerical solution.*

The numerical result is shown together with the two dimensional analytical solution, see Fig. 4.11.

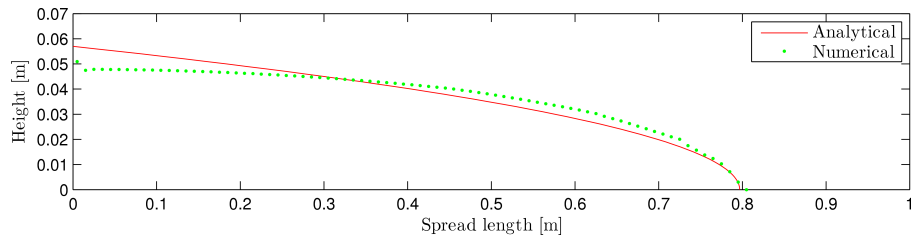


Figure 4.11: *The final shapes of the MATLAB result and analytical solution.*

In Fig. 4.11, the numerical result shows the same trends as the FLOW-3D model does in section 4.4.1. The numerical result lies a bit below the analytical solution at a spread length close to zero, while it is a bit above at a spread length close to the final spread length.

4.5.2 Material Law and Convergence Test

In the next three subsections, the MATLAB model is undertaking the same numerical analyses as carried out for the FLOW-3D model in section 4.4.2. The evaluation of the numerical results are still conducted qualitatively by a visual comparison between the final shapes.

4.5.2.1 Mesh Density Analysis

The mesh density analysis is performed with the CV lengths; 0.02 m, 0.01 m, and 0.005 m. In Fig. 4.12 the numerical results and the analytical solution are shown. The time step and initial viscosity used in the simulations are 0.01 s and 10 000 Pas, respectively.

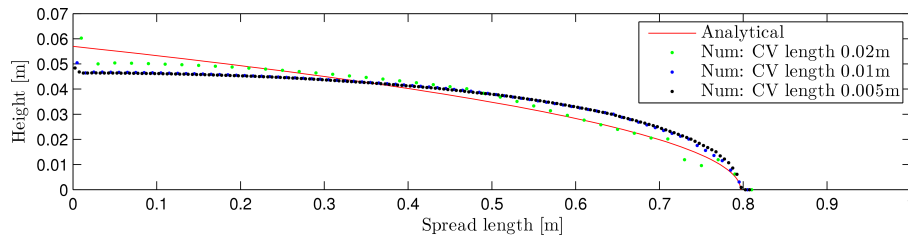


Figure 4.12: *The final shapes of the MATLAB results with different CV lengths and the analytical solution.*

The numerical results are much similar to the ones in the mesh density analysis for the FLOW-3D model in section 4.4.2.1. When using a CV length of 0.02 m the accuracy of the numerical result is not that good, see Fig. 4.12, but the numerical results seem to be converged when using a CV length of 0.01 m.

4.5.2.2 Time Step Analysis

The final shape for the three numerical results with different time steps and the analytical solution are shown in Fig. 4.13. The three different time steps are 0.1 s, 0.01 s, and 0.001 s. The simulations are using a CV length of 0.01 m and an initial viscosity of 10 000 Pas.

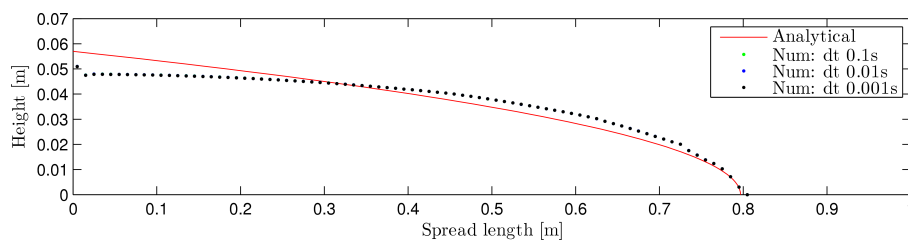


Figure 4.13: *The final shapes of the MATLAB results with different time steps and the analytical solution.*

Fig. 4.13 shows that the numerical results are converged and that a decrease in time step does not affect the numerical result to approach the analytical solution. Note that the same is observed for the FLOW-3D model in section 4.4.2.2.

4.5.2.3 Initial Viscosity Analysis

The initial viscosity included in the analysis are 100 Pas, 10 000 Pas and 1 000 000 Pas. The numerical results and the analytical solution are shown in Fig. 4.14. The CV length

used in the simulations are 0.01 m, while the time step is programmed in such a manner that the movement of the fluid through a CV can be maximum 30% of the cell. The new time step criterion is introduced in order for the simulation with the highest initial viscosity to finish in a reasonable time.

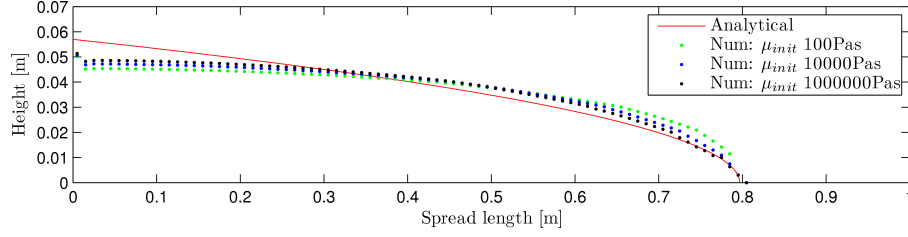


Figure 4.14: *The final shapes of the MATLAB results with different initial viscosities and the analytical solution.*

The numerical result slightly approaches the analytical solution when the initial viscosity is increased, see Fig. 4.14. This observation makes sense since the bi-viscosity material model then acts more and more like a yield stress material. One reason why the same pattern was not as pronounced in the initial viscosity analysis for the FLOW-3D model in section 4.4.2.3 could be that a wider range of initial viscosities are used in this two dimensional analysis. Bearing this observation in mind, one could then argue, why not use an initial viscosity of for instance 10^{16} Pas, however this numerical implementation runs into problems when having an initial viscosity above 1 000 000 Pas. In general numerical implementations often run into problems when using settings which go toward infinity.

4.6 Remarks on LCPC-Box Test

Based on the LCPC-box test it can be concluded that it is possible for both the FLOW-3D and the MATLAB model to obtain a relative good agreement between the numerical results and the analytical solution. In addition, this accuracy depends on the initial viscosity and therefore it can also be concluded that it is impossible for the numerical result to be in total agreement with the analytical solution, since it is impossible to use an infinitely high initial viscosity. On this basis and since it is necessary to fit the numerical results' spread length to the one of the analytical solution, one could state, that the analytical solution for the LCPC-box test cannot be used as a benchmark test for simulating flow of SCC with a CFD code. However, there are three factors which makes this test very useful and recommendable. Firstly, this test gives a very good understanding of the bi-viscosity material model and the error which is introduced when using it to mimic a yield stress fluid. Secondly, it gives an overview of which mesh density, time step and initial viscosity are working for the specific CFD code. Thirdly, the flow simulated in the LCPC-box test is much similar to the flows that the CFD code afterwards should be used for e.g. casting of a beam, a wall or a slab.

Chapter 5

Applications with Aggregate Migration

In this chapter the investigation regarding developing a numerical model capable of predicting the gravity induced aggregate migration is described, by presenting the key numerical results from Paper - I (Spangenberg et al., 2010), Paper - II (Spangenberg et al., 2012b), and Paper - III (Spangenberg et al., 2012a). The papers are presented in chronological order and after each of them a discussion follows, which focuses on the advantages and drawbacks of the applied numerical model. Afterwards, the optimization investigation is presented by introducing the most important points from Paper - IV (Spangenberg et al., 2011) and Technical Report - II. Also here a discussion follows, which puts the studies into perspective.

As was pointed out earlier it is necessary to introduce a stop criterion when using the bi-viscosity material model, cf. section 4.4. The simulations presented in this chapter were terminated either at the end of the form filling or a couple of seconds later, since this was assessed to be a reasonable and realistic stop criterion. In addition, it should be mentioned that the numerical models used initial viscosities of approximately 10^6 Pas in order to capture the yield stress behaviour of the SCC best possible during flow. The FLOW-3D models used an increased initial viscosity in these investigations as compared to the LCPC-box test due to the difference in stop criteria. In the previous investigation the fact that the maximum time step stays the same, while the calculation real time increased, when increasing the initial viscosity, resulted in a higher calculation time. However, since the stop criterion in the present studies prevented the calculation real time of increasing, it was possible to use higher initial viscosities without increasing the calculation time.

5.1 Discrete Aggregate Representation (FLOW-3D Model #1, Paper I)

The FLOW-3D model with the discrete aggregate representation, which is described in section 3.1.3.1, was used in the numerical study carried out in Paper - I (Spangenberg et al., 2010). The model predicted the gravity induced aggregate migration in an SCC beam casting and the final particle distribution was afterwards converted into property maps using semi-empirical relationships. The simulation of the 3 m long and 0.3 m thick beam was carried out in two dimensions, thus the reinforcement and the effect from

lateral walls were assumed to be negligible. As a consequence of the study being purely numerical, the material properties of the SCC were estimated. The global flow of the SCC was modelled with a density of 2200 kg/m^3 , a yield stress of 50 Pa , and a plastic viscosity of 50 Pas . The suspended aggregate was assumed to have a volume fraction of 0.64 when homogeneous, while the amount of aggregates considered being capable of settling corresponded to the 25% coarsest aggregates. The coarsest aggregates were assumed to be spherical with an average diameter of 15 mm and a density of 2700 kg/m^3 . The drag force multiplier β in Eqn. (3.9) was in this study defined as 0.1 and it enabled the viscosity of the surrounding fluid of the particles to be ten times lower than the viscosity of the global SCC flow. Meaning, it was assumed that the particles were settling in a surrounding fluid with viscosities of the order of mortar instead of SCC. As earlier mentioned the simulation was carried out in two dimensions and therefore it was necessary to estimate a number of aggregates going into the simulation which gave a good representation of the settling pattern. In this case the number of aggregates was taken as the number of aggregates which would give the correct volume fraction if they were cut through directly at the middle of the spherical particle. Only one half of the beam was simulated since it had a vertical symmetry line in the middle. In Fig. 5.1 the particle distribution in one half of the beam at the end of the casting is shown.

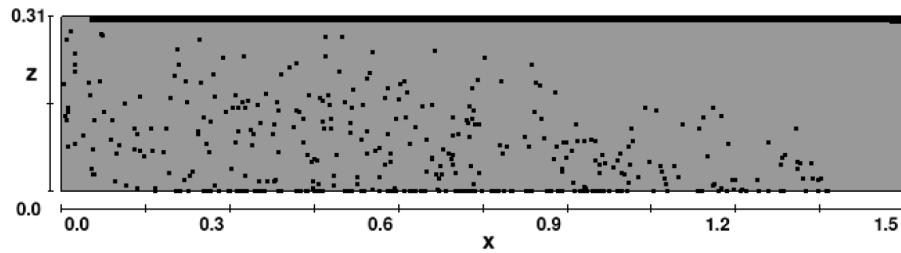


Figure 5.1: *Particle distribution at the end of the casting. Only the right half of the beam is showed. Vertical and horizontal distances are in (m), Paper - I (Spangenberg et al., 2010).*

The model predicted a settling pattern where the coarsest aggregates could not flow to the end of the mould, see Fig. 5.1. In addition, it was noted that there existed zones at the bottom of the formwork where the total volume fraction of the aggregates exceeded the assessed maximum packing fraction of 0.8 . This error was introduced due to the fact that the interactions between particles and between particles and walls were not taking into account in this model. The particles therefore accumulated without any hindrances at the bottom wall.

The aggregate distribution was afterwards converted to a total aggregate volume fraction by adding the local volume fraction of the coarsest aggregates to the volume fraction of the stable finer aggregates. The local volume fraction of the coarsest aggregates were found by dividing the beam into areas of $0.1 \times 0.1 \text{ m}$ and evaluating the numbers of aggregates inside each of them. In Fig. 5.2 the total aggregate volume fraction is shown. Note that in the zones at the bottom of the formwork where the maximum packing fraction of 0.8 was exceeded, the total aggregate volume fraction was set equal to the maximum packing fraction.

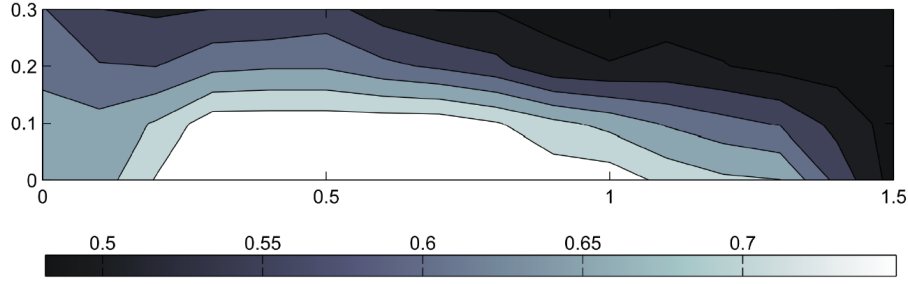


Figure 5.2: *Total aggregate volume fraction map. Vertical and horizontal distances are in (m), Paper - I (Spangenberg et al., 2010).*

The total aggregate fraction together with the simple models proposed in (de Larrard and Le Roy, 1992) and (de Larrard, 1999) allowed for the relative elastic modulus and compressive strength to be found. The variation induced by segregation for both of the properties were of the order of 10%. Another property variation this study shed some light on was the relative drying shrinkage strain which varied up to 25%, as seen in Fig. 5.3. The property was obtained from the relation given in (Eguchi and Teranishi, 2005). The reason why it is preferable not to have high variation of the drying shrinkage strain, is because it potentially could lead to unwanted cracks which could lead to corrosion of the reinforcement and thereby a decreased load carrying capacity.

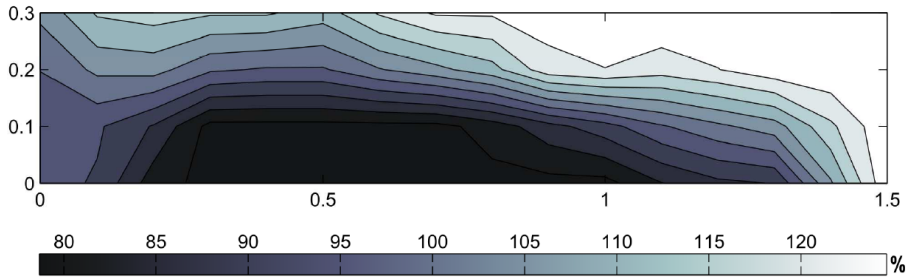


Figure 5.3: *Relative drying shrinkage strain map. Vertical and horizontal distances are in (m), Paper - I (Spangenberg et al., 2010).*

Discussion

This study showed both a strength and some drawbacks for FLOW-3D model #1 when using it to predict gravity induced aggregate migration. The strength of FLOW-3D model #1 is that it is based on the available modules in FLOW-3D. A person who is familiar with FLOW-3D can therefore relatively easy set up the model within a reasonable time. On the other hand, the model has some clear drawbacks. First of all, as long as the model is carried out in two dimensions one has to estimate how many aggregates should be included in the simulation in order to give a good representation of the settling pattern. This drawback though can be eliminated by simulating in three dimensions, however then the calculation time increases. Another drawback is that since the model does not consider every single aggregate fully coupled it is necessary to estimate the viscosity of the surrounding fluid in which the aggregates settle. Finally, it is also a drawback for this model that no interaction between the aggregates is taken into account, which in this study lead to a situation where the volume fraction in some zones at the bottom of the formwork exceeded the maximum packing fraction. Most likely it would be possible in FLOW-3D to program a criterion saying that if the number of aggregates in a certain region is higher than some specific number, then the aggregates should not be allowed

to enter this region. However, the question would then be how large the size of this region is supposed to be. This drawback can either be solved with fully coupled particles (aggregates) or by introducing a scalar which represents the aggregate volume fraction, since the region in which the aggregates is not allowed to settle to implicitly lies in the definition of the mesh, cf. FLOW-3D model #2 in section 3.1.3.2.

5.2 Scalar Aggregate Representation

The FLOW-3D model #2 and MATLAB model both use the scalar aggregate representation as described in sections 3.1.3.2 and 3.2.3, respectively. In the next two subsections the FLOW-3D model is first used to investigate the settling pattern in an SCC-like model fluid and afterwards the MATLAB model is used to study the same but in a real SCC.

5.2.1 Carbopol Test (FLOW-3D Model #2, Paper II)

In Paper - II (Spangenberg et al., 2012b) the FLOW-3D model #2 with the scalar aggregate representation, cf. section 3.1.3.2, was used to investigate the settling pattern in an SCC like model fluid. In the first part of the paper different physical phenomena leading to flow induced aggregate migration were reviewed and with analytical expressions the dominating phenomena were determined for various applications. In the case of casting the gravity induced migration was found to be the leading factor, which thereby justified that this was the physical phenomenon considered by FLOW-3D model #2.

The model fluid consisted of a transparent polymer with the name Carbopol Ultrez and spherical glass beads, see Fig. 5.4. It was found that the behaviour of the carbopol gel could either be fitted with a Bingham material model with a yield stress of 40 Pa and a plastic viscosity of 1 Pas or with a Herschel Bulkley model with a yield stress of 40 Pa, a K value of 15.8 Pas and an n value of 0.48. The Bingham model parameters for the carbopol alone were approximated with the bi-viscosity model, cf. section 2.2.2, in order to predict the global flow of the glass beads and carbopol mixture, whereas the Herschel-Bulkley material model was used as one of the possibilities for description of the surrounding fluid's viscosity in which the glass beads settle. The volume fraction of the glass beads used in the experiment was 10% and due to this relative low volume fraction, the behaviour of the glass beads and carbopol mixture did not strongly differ from the rheological behaviour of the carbopol alone and was therefore neglected in the numerical simulations. A maximum volume fraction though was taken into account numerically by preventing the particles from moving into a CV, in which the dense packing fraction of spheres had already been reached (i.e. 64%). The density of the carbopol and the glass beads were 1000 kg/m³ and 2500 kg/m³, respectively. The experiment was performed by slowly pouring 6 l of the model fluid into a 0.2x0.2x0.6 m container at one end. The container was made of transparent plexiglas, enabling visual observation of the flow front propagation. The casting speed was approximately 0.1 l/s to minimize inertia effects, cf. (Nguyen et al., 2006) and (Roussel, 2006a). At the end of the casting shown in Fig 5.5, the model fluid was divided into 6 zones by insertion of metal plates, see Fig. 5.6. The content of each zone was then washed and the volume fraction of glass beads in a given zone was computed from the weight of the beads. The experiment was carried out with glass beads with three different diameters; 2, 5 and 7 mm.



Figure 5.4: *Homogeneous carbopol gel and glass beads mixture at the end of the mixing phase, Paper - II (Spangenberg et al., 2012b).*

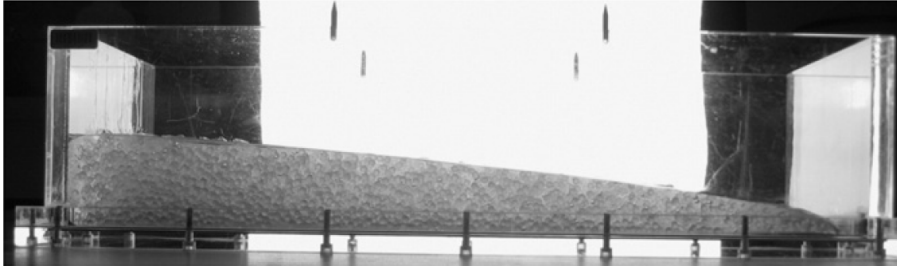


Figure 5.5: *Model formwork filled with the model material, Paper - II (Spangenberg et al., 2012b).*

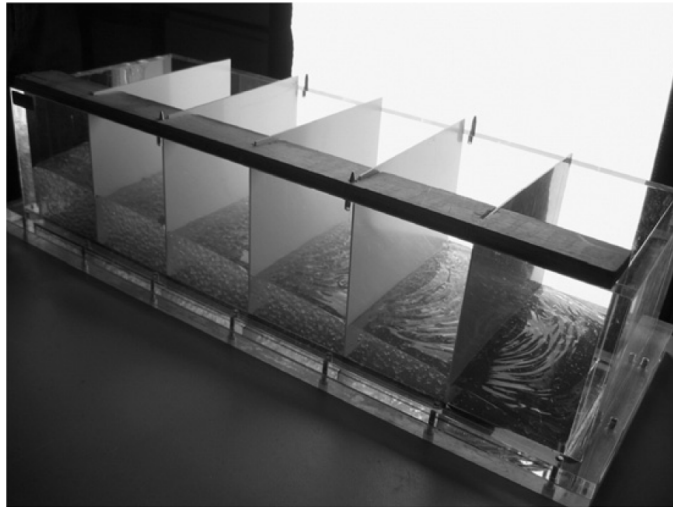


Figure 5.6: *Zones separation in the model formwork before weighing of beads, Paper - II (Spangenberg et al., 2012b).*

The measured glass bead volume fractions after the filling of the model formwork are reported in Fig. 5.7 for the three glass bead diameters. The figure illustrates that some particle migration was induced by the flow and that the model fluid became heterogeneous. This heterogeneity was increasing with the diameter of the glass beads and with the distance from the pouring point. After the flow propagation of 0.55 m, the volume fraction

decreased respectively from 10% to 8%, 3% and 1% for the 2, 5 and 7 mm beads. Close to the pouring point, the particle volume fraction was increasing as settling particles gathered at the bottom of the model formwork.

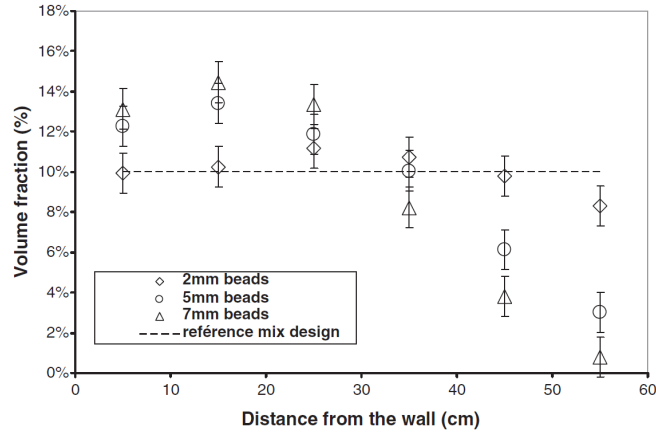


Figure 5.7: Measured glass beads volume fractions as a function of the distance in the model formwork, ref. Paper II (Spangenberg et al., 2012b).

In Fig. 5.8, the computed glass bead volume fraction as a function of the distance for three different assumptions regarding the value of the viscosity of the surrounding carbopol gel is plotted for the 5 mm beads. The numerical simulation underestimated the particle migration when the apparent viscosity was used as the viscosity of the surrounding fluid in which the glass beads were settling. If the plastic viscosity was used the simulations overestimated the particle migration, but the study showed that when using the tangential viscosity obtained from the Herschel-Bulkley material model it was possible to get a good agreement between the numerical result and the experiment. A good agreement was also found when simulating the other glass bead sizes with the tangential viscosity, see Fig. 5.9. These results suggested that the stresses generated by the weight of the mixture fulfilled the von Mises flow criterion and thereby initiating the flow. The density difference between the particles and the suspending fluid generated additional stresses in the system. As the von Mises criterion was already fulfilled by the contributions from the weight, these additional stresses only contributed to the viscous dissipation and did not have to exceed the yield stress to generate a relative flow between the particles and the gel. As a consequence, the settling process was the same as the one that would occur in a zero yield stress fluid. Therefore, the only parameter of interest was the tangential viscosity.

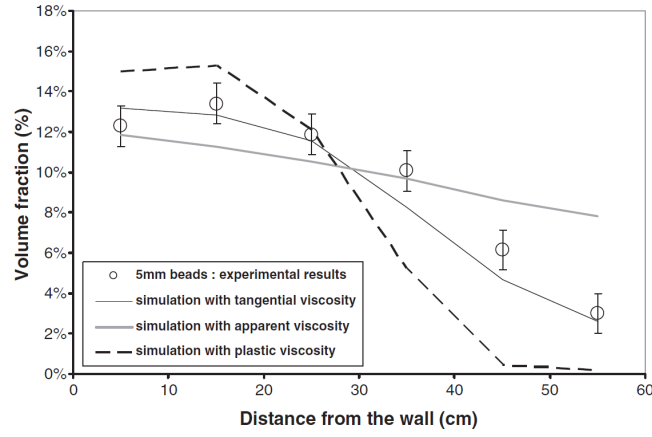


Figure 5.8: *Glass bead volume fraction as a function of distance for the 5 mm beads. Comparison between experimental results and numerical simulations for various assumptions for the viscosity of the suspending fluid. The yield stress is 40 Pa, Paper - II (Spangenberg et al., 2012b).*

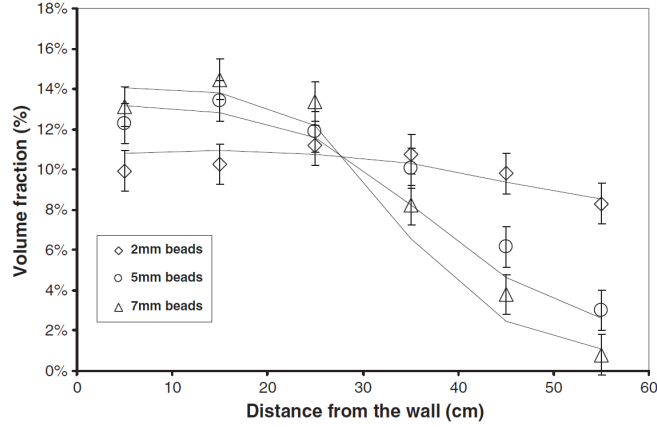


Figure 5.9: *Glass bead volume fraction as a function of distance for the 2, 5 and 7 mm beads. Comparison between experimental results and numerical simulations considering the tangential viscosity of the surrounding fluid, Paper - II (Spangenberg et al., 2012b).*

Discussion

A great advantage for FLOW-3D model #2 as compared to FLOW-3D model #1, with regards to prediction of gravity induced aggregate migration, is that it is capable of introducing a maximum volume fraction, which consequently means that it is not possible to have regions in the formwork where the aggregate volume fraction exceeds the dense packing fraction. Another strength of this model is that FLOW-3D allows for a scalar to be advected and afterwards manipulated in a user defined way (in this case a settling calculation), which definitely shortens the work load involved in implementing the scalar aggregate representation. There exist two main difficulties when expanding the approach proposed in this study to the case of real SCC. First, as the volume fraction of coarse aggregates in SCC is not in the order of 10%, but in the order of 40%, the local rheological properties need to depend on the local volume fraction of coarse aggregates. The problem of aggregates settling becomes therefore a coupled problem as it does not only create heterogeneity in component proportions but also heterogeneities in local rheological prop-

erties, which may in turn affect the global flow of the mixture and therefore aggregate settling pattern. For the scalar aggregate representation approach it is possible to take this dependency into account by implementing the equations in section 3.2.4, as done for the MATLAB model. Second, although the behaviour of the suspending fluid can be measured in the case of the model fluid used in this study, it is not the case for real SCC, since it includes aggregates in all sizes up to a couple of centimetres. Therefore, with the approach used in this study it is necessary to estimate the viscosity of the surrounding fluid in which the aggregates settle. An estimated value can be obtained by the use of experiments as seen in the study presented in the next subsection.

5.2.2 SCC Test (MATLAB Model, Paper III)

The MATLAB model with the scalar aggregate representation, see section 3.2, was used to predict gravity induced aggregate migration in two SCC beam cast experiments, cf. Paper - III (Spangenberg et al., 2012a). Two identical beams were cast with two different casting rates. The dimensions of the beams were length 4 m, width 0.2 m, and height 0.3 m, cf. Fig. 5.10. One beam was studied while the concrete was still fresh (low casting rate) while the other was studied after hardening (high casting rate). The beam studied in the hardened state was reinforced with two 8 mm bars for demoulding and transportation purposes. The concrete was poured directly and continuously from the concrete truck at a distance of approximately 0.3 m from one end of the beams. The pouring position did not change during the filling process in order to have as simple a casting scenario as possible. Consequently, the moulds were not fully filled and the filling process was stopped when concrete reached the top of the formwork closest to the pouring zone, cf. Fig. 5.10. For the lowest casting rate, the duration of the filling process was 160 s corresponding to a mass rate of concrete entering the formwork of 2.9 kg/s. For the highest casting rate, the duration of the filling process was 60 s corresponding to a mass rate of concrete entering the formwork of 7.7 kg/s. For the beam cast at the low casting rate, the induced horizontal heterogeneity was measured in the fresh state by measuring the aggregate content in the nine sub-regions illustrated on the sketch in Fig 5.10. After casting, some custom-made steel plates working as barriers were inserted in the concrete. The extracted fresh concrete samples were washed and sieved and the amount of aggregates belonging to the fractions 6/11 mm and 11/16 mm were measured. The beam cast at the high casting rate was cut in the middle of the nine sub-regions shown in Fig. 5.10 after setting. Image analysis of the vertical sections allowed for the determination of the concentration of 11/16 mm aggregates in three zones (upper, middle and lower zone) in each section. The thickness of each zone was approximately one third of the height in the specific cut. The rheological parameters for the SCC were obtained by the LCPC-box test and the T500. The yield stress was approximately 40 Pa, while the plastic viscosity was approximately 100 Pas. The dense packing fraction of the aggregates in the SCC was found to be 0.75. The SCC was tested for its static segregation resistance by placing aggregates of different sizes on top of a sample inside a bucket and showed no sign of static segregation.

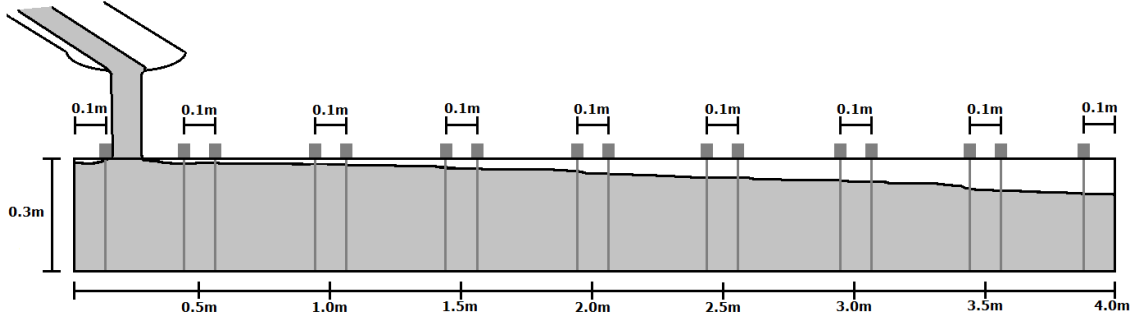


Figure 5.10: *Beam geometry and casting, Paper - III (Spangenberg et al., 2012a).*

Measurements of 6/11 mm and 11/16 mm aggregates volume fractions in fresh state by sampling and sieving are presented in Fig. 5.11. These two granular classes were initially present in the mix at the volume fractions of 17 and 16%, respectively. The measurements suggested that only the coarsest aggregates in the mix did migrate during flow. Moreover, as seen in the figure, there did not seem to be any segregation in the first two thirds of the beam where the aggregate volume fraction was more or less equal to the reference mix design volume fraction.

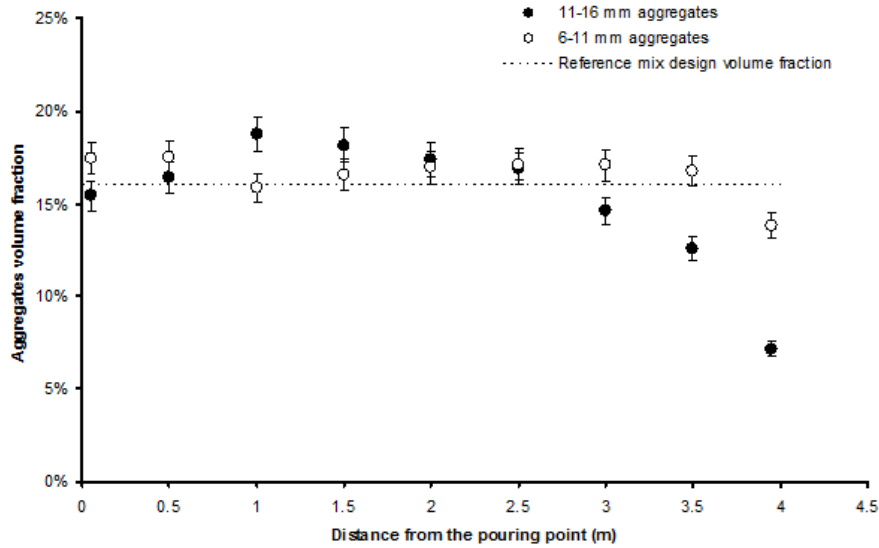


Figure 5.11: *Aggregate volume fraction measured in fresh state by sampling, washing and sieving as a function of the distance from the pouring end, Paper - III (Spangenberg et al., 2012a).*

However, the image analysis of the hardened cut samples showed that things were in fact more complex, cf. Fig. 5.12. Similarly to the measurements in fresh state, the total coarsest aggregates' volume fraction, after a plateau in the first two thirds of the beam, decreased in the last third. This suggested that, in most of the beam, the total volume fraction of aggregates in a vertical section was more or less equal to the reference mix design volume fraction. However, when focusing on the upper, middle and lower zone in each section, there existed a strong vertical heterogeneity in the sample as shown in Fig. 5.12 where a multilayer material seemed to be created. In this figure, the average value of the aggregates counting measurements in the first three meters of the beam are plotted. These results suggest that, in the upper zone, there is no segregation. They

moreover suggest that particle depletion from the middle zone results in an accumulation of particles in the lower zone. A peak in the aggregate volume fraction in the bottom zone was noted between 1 and 1.5 m from the pouring end of the beam.

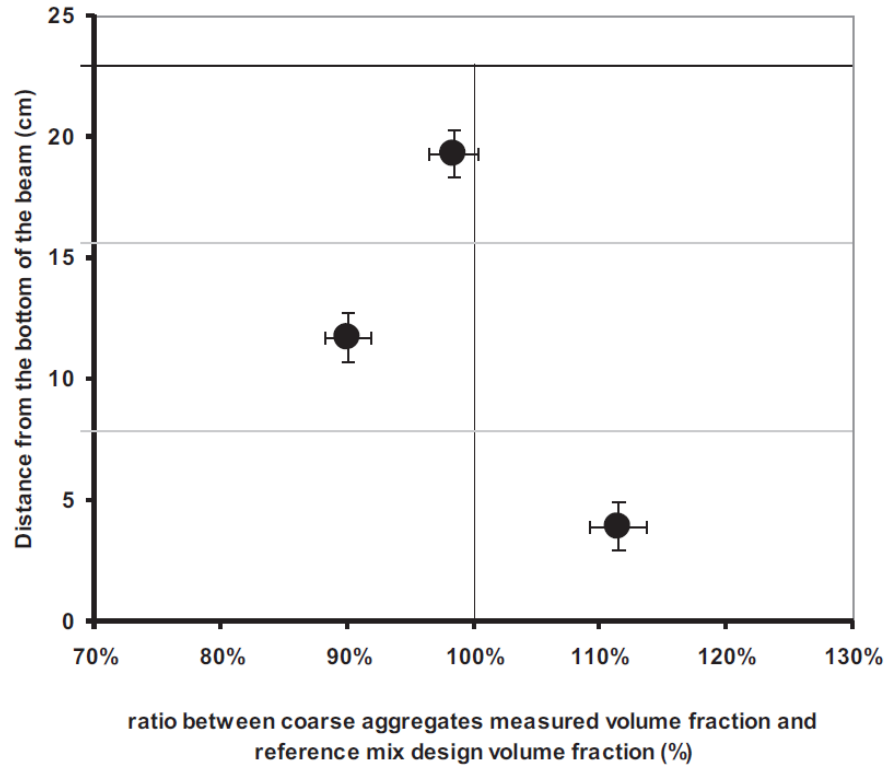


Figure 5.12: *The layered structure induced by segregation in the first three meters of the beam. The dashed line corresponds to the reference mix design volume fraction, Paper - III (Spangenberg et al., 2012a).*

A thorough analysis with analytical expressions justifying the necessity of using numerical tools to capture the migration patterns is presented in Paper - III (Spangenberg et al., 2012a). In the numerical simulation the aggregate fractions from 6/11 mm and 11/16 mm were considered in the settling calculation as spherical aggregates with a diameter of 8.5 mm and 14 mm, respectively. However, since the simulated aggregate fraction with the lowest diameter did only show a little or no segregation, as in the experiment (see Fig. 5.11), this fraction is not plotted for the numerical results in the following. The implementation of the viscosity of the surrounding fluid was carried out with the apparent viscosity divided by a parameter α . The parameter α was the only fitted parameter of this study. When α equalled 1, it meant that the surrounding fluid had the same behaviour as the tested SCC, but when it was greater than 1 it meant that the surrounding fluid had a lower particle volume fraction than the SCC itself.

The next step in this study focussed on the influence of the coupling between local rheological properties and local particle concentration variations due to gravity induced migration. In Fig. 5.13, the numerically predicted concentration profile along the beam for the coarsest aggregates (i.e. the ones that are the most prone to migration) are plotted both with and without the coupling when using $\alpha = 1.0$. It could be seen that the peak in aggregate volume fraction could not be simulated without the coupling. In addition, even if α was varied, this peak could not be obtained. In Fig. 5.14 the local aggregates' con-

centration cartography at the end of the casting process are plotted. The figure showed that both techniques predicted the formation of the multilayer structure as also observed in the experiment. However, without any coupling, the settled aggregates were dragged along with the flow and the peak in the settled aggregates concentration was located around 3 m from the pouring point. As the viscosity and yield stress of the material were not increasing with the local volume fraction, the zones where particles had migrated were still able to flow and advance in the beam. When the coupling was implemented, the settled aggregates did not flow anymore and the peak was located around 1 or 1.5 m from the pouring point as measured in the experiment. The viscosity and yield stress of the material strongly increased in these zones as the volume fraction tends towards the maximal packing fraction. These zones could not flow and a deposition zone was formed in the first meter or meter and a half.

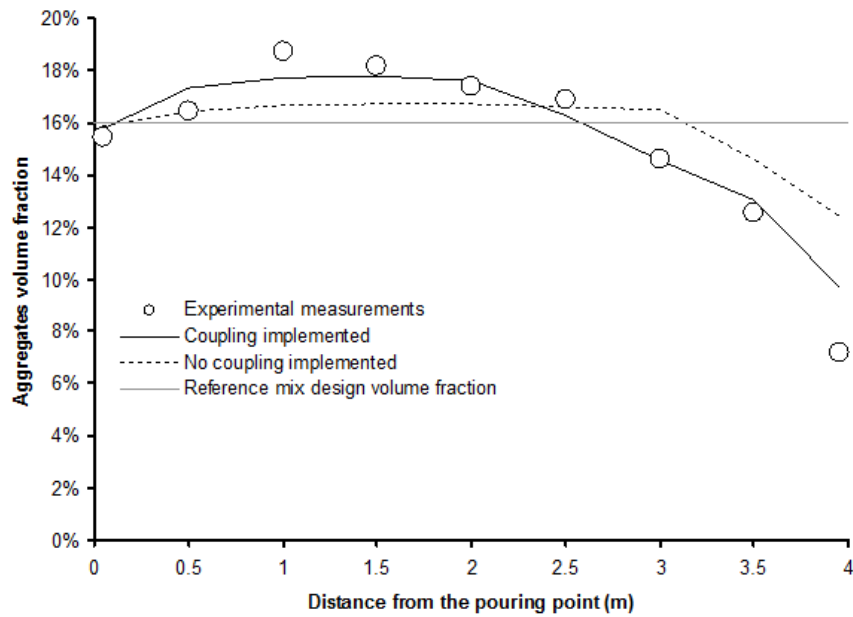


Figure 5.13: *Aggregates volume fraction as a function of the distance from the pouring end of the beam for low casting speed. Experimental measurements and numerical prediction with and without coupling, Paper - III (Spangenberg et al., 2012a).*

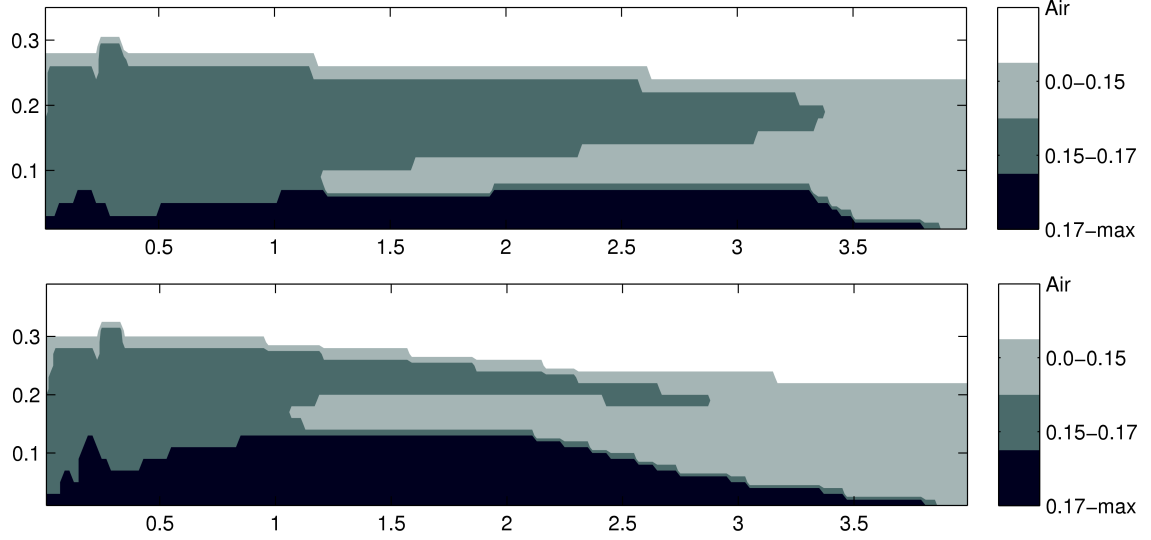


Figure 5.14: *Cartography of local aggregates volume fraction. (top) simulations with no coupling implemented (bottom) simulations with coupling implemented. Vertical and horizontal distances are in (m), Paper - III (Spangenberg et al., 2012a).*

Afterwards, an attempt was made to identify the best value for α . In order to reach the best agreement with the measured horizontal coarse aggregates concentration profile, α was fitted and the value of 1.45 was obtained. It was interesting to note that the value of the local apparent viscosity of the fluid surrounding the settling aggregates seemed to be 30% lower than the local apparent viscosity of the concrete. This suggests that the particles were settling in a material slightly more fluid than the concrete itself. The consequences of the gravity induced particle migration process were therefore not dictated by the behaviour of the concrete itself or the behaviour of its constitutive cement paste alone. Considering Eqns. (2.33) and (2.34), a value of 1.45 for α suggests that the viscosity of the surrounding fluid corresponds to the viscosity of the concrete studied here but depleted of its coarsest particles. The numerical simulations gave access to the shear rate and coarse aggregates vertical profiles in the beam, cf. Fig. 5.15. It was interesting to note that, contrarily to the case when no migration occurs in which the shear rate is maximal at the bottom wall interface, here the shear rate reached its maximal value at the deposition zone. This highly sheared zone had a lower apparent viscosity and was subjected to a fast particle depletion, which further reduced its viscosity, amplifying the gravity induced particle migration and turning it into a deposition process.

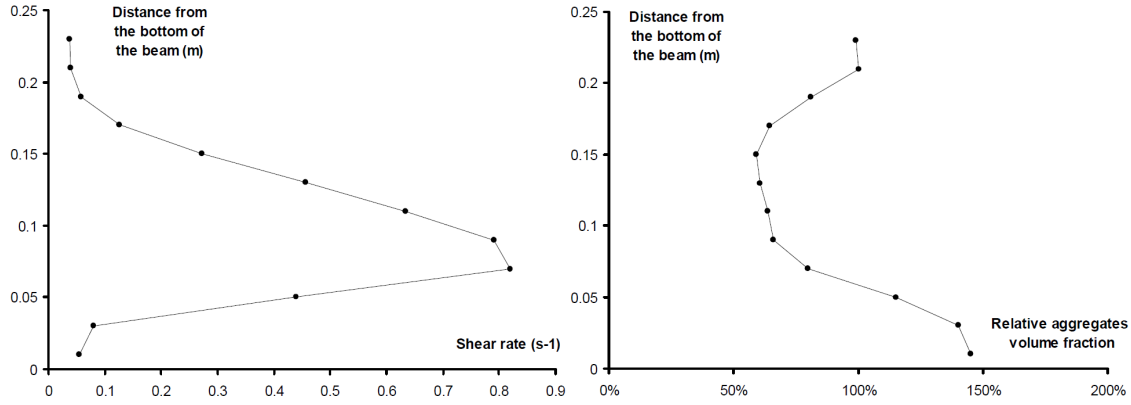


Figure 5.15: (left) Shear rate profile at the centre of the beam (right) Ratio between aggregates concentration and reference mix design concentration at the centre of the beam, Paper - III (Spangenberg et al., 2012a).

In Fig. 5.16 the results of the simulation with $\alpha = 1.45$ for the two casting rates together with the experimental results are shown. Based on the figure it was concluded that this simple numerical model with only one fitted parameter was able to predict the influence of casting rate on gravity induced aggregate migration. It was moreover noticed that increasing the casting rate decreased the magnitude of particle heterogeneities. Although increasing casting velocity for shear thinning materials such as SCC reduces the suspending fluid viscosity, it also decreases the time during which particles are migrating. Both experimental and numerical results obtained in this work confirm the hypothesis in Paper II (Spangenberg et al., 2012b) on model materials, which suggested that it was the time effect which dominated and that, therefore, increasing casting velocity decreased the induced horizontal heterogeneity.

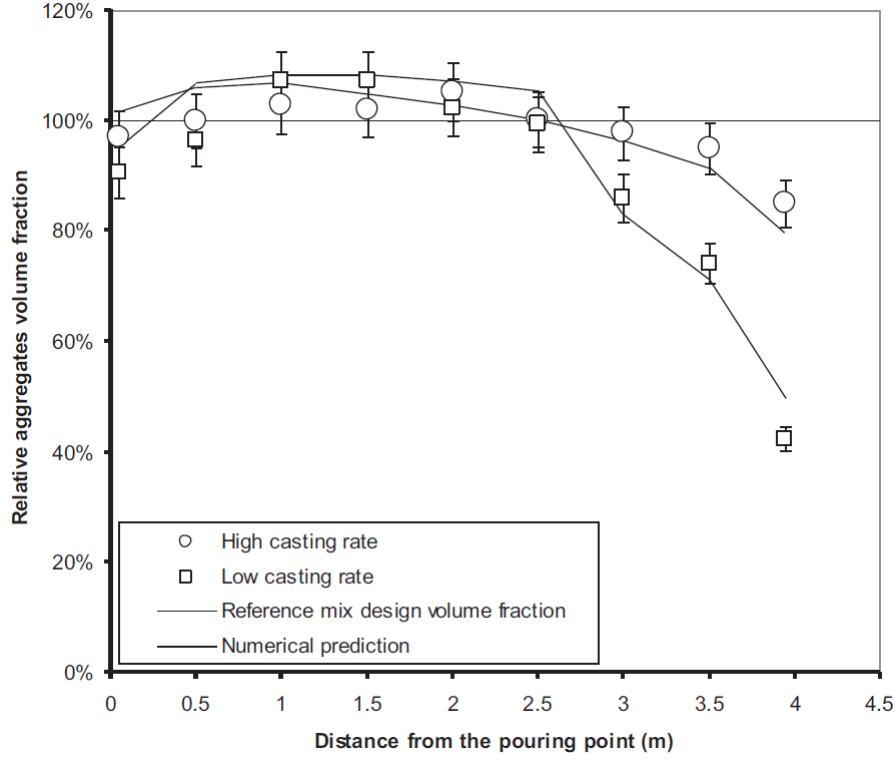


Figure 5.16: *Relative aggregates volume fraction (i.e. ratio between local aggregates volume fraction and reference mix design volume fraction) as a function of the distance from the pouring end for the low and high casting rate, Paper - III (Spangenberg et al., 2012a).*

Discussion

This study shows that the settling of aggregates in a material slightly more fluid than concrete itself as well as the coupling back from the aggregates to the rheological parameters are two important phenomena which need to be taken into account. In the previous study of the model fluid it was also found that the first of these two phenomena had to be addressed and the effect was implemented by the use of the tangent viscosity. However, in this study the tangent viscosity is not available and the effect is therefore taken into account via the α parameter. The implementation of the coupling back from the aggregates to the rheological parameters is straightforward for the scalar aggregate representation, however if this effect is supposed to be implemented for the discrete aggregate representation used in the FLOW-3D model #1 it would be much more comprehensive, since the same difficulties as mentioned in section 5.1 are implied in converting the aggregate distribution into a volume fraction map. The most important observations of this study from a numerical point of view are that this rather simple model is capable of capturing the first order effects of the gravity induced aggregate migration patterns in the two beams and that it can be used to investigate the formation of the multilayer and deposit zone. However, the obstacle with the scalar representation model is still the need of using the α parameter, because even though this study showed that it was possible to predict the settling pattern in two different beams with the use of the same α parameter, it is still unknown how this parameter changes when changing the composition of the SCC. This is the primary challenge if the numerical model with scalar aggregate representation

is supposed to be used as prediction tool for SCC casting in the future. In addition, to this discussion it should be mentioned that the α parameter never comes into play if a fully coupled model is developed. However, most likely such a model experiences other obstacles such as the cut of value for the size of the aggregates which are actually modelled as an aggregate and modelled as being a part of the suspending fluid and the determination of the rheological parameters of the suspending fluid. Moreover, the fully coupled model needs to be carried out in three dimensions and is therefore undoubtedly more computational heavy.

5.3 Optimization

In the two optimization studies included in this thesis, an evolutionary single objective genetic algorithm (SOGA) was applied to optimize the aggregate distribution while casting with SCC in order to get a uniform distribution of aggregates. In mathematical terms this objective was defined as minimization of the standard deviation of the volume fraction scalar at the end of the casting. Evolutionary algorithms (EAs) are non-deterministic (stochastic) methods that mimic evolutionary principles, e.g. natural selection and the survival of the fittest, to constitute their optimization strategy. They work with a set of solutions (population) instead of a single point as in traditional (classical) methods and this gives an opportunity to attack a complex problem (discontinuous, noisy, multi-modal, etc.) in different directions allowing the algorithm to explore as well as exploit the search space. This capability gives an advantage for having a more robust search strategy compared to traditional mathematical programming algorithms. Since they do not need any gradient information, they are very suitable for black-box (e.g. commercial software) optimization applications, i.e. the coupling to FLOW-3D in one of the studies.

Only a relatively limited work is published for numerical optimization of casting processes in general. One limiting factor is computational power which inhibits running multiple simulations with high accuracy within reasonable time. Another is that only a limited number of simulation software packages are coupled with optimization modules. These limitations eventually determine what is in fact possible today and hence determine what the "state-of-the-art" is. One example of exploiting numerical simulation of casting together with numerical optimization deals with increasing the casting yield via riser optimization meanwhile reducing the porosity in a gravity sand-cast steel part, cf. (Kotas et al., 2010).

SOGA is a single objective genetic algorithm (GA) which uses binary encoding for the representation of the design variables. The initial population, represented by binary strings of different lengths for each design variable, is composed of randomly distributed solutions in the design space. The algorithm is based on several genetic operators: binary tournament selection, single-point crossover and uniform mutation, cf. (Goldberg, 1989). Moreover it is an elitist algorithm which means that the best solutions found so far are preserved to accelerate convergence towards true or near optimum while still having explorative search to avoid premature convergence. The binary tournament selection implemented in SOGA is composed of two tournaments in which every individual compete only once in each. The other genetic operators are implemented in a standard way, cf. (Deb, 2001).

5.3.1 Feasibility Study (FLOW-3D Model #2, Paper IV)

The FLOW-3D model with the scalar aggregate representation was used to carry out an optimization study, where the objective was to obtain a homogeneous aggregate distribution in a beam casting, cf. ref Paper IV (Spangenberg et al., 2011). The study was a feasibility study and used estimated material properties much similar to the ones used in the study presented in section 5.1 (Paper I). The investigation was carried out on a 0.5 m high and 3 m long beam and was simulated in these two dimensions. The boundary conditions for the simulations are shown in Fig. 5.17. The rheological parameters for the simulated SCC was a yield stress of 50 Pa and a plastic viscosity of 50 Pas. The density of the SCC was 2200 kg/m^3 and the density of the aggregates was 2700 kg/m^3 . The aggregates considered for the settling calculation corresponded to the 25% coarsest particles in the SCC. The coarsest aggregates were modelled as spheres with a diameter of 14 mm. The volume fraction of the aggregates in the SCC was assumed to be 0.64 when it was homogeneous and the maximum volume fraction allowed was modelled to be 0.8. In this study the viscosity of the surrounding fluid in which the aggregates were settling, was estimated to be 0.5 times the viscosity of the global flow.

The vertical position of the inlet was 0.4 m from the bottom of the mould in all simulations, while its horizontal position was one of the three process parameters, which were varied for the optimization investigation. The horizontal position of the inlet was varied between 0.1 m and 1.5 m (which was the middle of the beam). The second varied process parameter was the inlet size and it was varied between 0.05 m and 0.08 m. The final process parameter was the mass rate and it was varied between 1.0 kg/s and 1.66 kg/s, which corresponded to a filling duration between 20 s and 35 s.

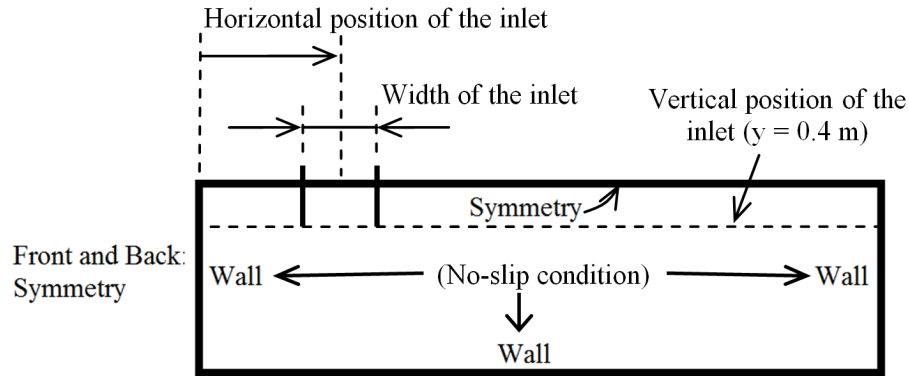


Figure 5.17: Boundary conditions, ref. Paper IV (Spangenberg et al., 2011).

The optimization procedure shown in Fig. 5.18 was executed from the MATLAB environment and it included a process integration of FLOW-3D and the optimization algorithm SOGA. The optimization cycle was initiated by creating an initial population of 20 randomly distributed set of design variables, i.e. the horizontal position and the size of the inlet as well as the mass rate. The total number of generations was 10 and the probabilities for the single point crossover and mutation operators were, 0.65 and $1/li$ (li : total string length). The design variables were updated by the optimization algorithm (i.e. SOGA) and were provided as an input for the flow simulation. Then the volume fraction scalar in each CV was saved at the end of the simulation. The standard deviation of the volume fraction was afterwards calculated by the optimization algorithm and used as the fitness of the design set to be minimized. This optimization cycle ran until the stopping

criterion, i.e. the total number of generations, was reached.

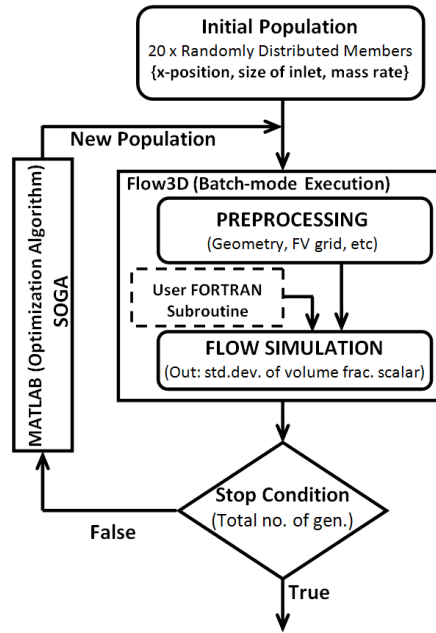


Figure 5.18: Flowchart of the optimization problem, ref. Paper IV (Spangenberg et al., 2011).

The results obtained from the optimization study are seen in Fig. 5.19. The figure shows the generations as a function of the standard deviation (fitness) for the best individual and for the average of all individuals. The algorithm found an improved solution in the third generation and the best solution in the fifth generation. The results showed that the final casting solution improved with approximately 11% and 20% as compared to the average of the first generation and the worst solution, respectively. The optimum process parameters obtained were; a horizontal position of 0.88 m, an inlet size of 0.074 m, and a mass rate of 1.66 kg/s. The study clearly showed that increasing the casting speed is beneficial as also documented in section 5.2.2. Regarding the inlet size, the optimization data showed that by increasing this a better solution could be obtained, if the same horizontal position and mass rate were used. However, the improvement was negligible as compared to the improvement of the solution when increasing the mass rate. Finally, the optimization showed that a more homogeneous aggregate distribution was produced when casting at 0.88 m as compared to casting in the middle.

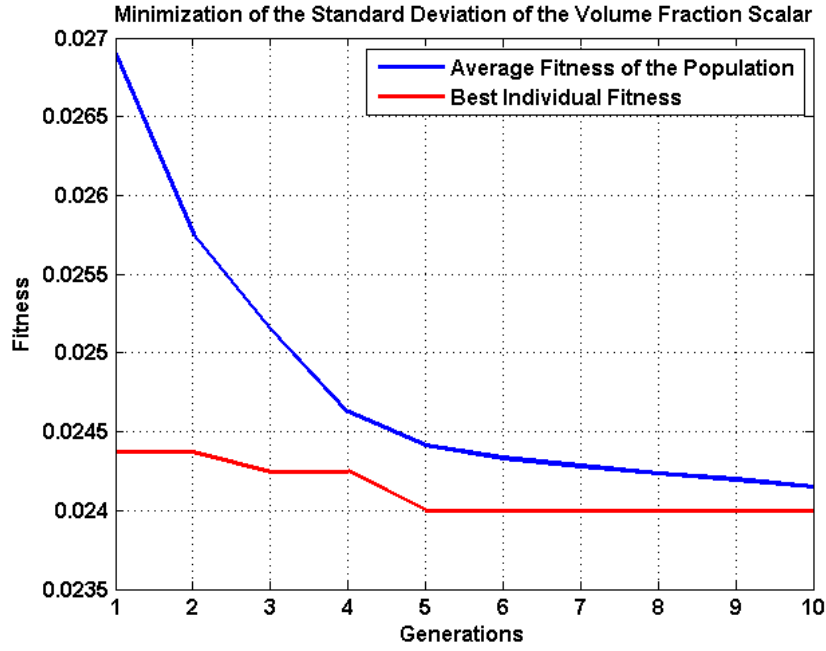


Figure 5.19: *Generations as a function of the standard deviation for best individual and average individuals, ref. Paper IV (Spangenberg et al., 2011).*

In Fig. 5.20, the volume fraction is shown in the last time step of the simulation for both the optimal solution (now referred to as beam_{opt}) and for the simulation with the optimum parameters for inlet size and mass rate, but with a horizontal inlet position in the middle of the beam (now referred to as $\text{beam}_{\text{middle}}$). Note, that the maximum contour limit in Fig. 5.20 is 0.16 which corresponded to the homogeneous value in order to highlight the areas where aggregates were immigrated from. The improvement by using beam_{opt} as compared to $\text{beam}_{\text{middle}}$ was approximately 3%. Even though this improvement is small and difficult to detect in Fig. 5.20, it showed that despite the reduction in the number of process parameters included in the optimization study and the simple geometry, the complexity involved in the casting process resulted in a non trivial optimal design set. However, Fig. 5.20 showed another important issue which was that $\text{beam}_{\text{middle}}$ obtained a zone where the aggregates were immigrated from on both sides of the inlet, while beam_{opt} primarily obtained such zone on the side of the inlet where the longest flow distance to the end of the mould was present. This issue opened the discussion whether the standard deviation was a satisfactory criterion to evaluate the casting process of the beam, e.g. it could be that the size of the immigrated zone was equally or more important for the beam as compared to the standard deviation of the volume fraction. Actually, the best possible criterion would be if the aggregate distribution was found based on a load case scenario for the beam and then using that aggregate distribution as the optimal solution. However, such a scenario was not included in this study (or other optimization studies in this thesis).

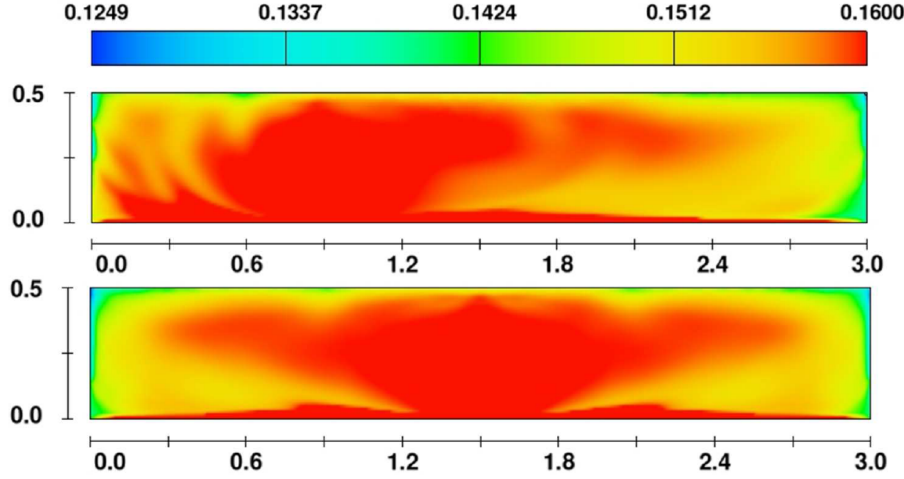


Figure 5.20: *Volume fraction of coarse aggregates in the last step for $beam_{opt}$ and $beam_{middle}$, ref. Paper IV (Spangenberg et al., 2011).*

Finally, the study sheds a light on the robustness topic. The optimal process parameters are accessed to be robust if a small deviation from them does not change the solution critically, which was the case in this study, cf. ref. Paper IV (Spangenberg et al., 2011). The robustness issue is especially important in optimization of SCC castings, since it is a process carried out by humans. Therefore, it is of no interest to find an optimal solution which is ruined if the hose is offset in the horizontal position by 0.91 m, instead of 0.88 m.

Discussion

The obvious drawback of this model is the usage of a viscosity multiplier of 0.5 which is too low if compared to the value found in ref. Paper - III (Spangenberg et al., 2012a). However, when discussing this study on the premise that it is a feasibility study, the model has some very important advantages. First, the coupling between the optimization algorithm and FLOW-3D is not too comprehensive to set up, both because FLOW-3D allows to be executed in batch mode, but especially since the post processing part where only some specific data should be delivered to the optimization algorithm is very intuitive in FLOW-3D. Second, each simulation took only one hour, which is most likely the most essential key to carry out an optimization study. The disadvantage of the need for a fast simulation is that it can conflict with the numerical accuracy and the physics included in the model. In this study the most important simplifications, when relating this to a real beam casting were that only one inlet was used and particularly that it was necessary to model the mould with a boundary at the top, which did not allow the SCC to overflow the mould. In section 5.3.2 an investigation is presented where some of the disadvantages of this study, such as only one inlet and no free surfaces at the top are attempted to be solved.

5.3.2 Case Study (MATLAB Model, Technical Report - II)

In Technical Report - II the MATLAB model with the scalar aggregate representation (cf. section 3.2.3) was used together with SOGA to optimize a beam casting much similar to the one presented in the previous section. However, four important differences between these two studies were; the usage of a numerical model which included the aggregates effect on the rheological parameters, the deployment of material properties from Paper - III (Spangenberg et al., 2012a), the use of up to three inlets with varying filling durations instead of one inlet, and also the addition of three constraints.

Fig 5.21 shows the geometry of the beam and as before due to computational speed the aggregate distribution in the beam casting was predicted based on a two dimensional simulation, thus the reinforcement is assumed to be arranged in such a way that it has negligible effect on the settling pattern. In addition, it is assumed that the settling pattern in two dimensions is representative for the settling pattern in three dimensions for the beam. All the boundaries were modelled as walls with zero velocity at the surface; however, since a mould is not closed in real life at the top, the upper boundary did not come into play. The three inlets were placed at 0.5 m, 1.5 m, and 2.5 m from the one end of the beam and the width of the inlets were 0.1 m each, see Fig. 5.21.

The process parameters varied in this optimization study were the sequence in which the inlets are filling and their individual filling duration. The total filling duration was 28.8 s for all of the simulations and the mass rate was kept constant. Three constraints were taken into account in order to find realistic and usable casting scenarios. The first constraint was a limitation on the free surface height of the SCC, because the yield stress behavior makes the free surface differ from a horizontal straight line. Consequentially, a casting scenario could occur where SCC would flow beyond the edge of the mould in real life. The overflow of the mould was not taken into account in the numerical model, but in order to prevent such a scenario the simulation was terminated if the free surface of the SCC reached a height greater than 4 cm above the edge of the mould. The second constraint was a limitation on the minimum height. A casting scenario where the minimum height of the free surface at the end of the casting was less than 4 cm from the mould edge was also prohibited. The third and final constraint was a minimum volume fraction limitation. The volume fraction of the coarsest aggregates was not allowed to be less than 10% anywhere at the end of the simulation.

The aggregate volume fraction considered to effect the rheological parameters was the aggregates from 6 to 16 mm in Paper - III (Spangenberg et al., 2012a), whose volume fraction corresponded to 0.33 when homogeneous. The aggregates allowed to settle in this study were the aggregates from 11 to 16 mm only and they had a volume fraction of 0.16. This change was made in order to decrease the memory use and calculation time of the simulation. The simulated aggregates were modelled as spheres with a diameter of 14 mm and the α parameter equalled 1.45 as found in Paper - III (Spangenberg et al., 2012a).

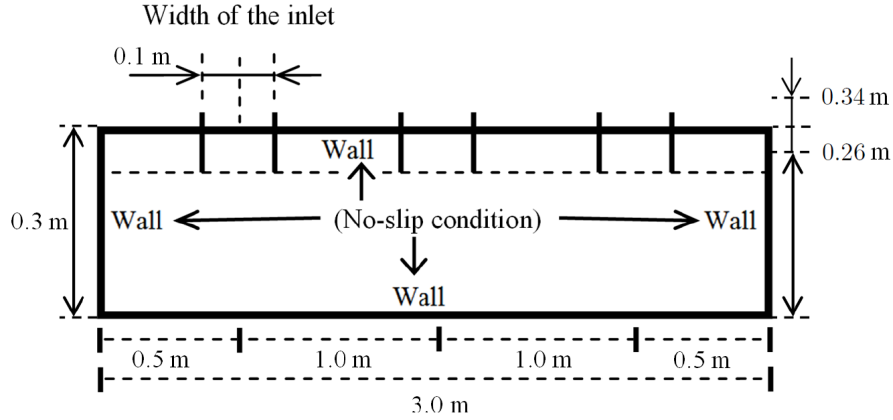


Figure 5.21: Inlet position and boundary conditions, *Technical Report - II*.

The flowchart for the optimization problem was much like the flowchart shown in Fig. 5.18. The primary difference is that the simulation is carried out with the MATLAB model instead of the FLOW-3D model #2 as shown in the figure.

The numerical results of a form filling with one inlet (i.e. in the middle) are illustrated in Fig. 5.22. The evolution of the casting process is shown at three different points.

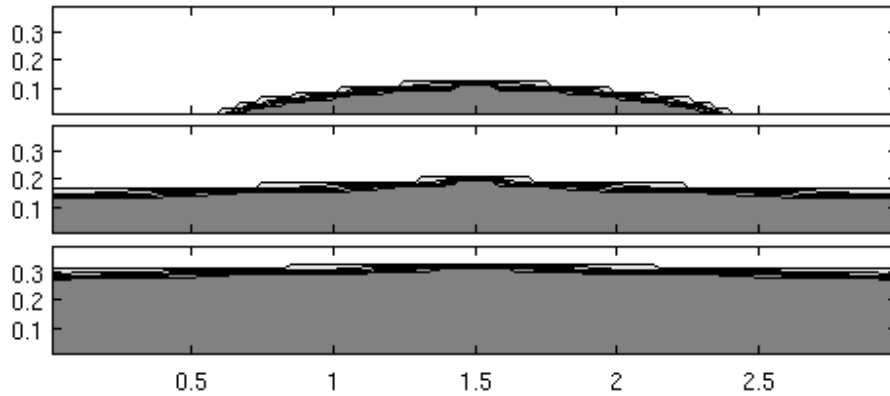


Figure 5.22: The evolution of the casting process, *Technical Report - II*.

The objective and constraint results obtained for the case shown in Fig. 5.22 are presented in Tab. 5.1 together with results from simulations carried out using two and three inlets. The simulation with two inlets initiated the form filling with the middle inlet and finalized with the left one. Each was active for 14.4s. The simulation with three inlets was also initiated with the middle inlet and finalized with the right inlet. Each of them was filling for 9.6s.

Model	Std. dev. ϕ	Min. ϕ	Max. Height	Min. Height
One Inlet	0.0156	0.1204	Ok	0.29
Two Inlets	0.0168	0.1216	Ok	0.28
Three Inlets	0.0154	0.1148	Ok	0.27

Table 5.1: Results from parameter study, *Technical Report - II*.

The brief parameter study shown in Tab. 5.1 clearly indicates the high non-linearity in-

volved in the problem and therefore how difficult it is to predict the best casting technique, e.g. one would expect that it is preferable to use two inlets as compared to one. However, in this specific case the results show that the standard deviation was lower when using the single inlet (the middle). In addition, the table shows that the standard deviation and minimum aggregate volume fraction were not fully correlated. In order to understand the correlation between the standard deviation and the minimum volume fraction a multi objective optimization study could be carried out in which the minimum volume fraction constraint was converted to an objective on its own. However, in this study the single objective was kept and in Fig. 5.23 the results of this optimization analysis are shown. The figure shows the standard deviation as a function of the generations for the best individual and the average of all individuals. Note, that the infeasible solutions were not taken into account when finding the average value.

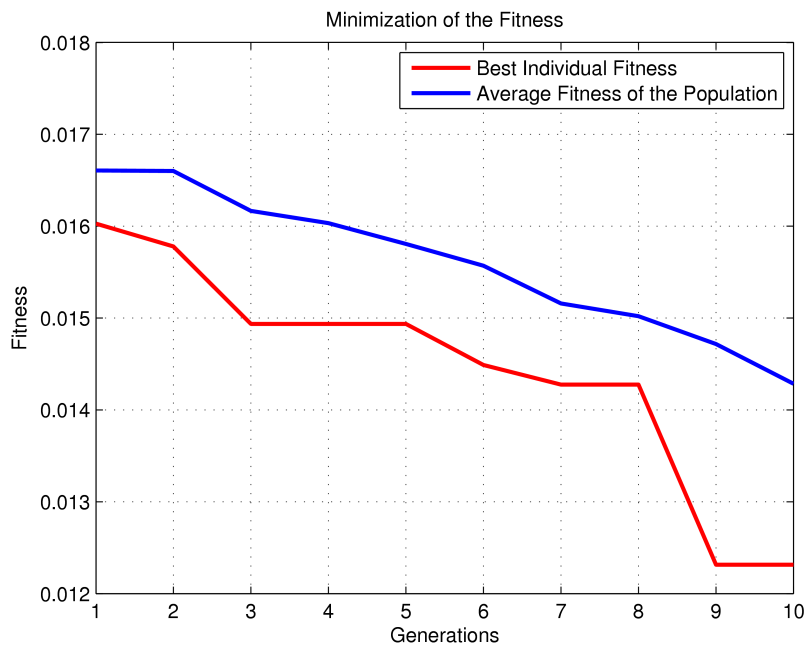


Figure 5.23: *Generations as a function of the standard deviation for best individual and average individuals, Technical Report - II.*

Fig. 5.23 shows that the best solution improves five times within the ten generations and ends up with the final result at the ninth generation. Most likely, it would be possible to obtain a better solution if the number of generations and individuals in each generation were increased. However, in order to run the optimization study within a reasonable time, ten generations and ten individuals were used. The process parameters for the best solution were; a casting initiation at the left inlet, followed by the middle inlet and finalizing with the right inlet. The casting durations were 8.6 s at the left inlet, 17.1 s at the middle inlet, and 3.1 s at the right inlet. This casting scenario led to a standard deviation of 0.0123, a minimum volume fraction of 0.13, an acceptable maximum height, and a minimum height of 0.28 m. The best casting scenario obtained improved the standard deviation with 20% and the minimum volume fraction with 13% as compared to using three inlets with the same filling duration, cf. Tab. 5.1. Another interesting observation was that the best solution was obtained when the third (the right) inlet is almost inactive, which was also a non-intuitive pattern.

Discussion

As mentioned in section 1.3 the MATLAB model was developed due to flexibility issues. In the present study this is especially seen in the dynamic constraint handling, which would be more cumbersome to handle in FLOW-3D. The constraints implemented in this study enables the casting scenarios to be more realistic than the ones investigated in section 5.3.1. However, the handling of the overflow of the mould can still be improved in order to have even more realistic casting scenarios e.g. it could be implemented that a free surface of 4 cm above the edge of the mould is accepted in the middle, where the thickness of the beam may prevent the SCC from overflowing the mould, but not at the ends of the mould where only the thickness of the mould prevents the SCC from overflowing. In addition, the implementation of a filling stoppage could be implemented in order for the SCC to be more levelled and thereby preventing it from overflowing. Another obstacle arising if the MATLAB model coupled with the optimization algorithm is supposed to be used as a predicting tool for SCC castings (other than the usage of the parameter α) is the calculation time. In this study the calculation time was 1 hour for a 0.3x3 m beam, which enabled all of the simulations to be finish in reasonable time of 4 days. However, if for instance a large wall is the evaluated structural part, the calculation domain and time would increase thus the optimization study would most likely be too time consuming. This drawback could though be limited by e.g. only considering the most crucial part of the wall or introducing some numerical improvements to speed up the model. This speed up could be obtained by programming in C or Fortran or by splitting the pressure and velocity calculation like the algorithm used in FLOW-3D.

Chapter 6

Summary of Appended Papers

In this chapter a short summary of the four appended papers and the two technical reports is given.

6.1 Paper - I

J. Spangenberg, N. Roussel, J. H. Hattel, J. Thorborg, M. R. Geiker, H. Stang, and J. Skocek (2010). Prediction of the impact of flow-induced inhomogeneities in Self-Compacting Concrete (SCC). In K. H. Khayat and D. Feys (Eds.), *Design, Production and Placement of Self-Consolidating Concrete: Proceedings of SCC2010, Montreal, Canada, September 26-29, 2010*, Volume 1 of *RILEM State of the Art Reports*, pp. 209-215. Springer Netherlands.

In this paper, a numerical simulation with a discrete aggregate representation is used to predict the flow induced aggregate migration in an SCC beam casting. A one way momentum coupling is used between the aggregates and the surrounding fluid in the model developed in the CFD-software FLOW-3D. The final simulated aggregate distribution is translated to a volume fraction map which afterwards together with semi-empirical relationships is converted to property maps for the hardened state SCC. The relative drying shrinkage strain showed the highest variation.

6.2 Paper - II

J. Spangenberg, N. Roussel, J. H. Hattel, H. Stang, J. Skocek, and M. R. Geiker (2012). Flow induced particle migration in fresh concrete: Theoretical frame, numerical simulations and experimental results on model fluids. *Cement and Concrete Research* 42 (4), 633-641.

This paper presents a review of the different physical phenomena leading to flow induced aggregate migration and with analytical expressions it determines the dominating phenomenon in various applications. In castings it is found that gravity induced migration is the leading factor. Subsequently, a FLOW-3D model considering gravity induced migration is used to predict the settling pattern in three model fluid castings carried out with different sizes of particles. The simulations are executed with a scalar particle representation and shows a good agreement with the experiments when using a tangential viscosity in the settling calculation.

6.3 Paper - III

J. Spangenberg, N. Roussel, J. H. Hattel, E. V. Sarmiento, G. Zirgulis and M. R. Geiker (2012). Patterns of gravity induced aggregate migration during casting of fluid concretes, *Cement and Concrete Research*, Accepted.

In this paper the migration patterns are measured in two experimental SCC beam castings with different casting rates. The measurements for the beam with the lowest casting rate is carried out while the concrete is in its fresh state and it shows that primarily the coarsest aggregates are prone to settling. The measurements for the other beam are performed after the SCC is hardened and shows that a multi-layer structure appears in the beam's vertical direction. Then, a numerical model developed in MATLAB captures the migration patterns in the horizontal and vertical directions of the beams with a scalar aggregate representation and an estimated value for the viscosity of the surrounding fluid, which is in between that of mortar and SCC scale. Finally, both experimental and numerical results confirm that high concrete casting rates reduce the magnitude of gravity induced particle migration.

6.4 Paper - IV

J. Spangenberg, C. Tutum, J. H. Hattel, N. Roussel, and M. R. Geiker (2011). Optimization of casting process parameters for homogeneous aggregate distribution in self-compacting concrete: A feasibility study. In *Evolutionary Computation (CEC), 2011 IEEE Congress on*, pp. 2163-2169.

This paper presents an optimization analysis of an SCC beam casting with respect to obtaining a homogeneous aggregate distribution. The investigation is conducted with a single objective genetic algorithm coupled with a FLOW-3D model with a scalar aggregate representation. Despite limited process parameters included in the study, a non trivial optimal solution is found. In addition, the paper discusses the importance of a fast calculation and a robust optimal casting scenario.

6.5 Technical Report - I

J. Spangenberg and J. H. Hattel (2012). A CFD Solver for Simulation of Flow of Self Compacting Concrete.

In this technical report, the discretization of the velocity and pressure equations for a non-Newtonian CFD solver is presented together with the wall boundary condition.

6.6 Technical Report - II

J. Spangenberg, C. C. Tutum, and J. H. Hattel (2012). Optimization of Casting Process Parameters for Homogeneous Aggregate Distribution in Self-Compacting Concrete: A Case Study.

This technical report presents an optimization study similar to the one carried out in Paper IV (Spangenberg et al., 2012b), however with modifications enabling the optimal

casting scenario to be more realistic, e.g. constraints for the maximum and minimum height of the SCC at the end of the casting are introduced as well as a constraint for the minimum volume fraction of the coarsest aggregates. In addition, the possibility of using up to three inlets is included in this study. The investigation shows that the optimization algorithm improved the casting technique with 20%.

Chapter 7

Conclusion and Future Work

In this chapter the conclusions of the three investigations are summed up and a description of the future perspectives within the field of numerically predicted gravity induced aggregate migration and optimization of SCC form fillings is given.

LCPC-box test:

- The LCPC-box test study showed that a relative good agreement between the analytical solution and the numerical results could be obtained for both the FLOW-3D and the MATLAB model. Furthermore, the study identified that the agreement improved when the initial viscosity was increased. Consequently, it could also be concluded that it is impossible for the applied numerical models to be in full agreement with the analytical solution, since an infinitely high initial viscosity cannot be handled by the CFD solver. Another drawback with the LCPC-box test is that it is necessary to fit the numerical results' spread length to the one of the analytical solution. However, there are definitely also advantages with the LCPC-box test e.g. it gives a good understanding of the bi-viscosity material model and the error introduced when using it to mimic a yield stress fluid. The test pinpoints which mesh density, time step and initial viscosity are working for the specific CFD code and finally the flow involved in the LCPC-box test is very similar to the flows that the CFD code afterwards should be used for e.g. casting of a beam, a wall or a slab. Based on the pros and cons of the LCPC-box test it can be concluded that the test should be used with some caution for the reasons stated above when validating an FDM/FVM based CFD solver with a bi-viscosity model, but it is a highly recommended test to carry out in order to get a better understanding of the numerical settings working for the CFD solver.

Numerical prediction of gravity induced aggregate migration:

- This investigation showed that it was possible for the MATLAB model with the scalar aggregate representation and the coupling back from the aggregates to the rheological parameters to obtain the same horizontal and vertical migration pattern as observed in two beam castings. Moreover, the numerical simulations suggested that the viscosity of the fluid surrounding the migrating particles is of the same order as the viscosity of the equivalent concrete without the migrating particles and confirmed that high concrete casting rates reduce the magnitude of gravity induced particle migration. In addition, the investigation showed that in order for FLOW-3D model #1 with the discrete representation to be capable of predicting

settling patterns like the MATLAB model, quite a lot of additional programming would be necessary e.g. converting the aggregate distribution into a volume fraction map, introducing a maximum fraction criterion, and including the coupling back from the aggregates to the rheological parameters. However, in the case of FLOW-3D model #2 only the latter needs to be implemented, which would not be too comprehensive. The study showed also a downside to the MATLAB model which was the need of the parameter α . The α parameter did not seem to change when changing the casting velocity, which is definitely an important observation for the applicability of this approach, but only a future study will show how it changes with different mix compositions of the SCC. In such a study it would be very interesting to correlate the α parameter to the rheological parameters of the SCC. As a result, if this correlation describes an applicable relationship, then this not too complex and calculation expensive approach is ready to be used by the industry. However, if not, then the more computational heavy, fully coupled three dimensional model with aggregates in a suspending fluid may be inevitable when numerical predicting gravity induced aggregate migration in SCC.

Optimization:

- Both the feasibility and case study showed that the best solutions found by the optimization algorithm was non-trivial casting scenarios, even though the design variables involved in the optimization process were limited. This fact clearly stated that the coupling between a numerical model capable of predicting gravity induced aggregate migration and an optimization algorithm can be a useful tool. However, one constraint for this being a tool used in the industry in the future is the dependency on an applicable relationship between the α parameter and the rheological parameters of SCC. In the case where this is not possible and the fully coupled three dimensional model with aggregates in a suspending fluid is needed to predict the gravity induced aggregate migration, the coupling to an optimization algorithm is most likely not relevant, since the calculation time of such model is too time consuming (at present). Finally, the study showed that the calculation time was 1 hour for a 0.3x3m beam, however if for instance a large vertical casting was evaluated instead, which is where SCC has an edge as compared to conventional concrete, then the calculation most likely would be too time consuming to finish the optimization study in a reasonable time. Two future implementations which may solve this problem by speeding up the calculation are i) to split the pressure and velocity calculation like the algorithm used in FLOW-3D or ii) reprogramming the CFD solver in C or Fortran.

Bibliography

- Barkhudarov, M. R. (2004). Lagrangian vof advection method for flow-3d. Technical report, Flow Science, Inc.
- Batchelor, G. K. (1967). *An introduction to fluid dynamics*. Cambridge University Press, Cambridge.
- Billberg, P. (2003). Form pressure generated by self-compacting concrete. In *3rd int RILEM symp Self-Compacting Concrete*.
- Bingham, H. B., Larsen, P. S., and Barker, V. A. (2009). *Computational Fluid Dynamics - Lecture Note for Course no. 41319*. Technical University of Denmark.
- Bird, R. B., Armstrong, R. C., and Hassager, O. (1987). *Dynamics of polymeric liquids - Volume 1, Fluid dynamics*. John Wiley & Sons.
- Chateau, X., Ovarlez, G., and Trung, K. L. (2008). Homogenization approach to the behavior of suspensions of noncolloidal particles in yield stress fluids. *Journal of Rheology*, 52:489–506.
- de Larrard, F. (1999). Concrete mixture proportioning: a scientific approach. *Modern Concrete technology*, 9.
- de Larrard, F. and Le Roy, R. (1992). Correlations between mix design and some mechanical properties of high performance concretes. *RILEM Materials and Structures*, 25:464–475.
- Deb, K. (2001). *Multi-Objective Optimization using Evolutionary Algorithms*. John Wiley and Sons, Ltd, Chichester, UK.
- Dufour, F. and Pijaudier-Cabot, G. (2005). Numerical modelling of concrete flow: homogeneous approach. *International Journal for Numerical and Analytical Methods in Geomechanics*, 29(4):395–416.
- Eguchi, K. and Teranishi, K. (2005). Prediction equation of drying shrinkage of concrete based on composite model. *Cement and Concrete Research*, 35(3):483 – 493.
- en.wikipedia.org (2012).
- Ferraris, C. and Martys, N. (2003). Relating fresh concrete viscosity measurements from different rheometers. *Journal of Research of the National Institute of Standards and Technology*, 108(3):229 – 234.
- Geiker, M. (2008). *Development in the formulation and reinforcement of concrete*, chapter Self-compacting concrete (SCC). Woodhead Publishing.

- Goldberg, D. (1989). *Genetic Algorithms in Search, Optimization & Machine Learning*. Addison Wesley Longman, Inc.
- Gram, A. (2009). *Numerical modelling of Self-Compacting Concrete Flow*. PhD thesis, Royal Institute of Technology (KTH).
- Gram, A. and Silfwerbrand, J. (2011). Numerical simulation of fresh scc flow: applications. *Materials and Structures*, 44:805–813. 10.1617/s11527-010-9666-9.
- Hattel, J. H. (2005). *Fundamentals of Numerical Modelling of Casting Processes*. Polyteknisk Forlag.
- Hirt, C. and Nichols, B. (1981). Volume of fluid (vof) method for the dynamics of free boundaries. *Journal of Computational Physics*, 39(1):201 – 225.
- Houst, Y. F., Bowen, P., Perche, F., Kauppi, A., Borget, P., Galmiche, L., Meins, J.-F. L., Lafuma, F., Flatt, R. J., Schober, I., Banfill, P. F., Swift, D. S., Myrvold, B. O., Petersen, B. G., and Reknes, K. (2008). Design and function of novel superplasticizers for more durable high performance concrete (superplast project). *Cement and Concrete Research*, 38(10):1197 – 1209.
- Kalland, K. M. (2008). A navier-stokes solver for single and two-phase flow. Master’s thesis, University of Oslo.
- Kotas, P., Tutum, C., Snajdrova, O., Thorborg, J., and Hattel, J. (2010). A casting yield optimization case study: Forging ram. *International Journal of Metal Casting*, 4:61–76.
- Krieger, I. and Dougherty, T. (1959). A mechanism for non-newtonian flow in suspensions of rigid spheres. *Transactions of the society of rheology*, 3:137–152.
- Mahaut, F., Mokéddem, S., Chateau, X., Roussel, N., and Ovarlez, G. (2008). Effect of coarse particle volume fraction on the yield stress and thixotropy of cementitious materials. *Cement and Concrete Research*, 38(11):1276 – 1285.
- Martys, N. and Ferraris, C. (2002). Simulation of scc flow. In *First North American Conference on the Design and Use of Self-Consolidating Concrete. Proceedings. Chicago, IL, November 12-13, pp. 27-30*.
- Mori, H. and Tanigawa, Y. (1992). Simulation methods for fluidity of fresh concrete. *Memoirs of the School of Engineering, Nagoya University*, 44(1):71–134.
- Neville, A. (1995). *Properties of Concrete*. Pearson.
- Nguyen, T., Roussel, N., and Coussot, P. (2006). Correlation between l-box test and rheological parameters of a homogeneous yield stress fluid. *Cement and Concrete Research*, 36(10):1789–1796.
- Noor, M. and Uomoto, T. (1999). Three dimensional discrete element simulation of rheological test of self-compacting concrete. In *Self-Compacting Concrete: Proceedings of the First International RILEM Symposium*.
- Okamura, H. and Ouchi, M. (2003). Self compacting concrete. *Journal of Advanced Concrete Technology*, 1:5–15.

- Patankar, S. V. (1980). *Numerical heat transfer and fluid flow*. Hemisphere Publishing Corporation.
- Pilliod, J. (1992). An analysis of piecewise linear interface reconstruction algorithms for volume-of-fluid methods. Master's thesis, University of California, Davis.
- Pilliod Jr., J. E. and Puckett, E. G. (2004). Second-order accurate volume-of-fluid algorithms for tracking material interfaces. *Journal of Computational Physics*, 199(2):465 – 502.
- rilem.net (2012).
- Roussel, N. (2006a). Correlation between yield stress and slump: Comparison between numerical simulations and concrete rheometers results. *Materials and Structures*, 39:501–509. 10.1617/s11527-005-9035-2.
- Roussel, N. (2006b). A theoretical frame to study stability of fresh concrete. *Materials and Structures*, 39:81–91. 10.1617/s11527-005-9036-1.
- Roussel, N. (2006c). A thixotropy model for fresh fluid concretes: Theory, validation and applications. *Cement and Concrete Research*, 36(10):1797 – 1806.
- Roussel, N. (2007). The lcpc box: A cheap and simple technique for yield stress measurements of scc. *Materials and Structures/Materiaux et Constructions*, 40(9):889–896.
- Roussel, N. and Coussot, P. (2005). "fifty-cent rheometer" for yield stress measurements: from slump to spreading flow. *Journal of Rheology*.
- Roussel, N., Geiker, M. R., Dufour, F., Thrane, L. N., and Szabo, P. (2007a). Computational modeling of concrete flow: General overview. *Cement and Concrete Research*, 37(9):1298 – 1307.
- Roussel, N., Staquet, S., Schwarzenruber, L., Le Roy, R., and Toutlemonde, F. (2007b). Scc casting prediction for the realization of prototype vhhpc-precambered composite beams. *Materials and Structures*, 40:877–887.
- Shen, L., Struble, L., and Lange, D. (2009). Modeling static segregation of self-consolidating concrete. *ACI Materials Journal*, 106(4):367–374.
- Simonsson, P. (2011). *Buildability of Concrete Structures*. PhD thesis, Luleå University of Technology.
- Skocek, J., Svec, O., Spangenberg, J., Stang, H., M.R., G., Roussel, N., and Hattel, J. (2011). Modeling of flow of particles in non-newtonian fluid using lattice boltzmann method. In *Proceedings of the 8th International Congress on the Chemistry of Cement*.
- Spangenberg, J., Roussel, N., Hattel, J., Sarmiento, E., Zirgulis, G., and Geiker, M. (2012a). Patterns of gravity induced aggregate migration during casting of fluid concretes. *Cement and Concrete Research*, page Accepted.
- Spangenberg, J., Roussel, N., Hattel, J., Stang, H., Skocek, J., and Geiker, M. (2012b). Flow induced particle migration in fresh concrete: Theoretical frame, numerical simulations and experimental results on model fluids. *Cement and Concrete Research*, 42(4):633 – 641.

- Spangenberg, J., Roussel, N., Hattel, J. H., Thorborg, J., Geiker, M. R., Stang, H., and Skocek, J. (2010). Prediction of the impact of flow-induced inhomogeneities in self-compacting concrete (scc). In Khayat, K. H. and Feys, D., editors, *Design, Production and Placement of Self-Consolidating Concrete*, volume 1 of *RILEM State of the Art Reports*, pages 209–215. Springer Netherlands.
- Spangenberg, J., Tutum, C., Hattel, J., Roussel, N., and Geiker, M. (2011). Optimization of casting process parameters for homogeneous aggregate distribution in self-compacting concrete: A feasibility study. In *Evolutionary Computation (CEC), 2011 IEEE Congress on*, pages 2163 –2169.
- Spangenberg, S. (2010). *Large construction projects and injury prevention*. Doctoral dissertation (Dr. Techn). National Research Centre for the Working Environment, Denmark & University of Aalborg, Denmark. 92 pp & 17 articles.
- Thrane, L. N. (2007). *Form Filling with Self-Compacting Concrete*. PhD thesis, Technical University of Denmark (DTU).
- Vasilic, K., Meng, B., Kühne, H., and Roussel, N. (2011). Flow of fresh concrete through steel bars: A porous medium analogy. *Cement and Concrete Research*, 41(5):496 – 503.
- voscc.net (2012).
- www.flow3d.com (2010). *V9.4 FLOW-3D User Manual*.
- Yao, G. F. (2004). Development of new pressure-velocity solvers in flow-3d. Technical report, Flow Science, Inc.

Appendixes

A PAPER-I

J. Spangenberg, N. Roussel, J. H. Hattel, J. Thorborg, M. R. Geiker, H. Stang, and J. Skocek (2010). Prediction of the impact of flow-induced inhomogeneities in Self-Compacting Concrete (SCC). In K. H. Khayat and D. Feys (Eds.), *Design, Production and Placement of Self-Consolidating Concrete*, Volume 1 of *RILEM State of the Art Reports*, pp. 209-215. Springer Netherlands.

Prediction of the impact of flow induced inhomogeneities in Self Compacting Concrete (SCC)

J. Spangenberg¹, N. Roussel², J. H. Hattel¹, J. Thorborg^{3,1}, M. R. Geiker⁴, H. Stang⁴, J. Skocek⁴

¹ Department of Mechanical Engineering, Technical University of Denmark (DTU), Denmark

² Université Paris Est, Laboratoire Central des Ponts et Chaussées (LCPC), France

³ MAGMA GmbH, Germany

⁴ Department of Civil Engineering, Technical University of Denmark (DTU), Denmark

Abstract. SCC is nowadays a worldwide used construction material. However, heterogeneities induced by casting may lead to variations of local properties and hence to a potential decrease of the structure's load carrying capacity. The heterogeneities in SCC are primarily caused by static and dynamic segregation. The present paper reports property maps for a beam based on particle distributions at the end of casting derived from numerical flow simulations. A finite volume based numerical model is used to predict particle distributions at the end of casting, which are then converted into property maps using semi-empirical relations from literature.

Introduction

The ideal mix design of a SCC is located somewhere between two opposite objectives. On one hand, the SCC has to be as fluid as possible to ensure that it will fill the formwork under its own weight. On the other hand, it has to be a stable mixture as flow in such a confined zone as a reinforced formwork may cause the components of the material to separate during casting. Therefore, a compromise between fluidity and stability has to be reached. The available method in the traditional toolbox of the civil engineer is to try various mix designs and, for each of them, cast the real size element and choose the most suitable mixture (if there is one). This is expensive, time consuming and does not guarantee that an answer will be obtained. However, in the last twenty years, the numerical tools of non-

Newtonian fluid dynamics have allowed for the numerical simulations of casting processes and, for a very low cost in time and money, the identification of the minimum needed fluidity [1]. Mori and Tanigawa [2] first demonstrated the applicability of Viscoplastic Divided Element Method (VDEM) to simulate the flow of concrete in a reinforced beam section and the filling of a reinforced wall whereas Kitaoji *et al.* [3] confirmed the applicability of 2D VDEM to simulate the flow of fresh concrete cast into a formwork. The results of a form filling experiment in a vertical wall have also been compared with the corresponding 3D simulation [4]. The results show good correlation with respect to detection of the free surface location, dead zones and particle paths. Numerical simulations were recently also applied to an industrial casting of a very high strength concrete pre-cambered composite beam by Roussel *et al.* [5]. The results of the simulations carried out for various values of the rheological parameters helped to determine the value of the minimum fluidity needed to cast the element. In most applications, a satisfactory agreement was found between the predicted and the actual global flow of the material within the formwork. It can therefore be expected that, in the future, computational modeling of flow will become a practical tool allowing for the simulation of either total form filling as described above or detailed flow behavior such as particle migration or fiber orientation. These methods could then be gathered in order to create a casting process engineering toolbox and bring rheology from the laboratory to the field.

The present paper shows a glimpse at this future by illustrating how it is possible to extract a map of properties in the hardened state of a structural element from numerical simulations of casting processes coupled with numerical simulations of the segregation of the coarsest particles. In the first part of this paper, we describe the numerical techniques and assumptions needed to simulate the segregation phenomenon during casting of SCC. In the second part, we present maps of coarse aggregates distribution through and at the end of the casting process. Finally, using simple semi-empirical correlations from literature, we deduct from these results maps of local properties or local phenomena such as elastic modulus, compressive strength and drying shrinkage.

Numerical simulations description

Most numerical simulations of concrete flows in literature consist in either considering a homogeneous fluid implicitly containing particles or taking explicitly into account the presence of the particles using for example Discrete Element Methods (DEM). The homogeneous approach is easier to implement but is valid only when the smallest characteristic dimension of the flow (size of the mould or spacing between bars) is high compared to the size of the largest particles (five times larger for example in [6]). In this paper, we will assume that these conditions are fulfilled and use a homogeneous approach to calculate the velocity field. As accepted in literature, a Bingham model is, in this case, an acceptable rheological

model to describe the concrete rheological behavior. From this velocity field, we then calculate the trajectories of the particles. Meaning, a one-way momentum coupling is applied such that the fluid affects the particles but not vice versa.

The computational fluid dynamics (CFD) code Flow3D® [7] is used here to solve the Navier Stokes equations. FLOW3D® is a general-purpose computer program with many capabilities. Using input data, the user can select different physical options to represent a wide variety of fluid flow phenomena. The program can be operated in several modes corresponding to different limiting cases of the general Navier Stokes equations. More details about the numerical methods used to model flow of concrete with FLOW3D® can be found in [8]. We consider in this paper an SCC with a yield stress of 50 Pa and a plastic viscosity of 50 Pa s. These are common orders of magnitude for standard SCC in housing construction that may be prone to segregation during casting. We moreover consider in this paper that concrete can be considered by a two phases approach as rigid particles suspended in a continuous phase. The suspended particles considered here correspond to the 25% coarsest particles in the material. The volume fraction of these particles is assumed to be in the order of 15-20% in practice and can be associated to a characteristics average diameter of 15mm. By doing so, we assume that the 75% finest aggregate particles are sufficiently small to be stable and do not segregate during flow. We moreover assume that the viscosity of the continuous phase is 10 times lower than the viscosity of the SCC. This is in agreement with the orders of magnitudes of viscosities of standard materials from the construction field (cement paste 0.5-1Pa., mortar 5-10Pa.s and concrete 50-100Pa.s). In the following, we either assume that a) the particles have the same density as the suspending fluid (2200kg/m^3) when we show results for which no segregation occurs or b) have a density of 2700kg/m^3 when we focus on segregation during casting. It has to be noted that, in the following simulations, all interactions between particles are neglected and that the rheological parameters of the concrete do not vary due to local volume fraction changes. The only thing that is simulated is gravity and the hydrodynamic effects of the fluid on the moving particle. We simulate the casting of a 3m long and 30cm thick beam. The casting point is located at the center of the beam and the material is assumed to be homogenous at the entry point. We neglect the presence of any steel bars and perform the calculation in 2D, and therefore also neglecting the influence of the lateral walls. We impose the casting rate so that the front velocity is of the order of 30cm/s.

Particle distributions

The casting process simulations are illustrated in Fig. 1 at successive time steps. Through the casting, the density difference between the coarse particle and the continuous phase is at the origin governed by a slow migration of the particles towards the bottom of the formwork. This migration is slowed down by the viscosity of the continuous phase but is not fully prevented. In the case of the SCC

studied here the results are within the frame of our assumptions.

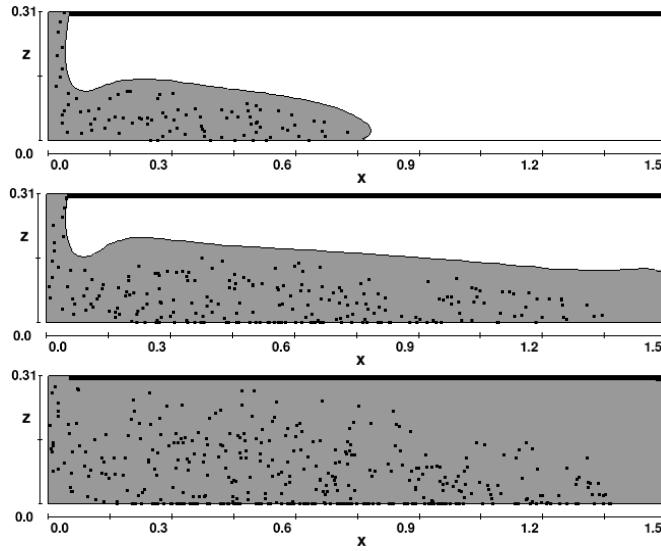


Figure 1. Particle distribution through the casting process. Only the right half of the beam is shown. Vertical and horizontal distances are in (m).

It can be noted that there exist zones at the bottom of the formwork where the volume fraction of the coarse aggregates is predicted to be higher than the maximum volume fraction at the end of casting. This source of error is due to the fact that we do not take into account any interactions between particles and between particles and walls. The particles therefore accumulate without any hindrances at the bottom wall.

In Fig. 2 we plot the total aggregates (sand and gravel) volume fraction at the end of casting. In order to obtain this value, we add the local volume fraction of the coarsest particles to the volume fraction of the stable finer aggregates. The top figure in Fig. 2 represents the case of particles having the same density as the continuous phase. While a homogeneous distribution of the particles is expected in this case at the end of casting, we see in this figure some heterogeneities. These are due to the sampling and particles counting method and to the random generation of particles at the flow inlet. These “natural” heterogeneities are of the order of ± 0.03 (5%) compared to the homogeneous concrete with an aggregate volume fraction of 0.64. The bottom figure in Fig. 2 shows the heterogeneities in the beam at the end of casting in the case of particles with a density of 2700kg/m^3 in a continuous phase with a density of 2200kg/m^3 . In this case, these heterogeneities are of the order of ± 0.20 (25%). These are five times higher than the heterogeneities associated with the counting and sampling technique. Because of the stacking of

the coarsest particles at the bottom of the formwork described above, there exist zones at the bottom of the formwork where the total aggregates volume fraction is predicted to be higher than the maximum volume packing fraction at the end of casting. In the zones where this happens, we consider in Fig. 2 and in the following sections that the volume fraction of the particles in these zones is equal to the maximum packing fraction of the order of 0.8.

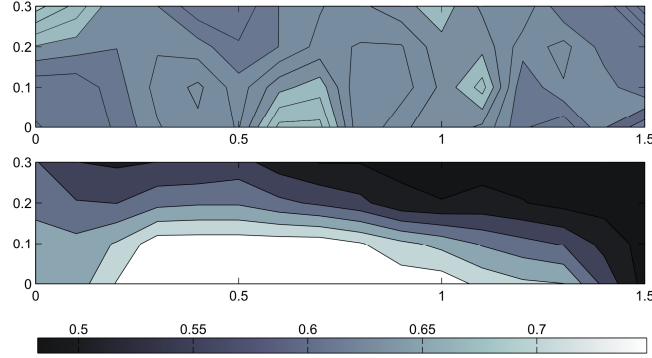


Figure 2. Aggregate volume fraction map. (top) “homogeneous” distribution of particles (homogeneous aggregate volume fraction is 0.64) (bottom) segregated particles. Vertical and horizontal distances are in (m).

Property maps

In Fig. 3 and Fig. 4 we plot the maps of the relative elastic modulus (*i.e.* the ratio between the local elastic modulus and the elastic modulus of the homogenous reference concrete) and the relative compression strength (*i.e.* the ratio between the local compressive strength and the compressive strength of the homogenous reference concrete) extracted from the bottom figure in Fig. 2 using the simple models proposed in [9] and [10]. The variations induced by segregation are of the order of 10% for these two properties.

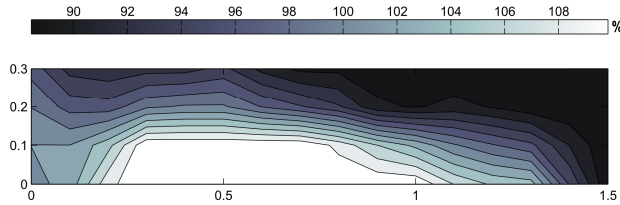


Figure 3. Relative elastic modulus map. Vertical and horizontal distances are in (m).

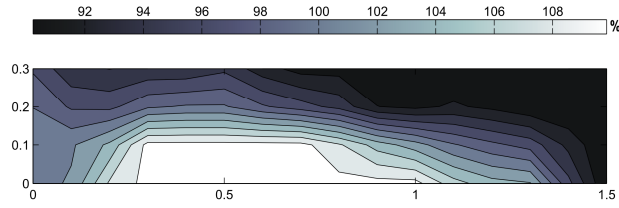


Figure 4. Relative compressive strength map. Vertical and horizontal distances are in (m).

In Fig. 5 we plot the map of the relative drying shrinkage strain (*i.e.* the ratio between the local drying shrinkage strain and the drying shrinkage strain of the homogenous reference concrete) using the relation given in [11]. The variations are of the order of 25% and could induce a strong concentration of shrinkage in specific zones of the beam, which could in turn induce some cracking.

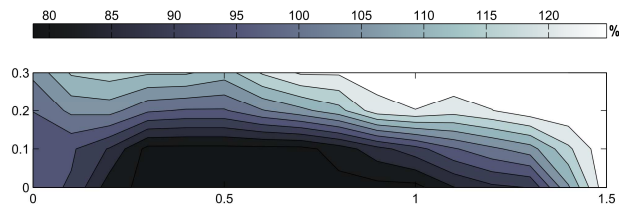


Figure 5. Relative drying shrinkage strain map. Vertical and horizontal distances are in (m).

Conclusion

We have shown in this paper how it is possible to use a CFD calculation of the casting process coupled with numerical modeling of the segregation of the coarsest particles to produce a map of properties in the hardened state of a structural element. We have plotted maps of local properties and phenomena such as elastic modulus, compressive strength and drying shrinkage strain for a beam filled with SCC, using simple semi-empirical correlations from literature.

References

- [1] Roussel, N. Geiker, M.R. Dufour, F. Thrane, L.N. Szabo, P. (2007), *Computational modeling of concrete flow: general overview*, Cement and Concrete Research, vol. 37(9), p. 1298-1307.

- [2] Mori, H. and Tanigawa, Y. (1992), *Simulation methods for fluidity of fresh concrete*, Memoirs of the school of engineering, Nagoya University, vol. 44, p. 71-133.
- [3] Kitaoji, H. Tanigawa, Y. Mori, H. Kurokawa, Y. Urano S. (1996), *Flow simulation of fresh concrete cast into wall structure by viscoplastic divided space element method*, Trans. of the Japan concrete institute, vol. 16, p. 45-52.
- [4] Thrane, L.N. Szabo, P. Geiker, M.R. Glavind, M. Stang, H. (2005), *Simulation and verification of flow in SCC test methods*, Proc. of 4th int. RILEM Symp. on SCC.
- [5] Roussel, N. Staquet, L. D'Aloia Schwarzenruber, L. Le Roy, R. Toutlemonde, F. (2007), *SCC casting prediction for the realization of prototype VHPC-precambered composite beams*, Materials and Structures, vol. 40(9), p. 877-887.
- [6] Coussot, P. and Ancey (1999), *Rheophysics of pastes and suspensions*, EDP Sciences, [in French].
- [7] Flow3D version 8.1 (2004), User's manual 1.
- [8] Roussel, N. and Coussot, P. (2005), *"Fifty-cent rheometer" for yield stress measurements: from slump to spreading flow*, Journal of Rheology, vol. 49(3), p. 705-718.
- [9] de Larrard, F. and Le Roy, R. (1992), *Correlations between mix design and some mechanical properties of high performance concretes*, RILEM Materials and Structures, vol. 25, p. 464-475, [in French].
- [10] de Larrard, F. (1999), *Concrete mixture proportioning – a scientific approach*, Modern Concrete technology, series 9.
- [11] Eguchi, K. and Teranishi, K. (2005), *Prediction equation of drying shrinkage of concrete based on composite model*, Cement and Concrete Research, vol. 35, p. 483-493.

B PAPER-II

J. Spangenberg, N. Roussel, J. Hattel, H. Stang, J. Skocek, and M. Geiker (2012). Flow induced particle migration in fresh concrete: Theoretical frame, numerical simulations and experimental results on model fluids. *Cement and Concrete Research* 42 (4), 633-641.



Flow induced particle migration in fresh concrete: Theoretical frame, numerical simulations and experimental results on model fluids

J. Spangenberg ^a, N. Roussel ^{b,*}, J.H. Hattel ^a, H. Stang ^c, J. Skocek ^c, M.R. Geiker ^{c,d}

^a Department of Mechanical Engineering, Technical University of Denmark (DTU), Denmark

^b Université Paris Est, Laboratoire Central des Ponts et Chaussées (LCPC), France

^c Department of Civil Engineering, Technical University of Denmark (DTU), Denmark

^d Department of Structural Engineering, Norwegian University of Science and Technology, Norway

ARTICLE INFO

Article history:

Received 15 November 2011

Accepted 31 January 2012

Keywords:

Fresh concrete (A)

Rheology (A)

Aggregate (D)

Modelling (E)

Segregation

ABSTRACT

In this paper, we describe and compare the various physical phenomena which potentially lead to flow induced particle migration in concrete. We show that, in the case of industrial casting of concrete, gravity induced particle migration dominates all other potential sources of heterogeneities induced by flow. We then show, from comparisons between experiments using model materials, dimensional analysis and numerical simulations, that, from a quantitative point of view, the viscous drag force, which prevents particles from migrating during a casting process, shall neither be computed from the apparent viscosity nor from the plastic viscosity of the suspending phase but from its tangential viscosity. Finally, the transfer of this type of numerical prediction tool to real concrete is discussed.

© 2012 Elsevier Ltd. All rights reserved.

1. Introduction

At the scale of a structural element such as a beam or a slab, concrete is a heterogeneous material. This is even more so the case if constitutive aggregates get segregated during the flow induced by casting processes or if they settle when concrete is at rest before setting.

In the traditional industrial description of self compacting concrete property requirements, the so-called “resistance to dynamic segregation” is often distinguished from the “resistance to static segregation”. The first one is associated with flow induced particle migration originating from various phenomena whereas the second one is only associated with the aggregate settling process due to the density difference between the components when the material is at rest before or after casting.

Static segregation has been the topic of several papers [1–4]. These papers either deal with the measurement or the prediction of this phenomenon. They show that yield stress and thixotropy seem to dictate static segregation for a given granular skeleton.

Dynamic segregation (i.e. flow induced particle migration) has however been far less studied. Depending on the considered concrete flow, different phenomena can dominate and dictate particle migration within the material.

In this paper, we first describe and compare the various physical phenomena which potentially lead to flow induced particle migration.

We compare their influence on the local aggregates volume fraction to the geometrically induced particle heterogeneity due to wall effect. We show for instance that shear induced particle migration and wall effect dominate in pumping processes whereas, in the case of industrial casting of concrete, gravity induced heterogeneity dominates over all other potential sources of heterogeneities induced by flow.

In the second part, we compare experimental measurements of flow induced particle migration, dimensional analysis and numerical simulations. We conclude on the value of the viscosity that has to be considered when studying particle migration during a casting process.

Moreover, based on the aforementioned results, it is found that it is possible to numerically predict gravity induced particle migration in the case of the casting of a model material, designed to mimic self compacting concrete.

Finally, the transfer of this type of numerical prediction tool to real concrete is discussed.

2. Flow induced particle migration

In this section, the consequences of the physical phenomena at the origin of flow induced particle migration on local aggregates volume fraction are compared. Although we do not deal with detailed processing problems, we provide here general orders of magnitude. Three main types of flow induced particle migration are identified:

- Shear induced particle migration
- Gravity induced particle migration
- Granular blocking

* Corresponding author at: IFSTTAR, 158, Bd. Lefebvre, 75732 Paris Cedex 15, France. Tel. +33 140435285.

For each particle migration phenomenon, the maximum induced local particle volume fraction variation and the characteristic time of this migration are estimated. Then, in order to estimate the global effect at the scale of the concrete flow, we ponder the local volume fraction variation by the size of the zone where the particle migration is expected to occur. We moreover compare the consequences of the above phenomena with particle heterogeneity induced by the wall effect.

2.1. Flow description

In the types of flow considered here, the smallest dimension will be denoted the thickness H . The flows can be industrial casting processes (the thickness is then the smallest dimension of the element to be cast), pumping flows (the thickness is then the radius of the pipe) or flows within rheometers or acceptance tests such as slump or slump flow test. The characteristic flow time is denoted T_f . In the case of a transient flow, this could be, for instance, the duration of the flow from flow start to stop. In the case of a steady state flow such as pumping, it could be the time spent by the concrete in the pumping pipe. The flow characteristic length (i.e. the propagation length in transient flows or the largest flow dimension in steady state flows) is denoted L . In the case of casting, this could, for instance, correspond to the length or the half length of a beam depending on the casting process. In the case of pumping, this could correspond to the length of the pipe. In these flows, the material flows at an average velocity V and is subjected to an average shear rate $\dot{\gamma}$. The quantities $\dot{\gamma}$, V , L , H and T_f are linked through the following dimensional relations: $T_f = L/V$ and $\dot{\gamma} = V/H$.

2.2. Shear induced particle migration

Particle collisions in highly sheared and/or highly concentrated zones force particles to migrate from these zones. This effect is counterbalanced by the local increase in the suspension viscosity resulting from this migration. Shear induced particle migration finds therefore its origin in the competition between gradients in particle collision frequency and gradients in viscosity of the suspension.

Leighton and Acrivos [5] and Phillips et al. [6] modeled the complex diffusion process associated with shear induced particle migration. The diffusion coefficient D may be written as $D \approx \bar{D}(\phi) \dot{\gamma} a^2$ [7,8] where ϕ is the solid volume fraction, $\dot{\gamma}$ the shear rate, a the size of the particles and $\bar{D}(\phi)$ a dimensionless diffusion coefficient proportional to the power two of the volume fraction $\bar{D}(\phi) \propto \phi^2$ [9]. Note here the power two of the particle diameter appearing in the value of the diffusion coefficient showing that coarse particles are the most prone to shear induced migration.

Shear induced particle migration is often strongly localized in highly sheared zones at interfaces. It can therefore strongly affect flow by creating lubricating layers such as the ones observed during concrete pumping processes [10–13] or during rheometric testing on concrete or mortars [14]. Recent and detailed numerical simulations of shear induced particle migration were carried out in the case of pumping [15]. The results showed that shear induced particle migration is indeed inducing the slippage layer of several mm at the interface between the material and the pipe during pumping processes. In this zone, not only the coarsest particles are migrating but also sand grains.

Shear induced particle migration reaches equilibrium because of the increase in viscosity of the zones where particles are migrating to. It can then be expected that shear induced migration shall stop before the local particle volume fraction is high enough to reach the so-called random loose packing (i.e. the lowest volume fraction value allowing for a percolated network of contacts between particles). It was shown recently that this random loose packing can be estimated

from the value of the maximum packing fraction ϕ_m of the particles and is of the order of $0.8\phi_m$ [16–18].

As a consequence, it can be expected that the highest variation in particle volume fraction due to shear induced particle migration after an infinite time shall be lower than:

$$\Delta\phi^{shear} = \phi_0 \left(1 - \frac{\phi_0}{0.8\phi_m} \right) \quad (1)$$

where ϕ_0 is the mix design particle volume fraction.

Let us now consider the characteristic time associated to shear induced particle migration. Most experimental studies show that the particle volume fraction profile reaches a steady state after a certain critical deformation γ_c of the suspension [6,9,19–21]. Recent results [9] have however shown, using MRI measurements, that, in the case of concentrated suspensions, this critical deformation seems to be one order of magnitude lower than expected. This peculiar effect was attributed to a local shear thickening of the material, which enhances particle migration [9]. It can be estimated from the above studies that the critical deformation, above which steady state is reached, in the case of concrete or mortars shall be of the order of $\gamma_c \approx H^2/10a^2\phi^2$. Shear induced particle migration shall therefore reach its full extent after a characteristic shear induced particle migration time T_c^{shear} of the order of:

$$T_c^{shear} = \frac{H^2}{10a^2\phi^2\dot{\gamma}} \quad (2)$$

2.3. Gravity induced particle migration

We will only deal here with the case of materials which are stable at rest [1,2] and focus on the particle migration induced by gravity when concrete is flowing and/or being cast [22]. It can however be reminded here that, in order to produce a concrete, which stays homogeneous at rest, the constitutive cement paste or mortar must either have a sufficient yield stress [1,2,23] or sufficient thixotropic structuration rate to quickly build up a structure able to support the coarsest particles [24,25].

When the material flows, the stress generated by gravity in the mixture is higher than the yield stress of the material. This means that any additional stress, such as the one generated by a density difference between an aggregate and the surrounding mixture, could induce a local flow around the aggregate even if this additional stress itself is lower than the yield stress.

Gravity induced particle migration during casting results therefore from the competition between the difference in density of the mixture components that force them to separate and the viscous drag of the flowing suspending fluid that slows down the phenomenon. Contrarily to shear induced particle migration, it is not a diffusion process but an advection process. The force induced by the density difference can be written as $F_{gravity} = g\Delta\rho\pi a^3/6$, where $\Delta\rho$ is the density difference between the aggregates and the suspending phase. Viscous drag can be computed, as a first approximation, from Stoke's law for dilute spheres in Newtonian fluids, $F_{viscous} = 3\pi\mu_0 a V_s$, where μ_0 is the viscosity of the suspending phase and V_s is the relative settling velocity of the aggregate in the suspending fluid. This relative velocity, in the case of aggregates heavier than the suspending fluid is a vertical settling velocity and can be written as $V_s = g\Delta\rho a^2/18\mu_0$. This approach neglects any effect of the yield stress of the surrounding fluid. It also neglects any other non Newtonian features. This aspect will however be discussed further in this paper.

As in the previous section, it can be expected that gravity induced particle migration shall stop before the local particle volume fraction reaches the so-called random loose packing. As a consequence, the highest variation in particle volume fraction due to gravity induced

particle migration is the same as the one due to shear induced particle migration:

$$\Delta\phi^{gravity} = \Delta\phi^{shear} = \phi_0 \left(1 - \frac{\phi_0}{0.8\phi_m} \right) \quad (3)$$

The characteristic time associated to this process is however very different. Being an advection process, it can be estimated as:

$$T_c^{gravity} \approx \frac{H}{V_s} = \frac{18\mu_0 H}{g\Delta\rho a^2}. \quad (4)$$

It is worth noting that the coarsest aggregates are once again most prone to a fast migration because of the power two of the particle diameter appearing in Eq. (4).

2.4. Granular blocking induced heterogeneities

We will not deal much here with this type of flow induced heterogeneity as we assume that, in proper industrial castings with properly mix designed materials, the size of the coarsest particles is compatible with the gap between reinforcement bars within the element to be cast [26–30] or with the thickness of the flow.

It should also be kept in mind here that the granular blocking phenomenon is of a probabilistic nature. The probability of granular blocking increases with the number of particles crossing the obstacles, their volume fraction and the ratio between the diameter of the particles and the gap between the obstacles. As long as it is not coupled with another source of flow induced particle migration, which could increase the local particle volume fraction at the vicinity of the obstacles, this phenomenon seems to only depend on geometrical considerations and not depend on the rheology of the suspending fluid.

Finally, it shall be kept in mind that this type of particle migration shall dominate all others when they occur as they are able to concentrate particle up to and above the loose packing fraction in the vicinity of the obstacles. They may also prevent the proper filling of the formwork [31–33].

2.5. Heterogeneity in particle distribution induced by the wall effect

Variations in local particle volume fraction may also be induced by the presence of walls. This phenomenon is not induced by flow but, because of simple geometrical considerations, it is not possible to find the center of a particle of diameter a at a distance from a wall lower than $a/2$ [34]. Because of this wall effect, there exists therefore some heterogeneity at the vicinity of any solid interface within the flow.

Thus, in a plane parallel to the wall, the coarse particle volume fraction will be the sum of contributions from all coarse particles with centers within $a/2$ of the plane. If the plane is at a short distance δ from the wall compared to the size of the particles, the particle volume fraction at the plane is small since there are relatively few particles with centers within a distance $a/2$ of the plane (only those with centers between $a/2$ and $a/2 + \delta$ can contribute). As the plane is moved further from the wall, more and more particles can contribute to the coarse particle volume fraction. The coarse particle volume fraction therefore increases from the wall. At a distance a , none of the suspension within $a/2$ of the considered plane is devoid of coarse particle centers. The coarse particle volume fraction reaches then its bulk value. The coarse particle volume fraction increases therefore from zero at the wall to the bulk volume fraction at a distance a . Its average value in the depleted zone can be estimated as half the bulk volume fraction $\phi_0/2$.

This phenomenon however only concerns interface zones, the characteristic thickness of which is, as shown above, of the order of

a and therefore smaller than the characteristic size of the concrete element to be cast. At the scale of the concrete flow of thickness H , the variation in coarse particle volume fraction due to wall effect shall therefore only be of the order:

$$\Delta\phi^{walleffect} \approx \frac{\phi_0 a}{2H}. \quad (5)$$

2.6. Induced heterogeneities during concrete casting or testing

As it was shown in the previous sections, most particle volume fraction variations induced by flow are increasing functions of the diameter of the particles and are therefore stronger at the scale of the coarsest aggregates. We choose here to focus on this fraction of the granular skeleton. As concrete contains in average 60 to 80% aggregates and as at least half of them by volume are coarse aggregates, we will therefore focus in the following on particles with a diameter of the order of 1 cm and a mix design volume fraction of approximately 40%.

We consider here the case (i) of the slump test for conventional concretes, (ii) of the slump flow test for self compacting concretes, (iii) of a typical concrete rheometer test and (iv) of typical casting and pumping processes. The quantities ϕ_0 , a and $\Delta\rho$ are respectively considered as being around 40%, 0.01 m and 500 kg/m³. The considered values for T , H , L and V are gathered in Table 1.

The typical value of the viscosity of the so-called suspending fluid is far more delicate to identify. The orders of magnitude of viscosities of cementitious suspensions at typical industrial shear rates are 0.1–1 Pa s for cement pastes, 1–10 Pa s for mortars and 10–100 Pa s for concretes [18,35]. If we consider that the suspending phase for the coarsest aggregates shall locate somewhere between the mortar scale and the concrete scale itself, we can consider $\mu_0 = 10$ Pa s as an order of magnitude.

In Table 2, the expected variations in coarse aggregates volume fraction are computed by considering that the fastest phenomenon (i.e. the one with the shortest characteristic time) occurs first. Its magnitude is proportional (and also limited) to the maximum particle volume concentration variation induced by this phenomenon and also proportional to the ratio between the duration of the flow and the characteristic time of the phenomenon. In the case of heterogeneities induced by the wall effect, we, of course, consider that it is instantaneous and occurs prior to other induced particle migration.

It can be concluded from Table 2 that, although shear induced particle migration and wall effect dominate during pumping processes, gravity induced particle migration dominates during typical industrial concrete casting processes.

The results in Table 2 moreover show that, although slump in the case of conventional concrete is only weakly affected by flow induced particle migration, slump flow for self compacting concrete is affected by both a potential gravity induced particle migration and wall effects. Because of these effects, there is no generally applicable correlation (i.e. independent of the concrete tested) between the slump flow value and yield stress as shown in [36].

Finally, the results in Table 2 show that shear induced and gravity induced particle migration shall affect the results obtained with

Table 1

Parameters describing typical concrete flows and the model casting studied in this paper.

Flow	L (m)	T_f (s)	H (m)	V (m/s)
Slump	0.2	2	0.15	0.1
Slump flow	0.4	4	0.05	0.1
Rheometer	–	60	0.1	0.5
Casting	5	50	0.2	0.1
Pumping	100	100	0.05	1
Model casting	0.6	90	0.055	0.007

Table 2
Origins and magnitude of average particles volume fraction variations due to flow induced particles migration in typical concrete flows and in the model casting studied in this paper.

Flow	Shear induced heterogeneities	Gravity induced heterogeneities	Wall effect induced heterogeneities
Slump	Neglectable	Neglectable	1–2%
Slump flow	Of the order of 1%	Of the order of 1%	3–5%
Rheometer	3–5%	1–2%	1–2%
Casting	Neglectable	5–10%	Of the order of 1%
Pumping	3–5%	Neglectable	3–5%
Model casting (beads diameter = 2 mm)	Neglectable	1%	Neglectable
Model casting (beads diameter = 5 mm)	Neglectable	5%	Neglectable
Model casting (beads diameter = 7 mm)	Neglectable	7%	Of the order of 1%

concrete rheometers. These phenomena, which depend on the exact geometry of the rheometer, may be at the origin of the discrepancy between the available concrete rheometers [37,38] as shown by recent MRI measurements on model mortars [14].

3. Experimental measurements

We have shown, in the previous section, that gravity induced particle migration dominates during typical industrial concrete casting processes. In order to reproduce this phenomenon in the laboratory, a combination of a model material and a model formwork able to mimic the casting of self compacting concrete is developed in this section.

3.1. Materials

We prepare our model concrete with a polymer gel and glass beads at a volume fraction of 10%, which aims at mimicking the behavior of a fluid (but transparent) concrete [39].

The polymer used in this work is Carbopol Ultrez (manufacturer Noveon), a transparent material that disperses faster than other conventional grades. Carbopol is used here at a volume fraction of 0.3%.

The dehydrated Carbopol powder is first slowly added to distilled water through a fine metal mesh using a variable speed mixer. The solution is then neutralized by a sodium hydroxide solution at 18%. A mixing period of 6 h follows this neutralization phase. Finally, the products are conserved at 25 °C for 2 days. The prepared carbopol suspension can then be diluted in distilled water in order to produce mixtures with yield stresses between 15 and 125 Pa. Before use, air bubbles are removed by a slow manual shearing. Because of the low polymer concentration, the density of the carbopol gel is very close to the density of water.

The Carbopol suspension used in this study is not thixotropic as shown by the superposition of measurements obtained for increasing and decreasing shear rate ramps in Fig. 1. We use a HAAKE ViscoTester VT550 equipped with coaxial cylinders, the inner cylinder of diameter 18.9 mm being in rotation whereas the outer cylinder of diameter 20.5 mm remains fixed. Both surfaces of the cylinders are covered with sand paper in order to avoid wall slip. The modified gap width is identified using a reference Newtonian oil. The behavior of the carbopol gel can either be fitted with a Bingham model ($\tau = \tau_0 + \mu_p \dot{\gamma}$) mixture with a yield stress τ_0 of 40 Pa and a plastic viscosity μ_p of 1 Pa s or fitted with a Herschel Bulkley model ($\tau = \tau_0 + K \dot{\gamma}^n$) with a yield stress τ_0 of 40 Pa, $K = 15.8$ Pa s and $n = 0.48$.

The Bingham model parameters for the carbopol alone are used further in this work for the prediction of the global flow of the glass beads and carbopol mixture in the model formwork. Because of the low volume fraction of the glass beads, the behavior of the glass beads and carbopol mixture does not strongly differ from the rheological behavior of the carbopol alone. It can indeed be expected from the theoretical work of Chateau et al. [40,41] that the yield stress of the mixture shall be around 1.09 times the yield stress of the

carbopol whereas its plastic viscosity shall be around 1.3 times the plastic viscosity of the carbopol. Because of these low fluctuations of the rheological parameters with the local concentration of glass beads, the influence of flow induced heterogeneities on local rheological properties and on the global flow of the mixture will be neglected in the following.

Both Bingham and Herschel Bulkley model parameters will be alternatively used to model the gravity induced particle migration in the last part of this paper. Results obtained with the two models will be compared and discussed.

The glass beads used here are SiLibeads® (Type M, Sigmund Linder GmbH). Three diameters are used (2, 5 and 7 mm). The density of the glass beads is 2500 kg/m³. In order to ensure that these particles behave as rough aggregates, they were first roughened by abrasion and then cleaned by ultrasound in water (Cf. Fig. 2). To prepare the mixtures, the glass beads are slowly added to the carbopol gel and gently stirred manually until a homogenous material is obtained (Cf. Fig. 3).

3.2. Model formwork

The experimental setup used in this study is shown in Fig. 4 [39]. The setup consists of a 20 × 20 × 60 cm container made of transparent Plexiglas, enabling observation of the flow front of the poured fluid. Approximately 6 l of the carbopol containing a 10% volume fraction of glass beads are slowly poured at one side of the form. The pouring speed is roughly 0.1 l/s to avoid any inertia effect [33,42]. We checked that final shape did not depend on pouring rate in this range and we kept the pouring height constant for each test. When the flow stops, image analysis allows for the recording of the final shape of the material. The material is then divided into 6 zones by insertion of metal plates (Cf. Fig. 5). The content of each zone is washed and the volume fraction of glass beads in a given zone is computed from the weight of the beads.

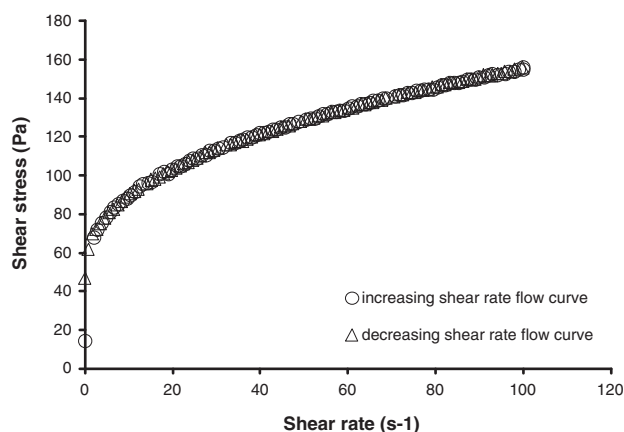


Fig. 1. Flow curve of the carbopol gel.

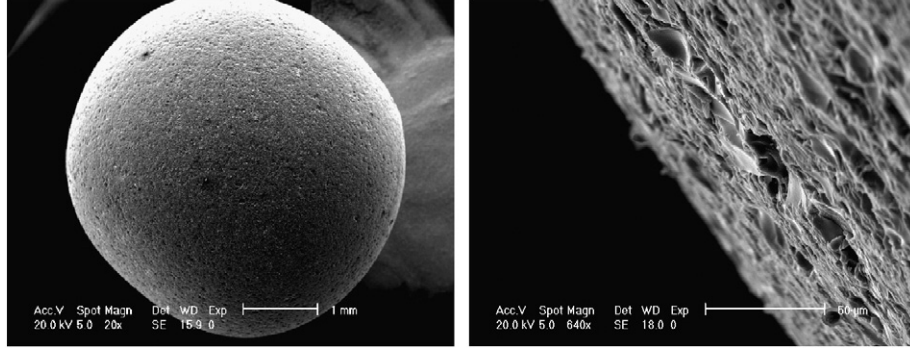


Fig. 2. Surface of the glass beads after abrasion treatment.

4. Numerical simulations

4.1. Prediction of the global flow of the mixture

There exist various numerical techniques allowing for the simulation of the flow of cementitious suspensions [43]. In this paper, a simple and time efficient numerical technique is introduced in order to capture gravity induced particle migration.

Basically, the numerical technique consists in combining the computation of both the global flow of the carboxypol and glass beads mixture and, in parallel, the evolution of the local volume fraction of beads. The global flow of the mixture is computed by solving the mass conservation (continuity) equation together with the momentum conservation equations.

In addition, the constitutive behavior of the fluid (carboxypol and glass beads mixture) is described with a Bingham material model (see the above section) in which the fluid is at rest when the von Mises stress is below the yield stress and flows according to the plastic viscosity when the von Mises stress is larger than the yield stress. In the numerical formulation, this is approximated with the so-called bi-viscosity model in which the initial viscosity μ_{init} which is used below the yield stress (expressed in terms of the threshold shear rate) is very high as compared to the plastic viscosity μ_p which is used above the yield stress, i.e.:

$$\tau^{ref} = \begin{cases} \mu_{init} \dot{\gamma}^{ref} & \dot{\gamma}^{ref} < \dot{\gamma}_0 \\ \mu_p \dot{\gamma}^{ref} + \tau_0 = \mu_{app} \dot{\gamma}^{ref} & \dot{\gamma}^{ref} \geq \dot{\gamma}_0 \end{cases} \quad (6)$$

where $(\tau^{ref})^2 = \frac{3}{2} \tau_{ij} \tau_{ij}$ $\tau_{ij} = \sigma_{ij} - \delta_{ij} \sigma_{kk}/3$ and $(\dot{\gamma}^{ref})^2 = \frac{1}{2} \dot{\gamma}_{ij} \dot{\gamma}_{ij}$

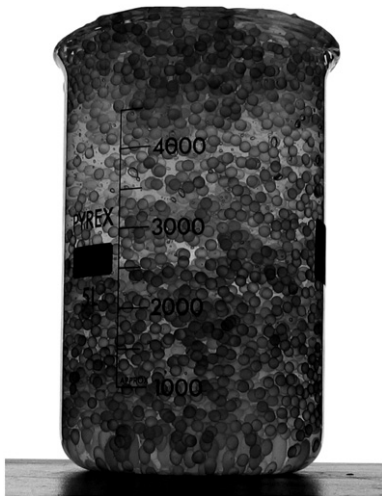


Fig. 3. Homogeneous carboxypol gel and glass beads mixture at the end of the mixing phase.

It should be noted here that the threshold value for this implementation is expressed in terms of the threshold strain rate, which relates to yield stress the following way:

$$\dot{\gamma}_0 = \frac{\tau_0}{\mu_{init}}. \quad (7)$$

When the flow is dominated by shear stress τ and shear rate $\dot{\gamma}$, and the initial viscosity is infinitely large, the equations shown above simplify to the Bingham scalar model:

$$\tau = \tau_0 + \mu_p \dot{\gamma} \quad \text{when} \quad \tau \geq \tau_0. \quad (8)$$

The above numerical technique is implemented in the Computational Fluid Dynamics (CFD) code Flow3D®, which is a general purpose software capable of modelling different fluid flow and heat transfer problems. This software allows the user to program subroutines which take into account specific physical phenomena.

4.2. Prediction of the gravity induced particle migration

The evolution of the particle volume fraction is computed by an advection and a settling calculation. The advection makes the volume fraction follow the streamlines of the global flow, while the settling calculation captures the actual settling of the beads. The settling calculation is derived from a mass conservation of the particles:

$$\frac{\partial \phi}{\partial t} + \text{div}(\phi \vec{V}) = 0 \quad (9)$$

where ϕ is the local particle volume fraction and \vec{V} is the local particle velocity.

In the settling problem studied here, the local particle velocity is a vertical downward settling velocity V_s , which can be derived from Stokes law (Cf. Section 2.3).

$$V_s = -\frac{ga^2 \Delta \rho}{18 \mu_0} \quad (10)$$



Fig. 4. Model formwork filled with the model material.

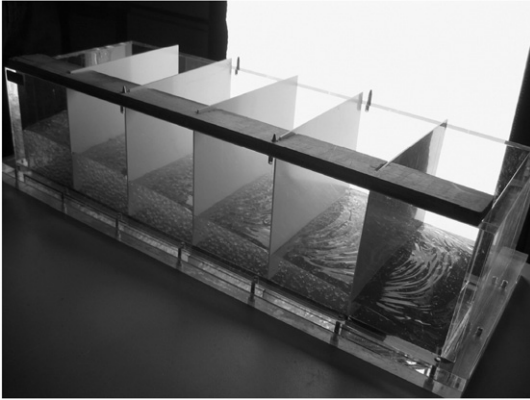


Fig. 5. Zones separation in the model formwork before beads weighting.

where a is the diameter of the glass beads, $\Delta\rho$ is the density difference between the carbopol gel and the glass beads and μ_0 is the local viscosity of the gel around the particle.

As the surrounding fluid is non Newtonian, the question of the nature of the scalar value of this local viscosity arises. The problem is highly three dimensional meaning that several components of the stress tensor may be different from zero. When the components of the stress tensor due to gravity fulfill the von Mises flow criterion, the mixture is flowing. The density difference between the particles and the suspending fluid generates additional stresses in the system. These are combined with the existing stresses at the origin of the global flow of the mixture. Two options can then be considered for the local viscosity of the surrounding fluid. It could either be equal to the apparent viscosity of the material at a shear rate imposed by the flow of the mixture or, as the von Mises criterion is already fulfilled by other components of the stress tensor, to the tangential viscosity (Cf. Fig. 6). In the case of a Bingham fluid model for the suspending fluid, this would be equivalent to considering the plastic viscosity. The gel used in this work can however be described either by a Bingham model for the sake of simplicity or, for a better fit, by a Herschel Bulkley model (Cf. Section 3.1). In the following, we will test the consequences of choosing as an input for the settling numerical simulation the plastic viscosity from the Bingham model, the apparent viscosity from the Herschel Bulkley model or the tangential viscosity from the Herschel Bulkley model (Cf. Fig. 6).

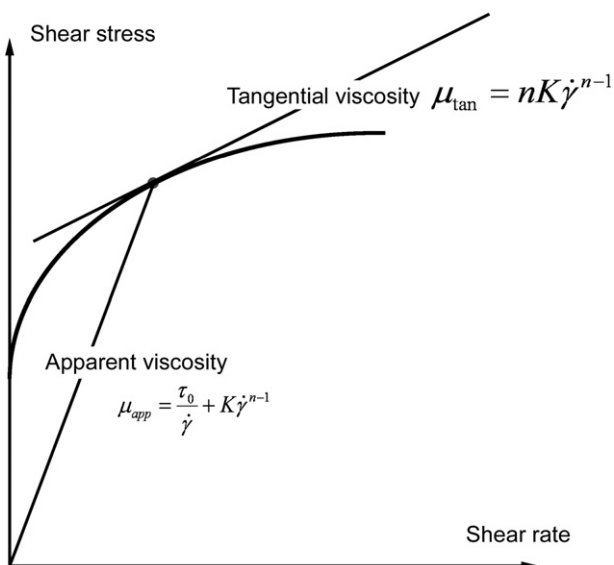


Fig. 6. Apparent and tangential viscosities for a suspending fluid behaving as a Herschel Bulkley material.

Moreover, it can be stressed here once more that, in the simulations carried out in this work, as the influence of the local volume fraction on the local rheology is very low in this range of low volume fractions (see Section 3.1), there is no coupling between the local volume fraction of the glass beads and the rheological behavior of the mixture. Finally, a boundary condition at the bottom of the formwork is implemented to prevent the particles from leaving the computation zone. Additionally, particles are numerically prevented from moving into a cell, in which the dense packing fraction of spheres has already been reached (i.e. 64%).

It can be noted that, in the case of the higher particle volume fractions of real concretes, the above approach would be clearly inappropriate. Particle migration would create a heterogeneous material, in which local viscosity fluctuations due to this migration could play a dominant role in the segregation process. It can be expected that, from a numerical point of view, either advanced discrete methods [44,45] or continuum methods integrating a coupling between local particle volume fraction and drag force [22] would be necessary.

5. Result analysis and discussion

5.1. General description of the experimental results

The measured glass bead volume fractions after the filling of the model formwork are reported in Fig. 7 for the three glass bead diameters. We can first see in this figure that some particle migration is induced by the flow and that the material becomes heterogeneous. This heterogeneity is increasing with the diameter of the glass beads and with the distance from the pouring point. After a flow propagation of 0.6 m, the volume fraction decreases respectively from 10% to 8%, 3% and 1% for the 2, 5 and 7 mm beads. Close to the pouring point, the particle volume fraction is increasing as settling particles gather at the bottom of the model formwork (Cf. Fig. 8).

5.2. Origin of the flow induced particle migration in the model casting

We apply here to our experiments the results from Section 2.6 considering a flow length L of 0.6 m and a flow thickness H of 0.055 m. The initial glass beads concentration ϕ_0 is 10%. The density difference $\Delta\rho$ is 1500 kg/m³ and the beads diameter a varies between 2 and 7 mm. The flow duration is of the order of 90 s and the flow velocity is therefore of the order of 1 cm/s. The shear rate shall then be of the order of 0.1 s⁻¹. μ_0 may either take the value of the tangent viscosity (around 50 Pa s, Cf. Fig. 1 and Fig. 6) or the apparent viscosity (around 450 Pa s, Cf. Fig. 1 and Fig. 6).

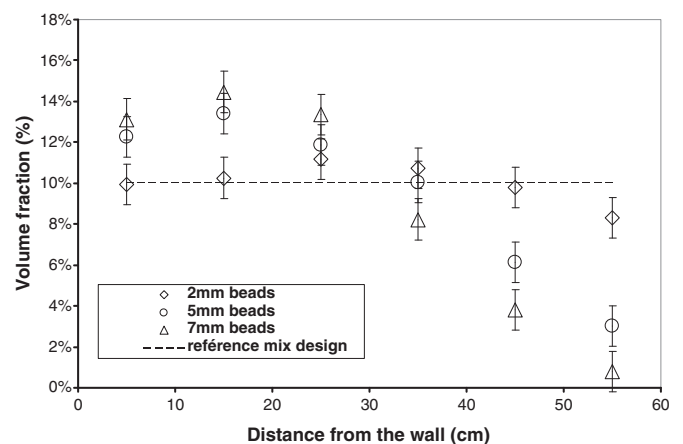


Fig. 7. Measured glass beads volume fractions as a function of the distance in the model formwork.

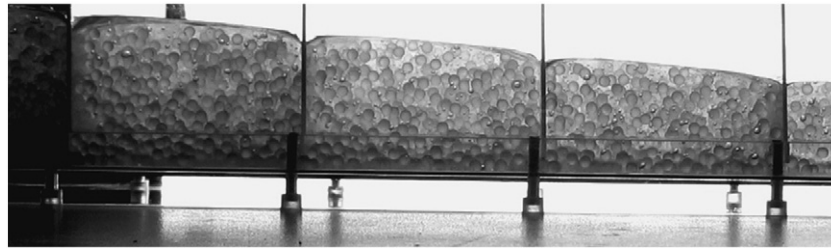


Fig. 8. Glass beads layer at the bottom of the model formwork at the vicinity of the pouring point (7 mm beads).

It can be shown using the relations in Section 2.6 that both shear induced migration and wall effect induced migration are neglectable (Cf. Table 2). This means that, in our experiment as in the casting of fluid concretes, gravity induced heterogeneity dominates all other potential sources of migration. The variations in glass beads volume fraction induced by gravity are then predicted dimensionally to be of the order of 2, 5 and 7% for the glass beads with diameters of 2, 5 and 7 mm if the tangent viscosity is considered and shall respectively be of the order of 0.5, 1 and 2% for the glass beads with diameters of 2, 5 and 7 mm if the apparent viscosity is considered. We can conclude from these estimations that considering the apparent viscosity of the gel results in a strong underestimation of the induced heterogeneity. It can moreover be noted that using the tangential viscosity results in a rather good prediction of the induced migration after 60 cm propagation of the material despite the simplicity of the approaches developed in Section 2.

5.3. Comparison between numerical simulations and experimental results

In Fig. 9, the computed glass beads volume fraction as a function of the distance for three different assumptions on the value of the viscosity of the surrounding carbopol gel is plotted for the 5 mm beads. If we consider for the surrounding fluid the apparent viscosity, numerical simulations underestimate particle migration. If we consider an approximate constant plastic viscosity from the data in Fig. 1, then simulations overestimate the particle migration. It is only when the tangential viscosity is used in the calculation that we obtain a good agreement between simulations and experiments.

This result suggests that the stresses generated by the weight of the mixture fulfill the von Mises flow criterion and are at the origin of the flow. The density difference between the particles and the suspending fluid generates additional stresses in the system. These are combined with the existing stresses at the origin of the global flow

of the mixture. As the von Mises criterion is already fulfilled by other components of the stress tensor, these additional stresses only contribute to the viscous dissipation and do not have to overcome the yield stress to generate a relative flow between the particles and the gel. As a consequence, the settling process is the same as the one that would occur in a zero yield stress fluid. The only parameter of interest is therefore the tangential viscosity.

We compare in Fig. 10 the numerical predictions based on the tangential viscosity and the experimental results for the various glass bead sizes. The overall agreement is satisfactory especially if we bear in mind the simplifying assumptions on which the numerical model is built.

6. Relevance of results to real concretes

There exist two main difficulties when expanding the approach proposed here to the case of real concretes.

First, as the volume fraction of coarse aggregates in concrete is far higher than 10% (it is of the order of 40%), the local rheological properties shall depend on the local volume fraction of coarse aggregates. The problem of particle settling becomes therefore a strongly coupled problem as it does not only create heterogeneity in component proportions but also heterogeneities in local rheological properties, which may in turn affect the global flow of the mixture and therefore particle settling (Cf. Section 4.2).

Second, although the behavior of the suspending fluid can be measured in the case of the model material used here, it is not the case for real concrete. It can be expected that the rheological properties to be taken into account shall be between the concrete scale and the mortar scale. Also, the behavior shall be shear thinning as for the carbopol used here. It is however difficult to identify this behavior apart except by using an inverse analysis of a real life flow induced segregation case. As this behavior shall strongly depend on mix design, this type of approach shall only give data for the specific case studied.

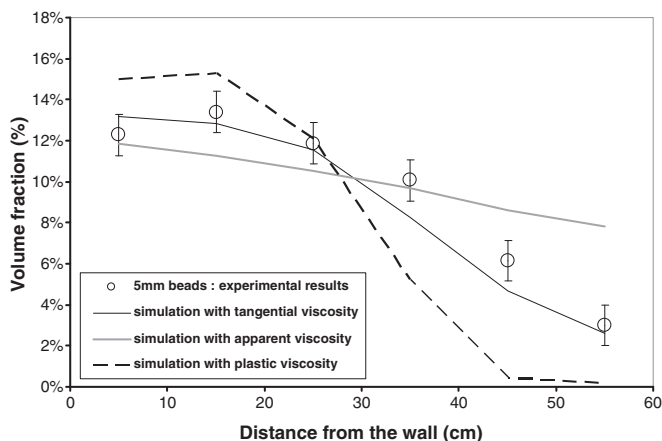


Fig. 9. Glass beads volume fraction as a function of distance for the 5 mm beads. Comparison between experimental results and numerical simulations for various assumptions for the viscosity of the suspending fluid. The yield stress is 40 Pa.

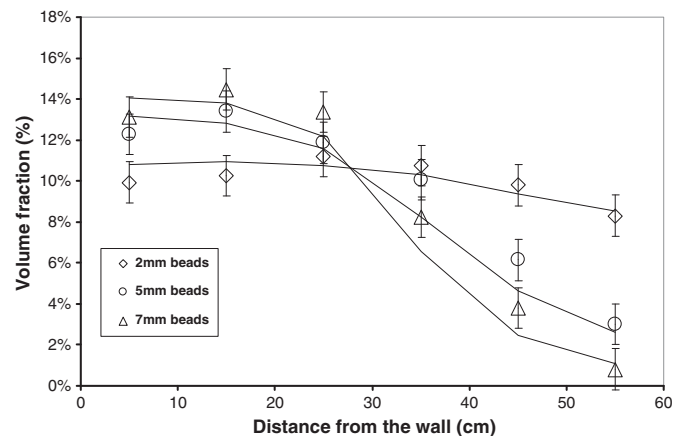


Fig. 10. Glass beads volume fraction as a function of distance for the 2, 5 and 7 mm beads. Comparison between experimental results and numerical simulations considering the tangential viscosity of the surrounding fluid.

We have shown in this paper that the tangential viscosity of the suspending fluid is dictating particle settling. It shall also be the case for real concretes no matter the rheological behavior of the suspending fluid to be considered. The characteristic time of gravity induced segregation (Eq. (4)) then becomes:

$$T_c^{\text{gravity}} \approx \frac{H}{V_s} = \frac{18nK\dot{\gamma}^{n-1}H}{g\Delta\rho a^2}. \quad (11)$$

The dimensionless ratio between the duration of the casting process T_f and the above characteristic time gives an idea of the magnitude of the gravity induced segregation for a given process and element to be cast. It scales with the casting velocity as:

$$\frac{T_f}{T_c^{\text{gravity}}} \approx V^{-n}. \quad (12)$$

As n shall always be positive, it can therefore be expected that, from a practical point of view, the magnitude of gravity induced segregation shall decrease for fast casting processes. Though intuitively correct, this result has however still to be validated at the scale of concrete. It could indeed be affected by the thixotropic nature of concrete: at high flow rates, the structural break down of the cement paste could lower the tangential viscosity and enhance gravity induced segregation.

7. Conclusions

In this paper, we have described and compared the various physical phenomena which potentially lead to flow induced particle migration in concrete. It was shown that shear induced particle migration and wall effect induced particle migration dominate in the pumping process whereas, in the case of industrial casting of concrete, gravity induced particle migration dominates all other potential sources of heterogeneities induced by flow.

In the second part, we have shown, from comparisons between experiments using model materials, dimensional analysis and numerical simulations, that, from a quantitative point of view, the viscous drag force, which prevents particles from migrating during a casting process, shall neither be computed from the apparent viscosity nor from plastic viscosity of the suspending phase but from its tangential viscosity.

We have moreover shown that it is possible to numerically predict flow induced particle migration during casting of a model material, which was designed to mimic self compacting concrete.

Finally, the transfer of this type of numerical prediction tool to real concrete was discussed.

Acknowledgment

The work is funded by the Danish Agency for Science Technology and Innovation (project 09-065049/FTP: Prediction of flow induced inhomogeneities in self compacting concrete).

References

- [1] A.W. Saak, H. Jenning, S. Shah, New methodology for designing self-compacting concrete, *ACI Mater. J.* 98 (6) (2001) 429–439.
- [2] N. Roussel, A theoretical frame to study stability of fresh concrete, *Mater. Struct.* 39 (2006) 81–91.
- [3] M.F. Petrou, B. Wan, F. Galada-Maria, V.G. Kolli, K.A. Harries, Influence of mortar rheology on aggregate settlement, *ACI Mater. J.* 97 (4) (2000) 479–485.
- [4] M.F. Petrou, K.A. Harries, F. Galada-Maria, V.G. Kolli, A unique experimental method for monitoring aggregate settlement in concrete, *Cem. Concr. Res.* 30 (2000) 809–816.
- [5] D. Leighton, A. Acrivos, The shear-induced migration of particles in concentrated suspensions, *J. Fluid Mech.* 181 (1987) 415–439.
- [6] R.J. Phillips, R.C. Armstrong, R.A. Brown, A.L. Graham, J.R. Abbott, A constitutive equation for concentrated suspensions that accounts for shear-induced particle migration, *Phys. Fluids* 4 (1992) 30–40.
- [7] D. Leighton, A. Acrivos, Measurement of shear-induced self-diffusion in concentrated suspensions of spheres, *J. Fluid Mech.* 177 (1987) 109–131.
- [8] A. Acrivos, Bingham award lecture—1994 Shear-induced particle diffusion in concentrated suspensions of noncolloidal particles, *J. Rheol.* 39 (1995) 813–826.
- [9] G. Ovarlez, F. Bertrand, S. Rodts, Local determination of the constitutive law of a dense suspension of noncolloidal particles through magnetic resonance imaging, *J. Rheol.* 50 (2006) 259–292.
- [10] Feys, D., Interactions between rheological properties and pumping of self-compacting concrete, PhD. Uni Ghent (2009).
- [11] S. Jacobsen, L. Hauganb, T.A. Hammer, E. Kalogiannidis, Flow conditions of fresh mortar and concrete in different pipes, *Cement Concr. Res.* 39 (11) (2009) 997–1006.
- [12] D. Kaplan, Pompage des bétons, Etudes des recherches des laboratoires des Ponts et Chaussées, Laboratoire Central des Ponts et Chaussées, Paris, 2001 (in French).
- [13] Ngo, T.T., Influence de la composition des bétons sur les paramètres de pompage et validation d'un modèle de prévision de la constante visqueuse, PhD. Uni Cergy Pontoise (2009) (In French).
- [14] H. Hafid, G. Ovarlez, F. Toussaint, P.H. Jezequel, N. Roussel, Estimating measurement artifacts in concrete rheometers from MRI measurement on model materials, Design, Production and Placement of Self-Consolidating Concrete, Proceedings of SCC2010, Montreal, Canada, , 2010.
- [15] Seung Hee Kwon, Seon-Doo Jo, Kyu Park, Jae-Hong Jeong, Seung-Hoon Lee Computational estimation of slip-layer in pipe flow of concrete, proceedings of the 9th International Symposium on High Performance Concrete, 9–11th of August 2011, Rotorua, New Zealand, 2011.
- [16] G.Y. Onoda, E.G. Liniger, Random loose packings of uniform spheres and the dilatancy onset, *Phys. Rev. Lett.* 64 (1990) 2727–2730.
- [17] J. Yammine, M. Chaouche, M. Guerin, M. Morandville, N. Roussel, From ordinary rheology concrete to self compacting concrete: a transition between frictional and hydrodynamic interactions, *Cem. Concr. Res.* 38 (2008) 890–896.
- [18] N. Roussel, A. Lemaître, R.J. Flatt, P. Coussot, Steady state flow of cement suspensions: a micromechanical state of the art, *Cement Concr. Res.* 40 (2010) 77–84.
- [19] A.M. Corbett, R.J. Phillips, R.J. Kauten, K.L. McCarthy, Magnetic resonance imaging of concentration and velocity profiles of pure fluids and solid suspensions in rotating geometries, *J. Rheol.* 39 (1995) 907–924.
- [20] A.L. Graham, S.A. Altobelli, E. Fukushima, L.A. Mondy, T.S. Stephens, Note: NMR imaging of shear-induced diffusion and structure in concentrated suspensions undergoing Couette flow, *J. Rheol.* 35 (1991) 191–201.
- [21] J.R. Abbott, N. Tetlow, A.L. Graham, S.A. Altobelli, E. Fukushima, L.A. Mondy, T.S. Stephens, Experimental observations of particle migration in concentrated suspensions: Couette flow, *J. Rheol.* 35 (1991) 773–795.
- [22] L. Shen, L. Struble, D. Lange, Modeling dynamic segregation of self-consolidating concrete, *ACI Mater. J.* 106 (4) (2009) 375–380.
- [23] D. Lowke, T. Kränkel, C. Gehlen, P. Shiessl, Effect of cement on super plasticizer adsorption, Yield stress, Thixotropy and Segregation resistance, in: K. Khayat, D. Feys (Eds.), Proceedings of SCC2010, Montreal, Canada, Springer, 2010, pp. 91–102.
- [24] N. Roussel, A thixotropic model for fresh fluid concretes: theory, validation and applications, *Cement Concr. Res.* 36 (10) (2006) 1797–1806.
- [25] N. Roussel, Steady and transient flow behaviour of fresh cement pastes, *Cement Concr. Res.* 35 (9) (2005) 1656–1664.
- [26] NF EN 1992-1-1 Eurocode 2 (2005).
- [27] T. Sedran, F. de Larrard, Optimization of self compacting concrete thanks to packing model, RILEM Symposium on Self Compacting Concrete, September 1999, pp. 321–332, Stockholm, 13–15.
- [28] N. Roussel, T.L.H. Nguyen, O. Yazoghli, P. Coussot, Passing ability of fresh concrete: a probabilistic approach, *Cement Concr. Res.* 39 (2009) 227–232.
- [29] F. Chevoir, F. Gaulard, N. Roussel, Flow and jamming of granular mixtures through obstacles, *Europhysics Lett.* 79 (2007) 14001.
- [30] N. Roussel, T.L.H. Nguyen, P. Coussot, General probabilistic approach of filtration process, *Phys. Rev. Lett.* 98 (11) (2007) 114502.
- [31] Tam, C.T., Shein, A.M.M., Ong, K.C.G., Chay, C.Y., Modified J-ring approach for assessing passing ability of SCC, proceedings of SCC 2005, published by Hanley Wood, 2005.
- [32] I.Y.T. Ng, H.H.C. Wong, A.K.H. Kwan, Passing ability and segregation stability of self-consolidating concrete with different aggregate proportions, *Mag. Concr. Res.* 58 (6) (2006) 447–457.
- [33] T.L.H. Nguyen, N. Roussel, P. Coussot, Correlation between L-box test and rheological parameters of an homogeneous yield stress fluid, *Cement Concr. Res.* 36 (10) (2006) 1789–1796.
- [34] F. de Larrard, Concrete Mixture Proportioning, E & FN Spon, London, 1999.
- [35] O. Wallevik, Rheology — a scientific approach to develop self-compacting concrete, Proceedings of the 3rd international RILEM Symposium on Self-Compacting Concrete, Reykjavik, Iceland, 2003, pp. 23–31, (RILEM PRO33, 2003).
- [36] N. Roussel, The LCPC BOX: a cheap and simple technique for yield stress measurements of SCC, *Mater. Struct.* 40 (9) (2007) 889–896.
- [37] C.F. Ferraris, L.E. Brower (Eds.), Comparison of concrete rheometers: international tests at LCPC (Nantes, France) in October, 2000, National Institute of Standards and Technology Interagency Report (NISTIR) 6819., , 2001.
- [38] C.F. Ferraris, L.E. Brower (Eds.), Comparison of concrete rheometers: international tests at MB (Cleveland OH, USA) in May, 2003, National Institute of Standards and Technology Interagency Report (NISTIR) 7154., , 2004.
- [39] Nguyen, T.L.H. (2007) « Outils pour la modélisation de la mise en œuvre des bétons », Doctoral thesis, Laboratoire central des Ponts et chaussées, ENPC p.122 (in French).
- [40] X. Chateau, G. Ovarlez, K.L. Trung, Homogenization approach to the behavior of suspensions of noncolloidal particles in yield stress fluids, *J. Rheol.* 52 (2008) 489–506.

- [41] F. Mahaut, S. Mokkaddem, X. Chateau, N. Roussel, G. Ovarlez, Effect of coarse particle volume fraction on the yield stress and thixotropy of cementitious materials, *Cem. Concr. Res.* 38 (2008) 1276–1285.
- [42] N. Roussel, Correlation between yield stress and slump: comparison between numerical simulations and concrete rheometers results, *Mater. Struct.* 39 (4) (2006) 501–509.
- [43] N. Roussel, M.R. Geiker, F. Dufour, L.N. Thrane, P. Szabo, Computational modeling of concrete flow: general overview, *Cement Concr. Res.* 37 (9) (2007) 1298–1307.
- [44] N.S. Martys, Study of a dissipative particle dynamics based approach for modeling suspensions, *J. Rheol.* 49 (2) (2005) 401–424.
- [45] N. Martys, C.F. Ferraris, Simulation of SCC flow, *Proc. 1st North American Conf. on the design and use of Self-Consolidating Concrete*, Chicago, IL, 2002, pp. 27–30.

C PAPER-III

J. Spangenberg, N. Roussel, J. H. Hattel, E. V. Sarmiento, G. Zirculis and M. R. Geiker (2012). Patterns of gravity induced aggregate migration during casting of fluid concretes, *Cement and Concrete Research*, Accepted.

PATTERNS OF GRAVITY INDUCED AGGREGATE MIGRATION DURING CASTING OF FLUID CONCRETES

J. Spangenberg¹, N. Roussel^{2*}, J.H. Hattel¹, E.V. Sarmiento³, G. Zirgulis³, and M.R. Geiker^{3,4}

¹ Department of Mechanical Engineering, Technical University of Denmark (DTU), Denmark

² Université Paris Est, Laboratoire Central des Ponts et Chaussées (LCPC), France

³ Department of Structural Engineering, Norwegian University of Science and Technology
(NTNU), Norway

⁴ Department of Civil Engineering, Technical University of Denmark (DTU), Denmark

* : corresponding author

Abstract

In this paper, aggregate migration patterns during fluid concrete castings are studied through experiments, dimensionless approach and numerical modelling. The experimental results obtained on two beams show that gravity induced migration is primarily affecting the coarsest aggregates resulting in a decrease of coarse aggregates volume fraction with the horizontal distance from the pouring point and in a puzzling vertical multi-layer structure. The origin of this multi layer structure is discussed and analyzed with the help of numerical simulations of free surface flow. Our results suggest that it finds its origin in the non Newtonian nature of fresh concrete and that increasing casting rate shall decrease the magnitude of gravity induced particle migration.

Keywords

Fresh Concrete (A), Rheology (A), Aggregate (D), Yield stress.

1. Introduction

Self-consolidating concrete (SCC) is characterized by a high fluidity allowing for the easy filling of formwork without compaction but sufficient stability to ensure uniform suspension of solid particles during placement. Stability requires that the material is at least stable at rest (*i.e.* not flowing). This implies that the constitutive cement paste yield stress is sufficient to resist the density difference between coarse aggregates and suspending matrix [1, 2].

This criterion is not sufficient to ensure mixture homogeneity during placement. It has indeed been shown recently [3, 4] that a concrete, which is stable at rest, can be unstable during flow. Several phenomena such as shear or gravity induced migration can lead to heterogeneities in the aggregates' local volume fraction in the hardened structural element [4]. Gravity induced particle migration was shown to dominate during casting of structural elements [4]. When the material flows, the stress generated by gravity in the mixture is higher than the concrete yield stress. This means that any additional stress, such as the one generated by a density difference between an aggregate and the surrounding mixture, could induce a local flow around the aggregate even if this additional stress itself is lower than the yield stress [4].

One could then expect that, as the yield stress is exceeded gravity induced particle migration shall be similar to the one measured in Newtonian fluids. However, because of the non Newtonian nature of concrete and because of the typical flow typology during casting, gravity induced particle migration is far more complex. In the present work, the casting of two identical beams at two different casting rates is studied. The self compacting concrete studied here was stable at rest. However, we measured in the beam some gravity induced particle migration during casting. This migration resulted in a decrease of the coarsest aggregates' volume fraction as a function of the distance from the pouring point but it also lead to a

puzzling vertical multilayer structure. This phenomenon is analyzed and discussed with the use of simple physical analysis and numerical simulations.

2. Materials and Protocols

2.1. Materials

The concrete used in this study was produced at a local concrete producer in Norway. It is typical of Northern Europe Self Compacting Concrete production with a relatively high content of high quality aggregates and a viscosity agent. Its mix proportions are given in Tab. 1. The particle size distribution for both sand and gravel are shown in Fig. 1. The dense packing fraction of the two aggregate fractions was measured using the method developed at the Danish Technological Institute [5]. The 4C packing software also developed at the Danish Technological Institute was then used to compute a dense packing fraction of 0.75 for the combination of the two fractions [6]. A retardation agent was used in order to allow for enough time for the experimental work to be carried out.

2.2. Casting process

Two identical beams were cast with the concrete described above at two different casting rates. The dimensions of the beams were length 4 m, width 0.2 m, and height 0.3 m (Cf. Fig. 2). One beam was studied while the concrete was still fresh (low casting rate) while the other was studied after hardening (high casting rate). The beam studied in the hardened state was reinforced with two 8 mm bars for demoulding and transportation purposes. The concrete was poured directly and continuously from the concrete truck at a distance of approximately 0.3 m from one end of the beams. The pouring position did not change during the filling process in order to have as simple a casting scenario as possible. Consequently, the moulds were not fully filled and the filling process was stopped when concrete reached the top of the formwork

closest to the pouring zone (Cf. Fig. 2). For the lowest casting rate, the duration of the filling process was 160 s corresponding to a mass rate of concrete entering the formwork of 2.9 kg/s.

For the highest casting rate, the duration of the filling process was 60 s corresponding to a mass rate of concrete entering the formwork of 7.7 kg/s.

For the beam cast at the low casting rate, the induced horizontal heterogeneity was measured in the fresh state by measuring the aggregate content in the nine sub-regions illustrated on the sketch in Fig 2. After casting, some custom-made steel plates working as barriers were inserted in the concrete. The extracted fresh concrete samples were washed and sieved and the amount of aggregates belonging to the fractions 6/11 mm and 11/16 mm were measured.

The beam cast at the high casting rate was cut in the middle of the nine sub-regions shown in Fig. 2 after setting. Image analysis of the vertical sections allowed for the determination of the concentration of 11/16 mm aggregates in three zones (upper, middle and lower zone) in each section. The thickness of each zone was approximately one third of the height in the specific cut.

2.3.Fresh properties measurements

Measurement of fresh properties of concrete is a delicate issue. Large scale rheometers dedicated to concrete have been developed in the last decades (BTRheom [7], BML [8] or two-point test [9]) but, even if these apparatus represent a big step forward in the field of concrete science, there still exists a discrepancy between the various concrete rheometers, [10, 11]. The apparatus give the same rheological classification of materials, but they do not give the same absolute values of the rheological parameters. It was recently suggested that this discrepancy finds its origin in the shear induced particle migration that occurs in these confined high shear rates flows [12]. We therefore choose in the following to use a simple

industrial test, which allows for a computation of approximate values for the rheological parameters of the material.

2.3.1. LCPC box test

The yield stress of the studied concrete was measured using the LCPC box test [13-15]. This test requires the same amount of concrete to be tested as the slump flow test, but fulfils the minimum thickness condition allowing for an analytical relation between the test result and the yield stress of the tested material. The analysis of the test takes into account the shear stress at the lateral walls and at the bottom wall of the box to predict the shape at stoppage of a given volume of a yield stress fluid flowing slowly enough for any inertia effects to be negligible. The excellent agreement of this method with other experimental measurements was demonstrated in the case of limestone powder suspensions [14]. In the present study, a slump flow test was also carried out in parallel.

2.3.2. T500 measurements

The plastic viscosity of the studied concrete was roughly estimated from T500 measurements. It is interesting to note here that, although the final thickness of the sample in a slump flow test is too small compared to the size of the coarsest particles to get any quantitative information on yield stress when flow stops [13-15], the thickness of the sample is roughly in the order of several cm when the spread reaches 500 mm. As a consequence, it is possible to compute an approximate value of the plastic viscosity from this measurement.

We first assume that the lifting of the cone and the phase during which the material slumps under a mainly tensile strain rate state [16] do not last more than a few tenths of second. After this initial phase, the ratio between the radius of the sample and its thickness becomes high enough to assume that shear stresses dominate the stress tensor [16].

In this regime, the shear rate may be approximated as $\dot{\gamma} \cong V/h$ where V is the horizontal velocity, the average value of which is $0.25/T_{500}$, where T_{500} is the measured flow time to reach a spread diameter of 500 mm (*i.e.* a spread radius of 0.25 m). h is the thickness of the sample that we approximate here as $Vol/\pi(0.25)^2$ assuming a flat cylindrical shape of the sample. Vol is the volume of the sample and is of the order of 6 litres. As a consequence, h and $\dot{\gamma}$ are respectively in the order of 3 cm and between 2 and 20 s⁻¹ for T_{500} values between 0.5 and 5 s. These values are in agreement with numerical simulations of slump test and slump flow test [17]. The stress generated by gravity is in the order of $\tau \cong \rho gh$, where ρ is the density of the concrete. The plastic viscosity can then be estimated as $\mu_p \cong (\tau - \tau_0)/\dot{\gamma}$ or $\mu_p \cong 4(\rho gh - \tau_0)hT_{500} = 0.12(0.3\rho - \tau_0)T_{500}$. The yield stress value can be measured by the LCPC box test described above. It shall be noted that this relation should not hold for very low plastic viscosity concretes, for which inertia effects start to play a role [16] or for high plastic viscosity concretes for which the duration of the initial slumping phase can be longer than a few tenths of seconds.

2.3.3. Static segregation

The concrete was tested for its static segregation resistance by placing aggregates of different sizes on top of a sample inside a bucket. In parallel, a visual evaluation of stability was carried out.

3. Experimental results

3.1. Fresh properties measurements

The obtained measurements are presented in Tab. 2.

3.2. Heterogeneities measurements

First, it can be noted that, for the two beams, coarse aggregates were visible at the surface of the concrete suggesting that no segregation occurred during casting. The numbers of visible coarse grains however dropped in the last third of the beam.

Measurements of 6-11 mm and 11-16 mm aggregates volume fractions in fresh state by sampling and sieving are presented in Fig. 3. These two granular classes are initially present in the mix at the volume fractions of 17 and 16 %, respectively. Our measurements suggest that only the coarsest grains in the mix do migrate during flow. Moreover, as seen in Fig.3, there does not seem to be any segregation in the first two thirds of the beam where the aggregate volume fraction is more or less equal to the reference mix design volume fraction.

However, the image analysis of the hardened cut samples shows that things are in fact more complex. Similarly to the measurements in fresh state, the total coarsest aggregate volume fraction, after a plateau in the first two thirds of the beam, decreases in the last third, Fig. 3. This suggests that, in most of the beam, the total volume fraction of aggregates in a vertical section is more or less equal to the reference mix design volume fraction. However, when focusing on the upper, middle and lower zone in each section, there exists a strong vertical heterogeneity in the sample as shown in Fig. 4 where a multilayer material seems to have been created. In this figure, the average value of the aggregates counting measurements in the first three meters of the beam are plotted. These results suggest that, in the upper zone, there is no segregation. They moreover suggest that particle depletion from the middle zone results in an accumulation of particles in the lower zone. A peak in the aggregates volume fraction in the bottom zone was noted between 1 and 1.5m from the pouring point.

4. Analysis and discussion

4.1. Particle migration regime

In this section, the consequences of the physical phenomena resulting in particle distribution heterogeneities are compared in the case of the beams studied here. It has to be kept in mind that variations in the local particle volume fraction will always be induced by the presence of walls or more generally interfaces. This phenomenon is not induced by flow but, because of simple geometrical considerations, it is not possible to find the centre of a particle of diameter a at a distance from a wall lower than $a/2$ [18]. Because of this wall effect, there exists some heterogeneity at the vicinity of any solid interface. In the case of a beam such as the ones studied in this paper, this effect shall be constant along the beam and cannot therefore explain any decrease in particle volume fractions along the beam. When there are no steel bars and therefore no granular blocking [19-25], two other types of flow induced particle migration may occur as identified in [4]: shear induced particle migration and gravity induced particle migration.

Shear induced particle migration

Shear induced particle migration finds its origin in the competition between gradients in particle collision frequency and gradients in the viscosity of the suspension.

It was shown in [4] that shear induced particle migration shall reach its full extent after a characteristic shear induced particle migration time T_c^{shear} in the order of:

$$T_c^{shear} = \frac{H^2}{10a^2\phi_0^2\dot{\gamma}} \quad (1)$$

The thickness H of the beam is in the order of 0.3 m. In the beam, the material flows at an average casting velocity V and is subjected to an average shear rate $\dot{\gamma}$ with $\dot{\gamma} = V/H$. ϕ_0 is the mix design particle volume fraction or initial particle volume fraction of size a . In the case of the beams studied here, the characteristic shear induced particle migration time T_c^{shear} is of the order of several thousands seconds for the coarsest particles. This is far higher than

the duration of the casting process. As a consequence, the migration measured in Fig. 3 can not result from this physical phenomenon.

Gravity induced particle migration

When the material flows, the stress generated by gravity in some zones of the mixture is higher than the yield stress of the material. This means that any additional stress, such as the one generated by a density difference between an aggregate and the surrounding mixture, could induce a local flow around the aggregate even if this additional stress itself is lower than the yield stress [4].

It was shown in [4] that the highest variation in particle volume fraction due to gravity induced particle migration is of the same order as the one due to shear induced particle migration. The characteristic time associated with this process is however very different and can be estimated as:

$$T_c^{gravity} \cong \frac{18\mu_s H}{g\Delta\rho a^2} \quad (2)$$

$\Delta\rho$ is the density difference between the aggregates and the suspending phase. μ_s is the apparent viscosity of the suspending phase (*i.e.* the ratio between shear stress and shear rate). The typical value of the viscosity of the so-called suspending fluid is delicate to identify. If we consider as in [4] that the suspending phase for the coarsest aggregates shall locate somewhere between the mortar scale and the concrete scale itself, we can consider $\mu_s = 10$ Pa.s as an order of magnitude.

In the case of the beams studied here, the characteristic gravity induced particle migration time $T_c^{gravity}$ is respectively in the order of 50 seconds for the 11-16 mm particles and 200 seconds for the 6-11 mm particles. These values are of the same order as the duration of the casting process. This suggests that the migration measured in Fig. 3 results from this physical phenomenon. The relative values of the $T_c^{gravity}$ for the two sizes of particles moreover suggest

that the magnitude of gravity induced migration should decrease by a factor 4 between the 11-16mm and the 6-11 mm aggregates. This is approximately the case for the results shown in Fig. 3 where the 11-16 mm and the 6-11 mm aggregate volume fractions decrease by 20 and 65 %, respectively.

4.2. Influence of flow typology on gravity induced particle migration

In the previous section, it was shown that gravity induced particle migration can explain the heterogeneities shown in Fig. 3. However, the influence of the non-Newtonian behaviour of the material was not taken into account into the above simple dimensionless approach. All the material was assumed to be sheared and the apparent viscosity of the suspending phase was assumed to be constant through the casting process.

However, during the casting process, only a part of the material is sheared. There exist zones where the stress stays lower than the yield stress and zones where the stress exceeds the yield stress and flow occurs. It is possible to consider that there exist two laminar regimes during the horizontal casting of a fluid concrete. In the first transient regime (Cf. Fig. 5), the material is propagating mostly horizontally in the formwork until it reaches the opposite end of the inlet. The propagation length $L(t)$ increases from zero to the length of the beam. In the second regime (Cf. Fig. 6), the material has reached the opposite wall. The velocity is still mostly horizontal but, as the boundary conditions are only slightly changing in this regime, the flow can be approximated as a steady flow.

Because of stress equilibrium, in both regimes, the stress increases linearly from zero at the free surface to a maximum value at the bottom interface. This means that there shall exist a zone just below the free surface where the material is not sheared and flows as a plug (Cf. Fig. 5 and 6). In this zone, the material behaves like a solid (*i.e.* the stress is below the yield stress) and its apparent viscosity shall be infinite. If the material is a stable material from a static

segregation point of view (*i.e.* at rest, the aggregates do not settle), no gravity induced migration shall occur. As a consequence, there shall exist an upper layer where the aggregate volume fraction stays equal to the initial or mix design volume fraction.

Below this layer, the material is sheared and particles can settle through this fluid material. They settle with a settling velocity V_s , which depends on the suspending fluid's apparent viscosity, the diameter of the particles considered and the density difference between surrounding fluid and particles. The particles deposit at the bottom of the formwork where they pile up to the so-called random loose packing (*i.e.* the lowest volume fraction value allowing for a percolated network of contacts between particles) [4]. We suggest that it is these coupled phenomena (*i.e.* upper plug flow layer where no gravity induced migration occurs, intermediate sheared layer that gets depleted from particles and lower layer where the particles gets accumulated) which give rise to the vertical multi-layer structure measured above and shown in Fig. 4.

In the first regime (Cf. Fig. 5), at a time t after the beginning of the casting process, the aggregates volume fraction in the sheared zone above the deposit has decreased. The residual volume fraction at a position x from the casting point ($0 \leq x \leq L(t)$) writes $\phi_0(1 - V_s x / H_s V_H)$ where H_s and V_H are respectively the thickness of the sheared zone and the horizontal velocity. Similarly, the volume fraction of deposited particles can be written as $\phi_0(1 + V_s(L(t) - x) / H_s V_H)$. This suggests that, in this regime, the concentration profile decreases with the distance from the casting point. There is moreover a competition between settling velocity and casting velocity, which shall dictate the magnitude of the induced horizontal heterogeneity. It has to be kept in mind that, according to [4], increasing casting velocity for shear thinning materials such as concrete shall reduce the suspending fluid's viscosity while decreasing the time during which particles are migrating. The experimental results obtained in [4] on model materials seem to suggest that it is this last effect which

dominates and that, therefore, increasing casting velocity shall decrease the induced horizontal heterogeneity.

In the second regime (Cf. Fig. 6), the particle depletion rate from the sheared layer and the deposition rate in the lower layer are constant along the beam. The residual volume fraction in the sheared layer writes $\phi_0(1 - V_s H(t) / H_s V_v)$ where V_v is the vertical filling velocity.

Similarly, the volume fraction of deposited particles can be written as $\phi_0(1 + V_s H(t) / H_s V_v)$.

This suggests that the concentration profile along the beam shall be constant. The only gravity induced heterogeneity shall be vertical and corresponds to the multi-layer structure. This vertical heterogeneity shall increase with time. Here again, there is a competition between settling velocity and casting velocity, which shall dictate the magnitude of the induced vertical heterogeneity.

For a fluid concrete such as SCC and a beam of limited length, it is possible to assume that the first regime in Fig. 5 will be short and that its contribution to the final concentration profile shall be neglectable. We can therefore expect to get a constant concentration profile along the beam. This is indeed what we measure in the first two thirds of the beam as shown in Fig. 3. However, a drop in concentration and a drop in the number of visible aggregates at the surface of the concrete were measured in the last third of the beam. We can therefore expect that something else is affecting the concentration profile.

In the previous analysis, we did not take into account the fact that particle migration induces not only a heterogeneous solid content field but also affects local rheological properties. The zones depleted from the coarsest particles become more fluid whereas the zones where coarse particles accumulate display higher yield stress and viscosity. Such a complex coupling between particle migration and local rheological properties prevents the use of any simple analysis of the global flow pattern. In the next section, we use numerical simulations to go

one step further in the understanding of the patterns of gravity induced particle migration during flow of fluid concretes.

5. Numerical model

In this section, the numerical simulation tools used to model gravity induced segregation in this work are described. The strategy is to choose the simplest models available in literature in order to minimize the number of parameters to be fitted.

A two dimensional computational fluid dynamics (CFD) code used to simulate the flow induced particle migration in this study was developed in the technical computing language MATLAB and was based on the methodology presented in [4]. The particle migration is modeled by taking the following three physical phenomena into account.

1. The global free surface non-Newtonian SCC flow
2. The gravity induced aggregate migration
3. The effect of local aggregate volume fraction on local rheological parameters

Each of the physical phenomena and their numerical implementation are shortly reviewed in the following three sections.

5.1. The global non-Newtonian SCC flow

The SCC flow behaviour is non-Newtonian and the numerical model captures it by solving the continuity equation together with the momentum equations. The Finite Volume Method (FVM) was used to discretize the governing equations in order to compute pressure and velocity fields on a staggered grid, Cf. [26]. The pressure and viscous stresses are computed implicitly with a direct solver while the non-linearity represented by the convective terms in

the momentum equations is updated explicitly. The free surface is also updated explicitly and is tracked using the Volume Of Fluid (VOF) method [27, 28].

The Bingham material model is typically the constitutive law used to describe the flow behaviour of SCC [29]. However, a numerical flow model cannot handle the exact Bingham material model due to infinitely high apparent viscosities in the zones where shear rate approaches zero. Therefore, the Bingham material model is approximated here with the bi-viscosity material model [4].

5.2. Gravity induced particle migration

The aggregate migration is computed through an advection and a settling calculation. The settling procedure is carried out by solving Eq. (3).

$$\frac{\partial \phi}{\partial t} + \nabla(\phi V_s) = 0 \quad (3)$$

Where V_s is the settling velocity vector. This settling velocity is computed using Eq. (4), which evaluates how gravity, buoyancy and Stokes drag force affect a spherical particle (aggregate).

$$V_s = \frac{g \Delta \rho a^2}{18 \mu_s} \quad (4)$$

Where a is the diameter of the aggregate, $\Delta \rho$ is the density difference between the aggregates and the surrounding material, and μ_s is the local surrounding viscosity of the suspending fluid. The value of this viscosity is investigated further in this paper. In addition, it should be noted that aggregates were numerically prevented from settling out of the domain and into a cell, in which the packing fraction of aggregates had already reached the measured dense packing fraction of 0.75.

5.3. Local rheological parameters and local volume fraction

In this work, the rheological parameters' dependency on the aggregate volume fraction is approximated from simple but well documented analytical relationships for mono-sized spherical particles. The yield stress' dependency on the local aggregate volume fraction is based on Chateau *et al.* [30, 31]:

$$\frac{\tau_0(\phi)}{\tau_0(0)} = \sqrt{\left(1 - \phi\right) \left(1 - \frac{\phi}{\phi_m}\right)^{-2.5\phi_m}} \quad (5)$$

where ϕ_m is the dense packing fraction of the mono-sized spherical particles. The plastic viscosity's dependency on the local aggregate volume fraction is based on Krieger and Dougherty [32] as follows:

$$\frac{\mu_p(\phi)}{\mu_p(0)} = \left(1 - \frac{\phi}{\phi_m}\right)^{-2.5\phi_m} \quad (6)$$

The local surrounding viscosity used in the computation of the local settling velocity is expressed as a function of the local apparent viscosity of the surrounding concrete.

$$\mu_s = \frac{1}{\alpha} \left(\mu_p(\phi) + \frac{\tau_0(\phi)}{\sqrt{I_2}} \right) \quad (7)$$

Where I_2 is the local second invariant of the strain rate tensor and α is a scalar that shall be equal or higher than 1. α is the only fitted parameter in this study. When α equals 1, the surrounding fluid has the same behaviour as the tested concrete. It can however be expected that, as the surrounding fluid has a lower particle volume fraction than the concrete itself, α shall be higher than 1.

5.4. Simulations results

We first focus on the influence of the coupling between local rheological properties and local particle concentration variations due to gravity induced migration. We first choose $\alpha = 1$ as a first approximation. We plot in Fig. 7 the concentration profile along the beam for the coarsest particles (*i.e.* the ones that are the most prone to migration). It can be seen that the peak in aggregates volume fraction around 1 or 1.5 m can not be simulated. This holds true even if the value of α is varied.

We moreover plot in Fig. 8 the local aggregates concentration cartography at the end of the casting process. We see that both techniques predict the formation of the multilayer structure measured above. However, without any coupling, the settled aggregates are dragged along with the flow and the peak in settled aggregates concentration is located around 3 m from the pouring point. As the viscosity and yield stress of the material are not increasing with the local volume fraction, the zones where particles have migrated are still able to flow and advance in the beam. When coupling is implemented, the settled aggregates do not flow anymore and the peak is located around 1 or 1.5 m from the pouring point as measured in the experiment. The viscosity and yield stress of the material strongly increase in these zones as the volume fraction tends towards the maximal packing fraction. These zones can not flow and a deposition zone is formed in the first meter or meter and a half.

We now try to identify the best value for α . To do so, we fit α in order to reach the best agreement with the measured horizontal coarse aggregates concentration profile. A value of 1.45 is obtained. It is interesting to note that the value of the local apparent viscosity of the fluid surrounding the settling aggregates seems to be 30 % lower than the local apparent viscosity of the concrete. This suggests that the particles are settling in a material slightly more fluid than the concrete itself. The consequences of the gravity induced particle migration process are therefore not dictated by the behaviour of the concrete itself or the behaviour of its constitutive cement paste alone. Considering Eq. (5) and (6), a value of 1.45

for α suggests that the viscosity of the surrounding fluid corresponds to the viscosity of the concrete studied here but depleted of its coarsest particles. As a consequence, it could be expected that simultaneously decreasing the amount of coarse particles and increasing the amount of sand shall reduce the magnitude of gravity induced particle migration.

The numerical simulations give access to the shear rate and the coarse aggregates vertical profiles in the beam (Cf. Fig. 9). It is interesting to note that, contrarily to the case when no migration occurs in which the shear rate is maximal at the bottom wall interface, here the shear rate reaches its maximal value at the top of the deposition zone. This highly sheared zone has a lower apparent viscosity and is submitted to a fast particle depletion, which further reduces its viscosity, amplifying the gravity induced particle migration and turning it into a deposition process.

We now compare in Fig. 10 the results of the simulation with $\alpha = 1.45$ for the two casting rates studied here. We focus only on the coarsest particles (11-16 mm). We conclude that the simple numerical tool with only one fitted parameter used in this work is able to predict the influence of casting rate on gravity induced particle migration. It is moreover worth noting that increasing casting rate decreases the magnitude of particle heterogeneities. Although increasing casting velocity for shear thinning materials such as concrete shall reduce the suspending fluid viscosity, it also decreases the time during which particles are migrating. Both experimental and numerical results obtained in this work confirm the experimental results obtained in [4] on model materials, which suggest that it is the time effect which dominates and hence increasing casting velocity shall decrease the induced horizontal heterogeneity.

7. Conclusion

We have shown in this paper that gravity induced particle migration is mostly affecting the coarsest particles' concentration in concrete. It results in two types of heterogeneities in the final concrete element: the particle volume fraction decreases with the horizontal distance from the pouring point and a vertical multi-layer structure appears in the material.

We have moreover suggested from using numerical simulations that the viscosity of the fluid surrounding the migrating particles is of the same order as the viscosity of the equivalent concrete without the migrating particles. Finally, our experimental and numerical results confirm that high concrete casting rates reduce the magnitude of gravity induced particle migration.

ACKNOWLEDGEMENTS

The work is funded by the Danish Agency for Science Technology and Innovation (project 09-065049/FTP: Prediction of flow induced inhomogeneities in self compacting concrete).

The paper is partly based on the work performed in COIN – Concrete Innovation Centre (www.coinweb.no) – which is a Centre for Research based Innovation, initiated by the Research Council of Norway (RCN) in 2006.

REFERENCES

- [1] A.W. Saak, H. Jennings, S. Shah, New methodology for designing self-compacting concrete, *ACI Mater. J.* 98 (6) (2001) 429–439.
- [2] N. Roussel, A theoretical frame to study stability of fresh concrete, *Mater. Struct.* 39 (2006) 81–91.
- [3] L. Shen, L. Struble, D. Lange, Modeling dynamic segregation of self-consolidating concrete, *ACI Mater. J.* 106 (4) (2009) 375–380.

- 439 [4] J. Spangenberg, N. Roussel, J.H. Hattel, H. Stang, J. Skocek, M.R. Geiker, Flow induced
440 particle migration in fresh concrete: Theoretical frame, numerical simulations and
441 experimental results on model fluids, *Cement and Concrete Research* 42 (2012) 633–641.
- 442 [5] www.dti.dk/2783, (2012).
- 443 [6] www.dti.dk/2783,4 , (2012).
- 444 [7] C. Hu, F. de Larrard, T. Sedran, C. Boulay, F. Bosc, F. Deflorenne, Validation of
445 BTRHEOM, the new rheometer for soft-to-fluid concrete, *Materials and Structures*, Vol. 29,
446 No. 194, (1996) 620-631.
- 447 [8] Operating manual, the BML viscometer, the viscometer 4, Con Tec, 2000.
- 448 [9] G.H. Tattersall, S.J. Bloomer, Further development of the two-point test for workability
449 and extension of its range, *Magazine of Concrete Research*, 31, (1979) 202-210.
- 450 [10] C.F. Ferraris, L.E. Brower, editors (2001), Comparison of concrete rheometers:
451 International tests at LCPC (Nantes, France) in October 2000, National Institute of Standards
452 and Technology Interagency Report (NISTIR) 6819.
- 453 [11] C.F. Ferraris, L.E. Brower, editors (2004), Comparison of concrete rheometers:
454 International tests at MB (Cleveland OH, USA) in May 2003, National Institute of Standards
455 and Technology Interagency Report (NISTIR) 7154.
- 456 [12] H. Hafid, G. Ovarlez, F. Toussaint, P.H. Jezequel, N. Roussel, Estimating Measurement
457 Artifacts in Concrete Rheometers from MRI Measurement on Model Materials. In K.H.
458 Khayat and D. Feys (Eds.), *Design, Production, and Placement of Self-Consolidating*
459 *Concrete: Proceedings of SCC2010, Montreal, Canada, September 26-29, 2010, Volume 1 of*
460 *RILEM State of the Art Reports*, (2010) 127-137.
- 461 [13] N. Roussel, Rheology of fresh concrete: from measurements to predictions of
462 casting processes, *Materials and Structures* 40 (10) (2007) 1001–1012.

- 463 [14] N. Roussel, The LCPC BOX: a cheap and simple technique for yield stress
464 measurements of SCC, *Mat. Struct.* 40 (9) (2007) 889–896.
- 465 [15] T.L.H. Nguyen, N. Roussel, P. Coussot, Correlation between L-box test and rheological
466 parameters of an homogeneous yield stress fluid, *Cem. Concr. Res.* 36 (10) (2006)
467 1789–1796.
- 468 [16] N. Roussel, P. Coussot, “Fifty-cent rheometer” for yield stress measurements: from
469 slump to spreading flow, *J. Rheol.* 49 (3) (2005) 705–718.
- 470 [17] N. Roussel, Correlation between yield stress and slump: comparison between numerical
471 simulations and concrete rheometer results, *Mater. Struct.* 39 (4) (2006) 501–509.
- 472 [18] F. de Larrard, *Concrete Mixture Proportioning*, E & FN Spon, London, (1999).
- 473 [19] Eurocode 2, NF EN (1992).
- 474 [20] T. sedran, F. de Larrard, Optimization of Self Compacting Concrete thanks to Packing
475 Model, *RILEM Symposium on Self Compacting Concrete*, pp. 321-332, Stockholm, 13-15
476 September 1999.
- 477 [21] N. Roussel, T.L.H. Nguyen, O. Yazoghli, P. Coussot, Passing ability of fresh concrete: A
478 probabilistic approach, *Cement and Concrete Research* 39 (2009) 227–232
- 479 [22] F. Chevoir, F. Gaulard, N. Roussel, Flow and jamming of granular mixtures through
480 obstacles, *Europhysics Letters*, 79 (2007) 14001.
- 481 [23] N. Roussel, T.L.H. Nguyen, P. Coussot, General probabilistic approach of filtration
482 process, *Physical Review Letter*, 98(11) (2007) 114502.
- 483 [24] C.T. Tam, A.M.M Shein, K.C.G. Ong, C.Y. Chay, Modified J-ring approach for
484 assessing passing ability of SCC, *proceedings of SCC 2005*, published by Hanley Wood.
- 485 [25] I.Y.T. Ng, H.H.C Wong, A.K.H. Kwan, Passing ability and segregation stability of self-
486 consolidating concrete with different aggregate proportions, *Magazine of concrete research*,
487 volume 58(6), (2006) 447-457.

- 488 [26] J.H. Hattel, Fundamentals of Numerical Modelling of Casting Processes, Polyteknisk
489 Forlag, (2005)
- 490 [27] K.M. Kalland, A Navier-Stokes Solver for Single- and Two-Phase Flow, M. S. Thesis,
491 University of Oslo, (2008).
- 492 [28] J.E. Pilliod Jr, G.P Elbridge, Second-order accurate volume-of-fluid algorithms for
493 tracking material interfaces, Journal of Computational Physics, vol. 199, (2004) 465-502.
- 494 [29] G.H. Tattersall, P.G.F. Banfill, The Rheology of Fresh Concrete, Pitman, London, (1983).
- 495 [30] X. Chateau, G. Ovarlez, K.L. Trung, Homogenization approach to the behavior of
496 suspensions of noncolloidal particles in yield stress fluids, Journal of Rheology., vol. 52,
497 (2008) 489–506.
- 498 [31] F. Mahaut, S. Mokeddem, X. Chateau, N. Roussel, G. Ovarlez, Effect of coarse particle
499 volume fraction on the yield stress and thixotropy of cementitious materials, Cement and
500 Concrete Research, vol. 38, (2008) 1276-1285.
- 501 [32] I.M. Krieger, T.J. Dougherty, A mechanism for Non-Newtonian Flow in Suspensions of
502 Rigid Spheres, Transactions of the society of rheology, vol. 3, (1959) 137-152.

Components	kg/m3
Norcem Standard FA	278.3
Free water	178.2
Sand 0/8 mm	1035.7
Gravel 8/16 mm	847.4
Air entraining agent	1.81
High range water reducing admixture	2.56
Retardation agent	0.28
Viscosity agent	2.09
Density	2346

Table1. Mix proportions of the concrete studied in this paper.

Slump flow	T500	LCPC Box	Yield stress	Plastic viscosity
650mm	1.4 s	72 cm	40 ±20 Pa	100 ±20 Pa.s

Table 2. Fresh properties measurements

Figure(s)

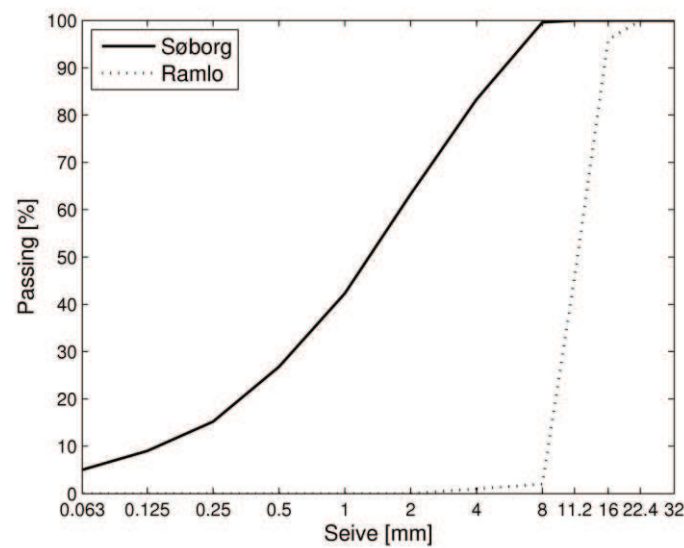


Figure 1. Particle size distribution for the sand and gravel used in this paper.

Figure(s)

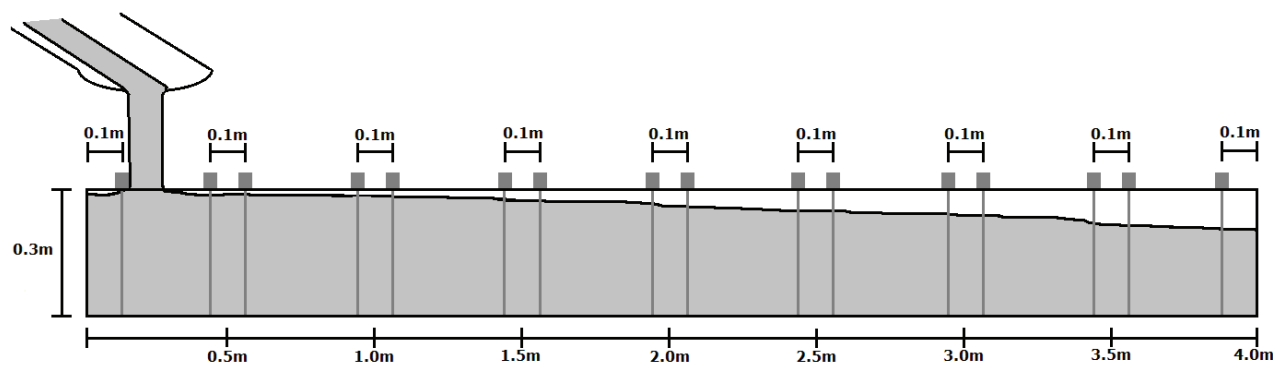


Figure 2. Beam geometry and casting.

Figure(s)

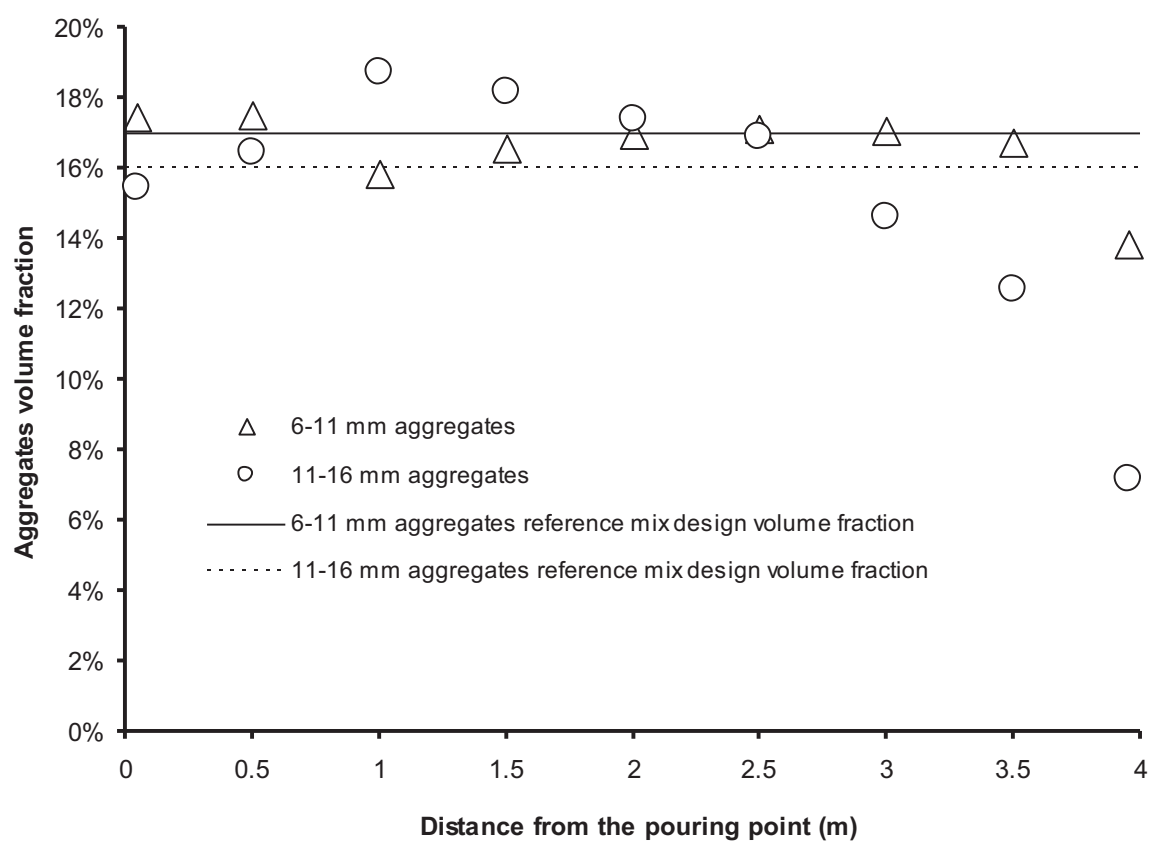


Figure 3. Aggregate volume fraction measured in fresh state by sampling, washing and sieving as a function of the distance from the pouring point.

Figure(s)

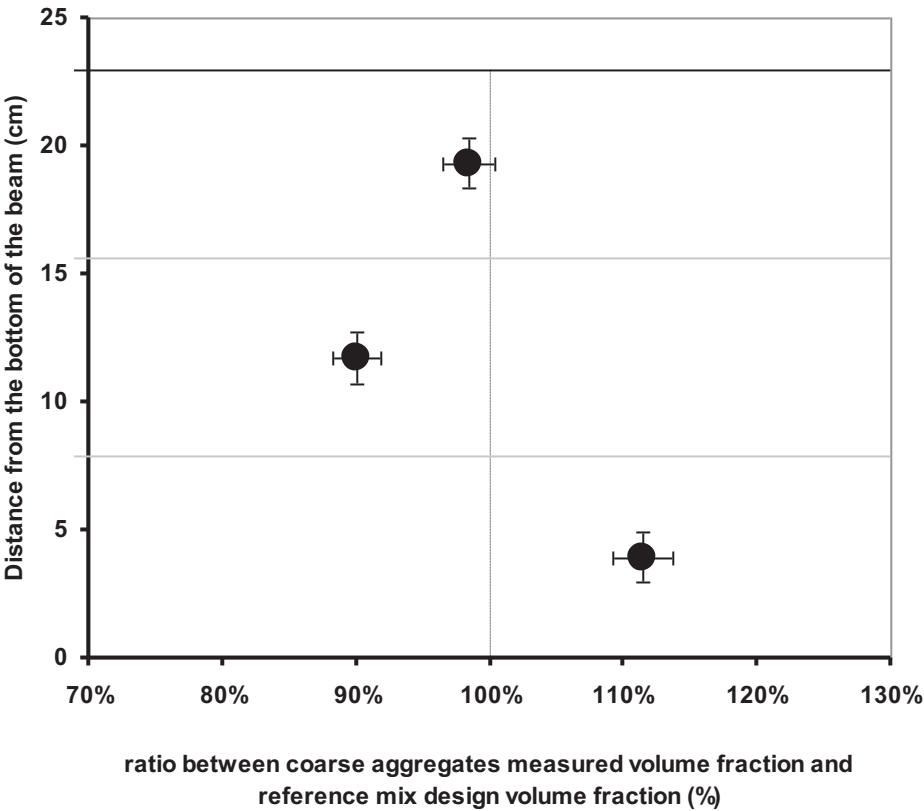


Figure 4. The layered structure induced by segregation in the first three meters of the beam. The dashed line corresponds to the reference mix design volume fraction.

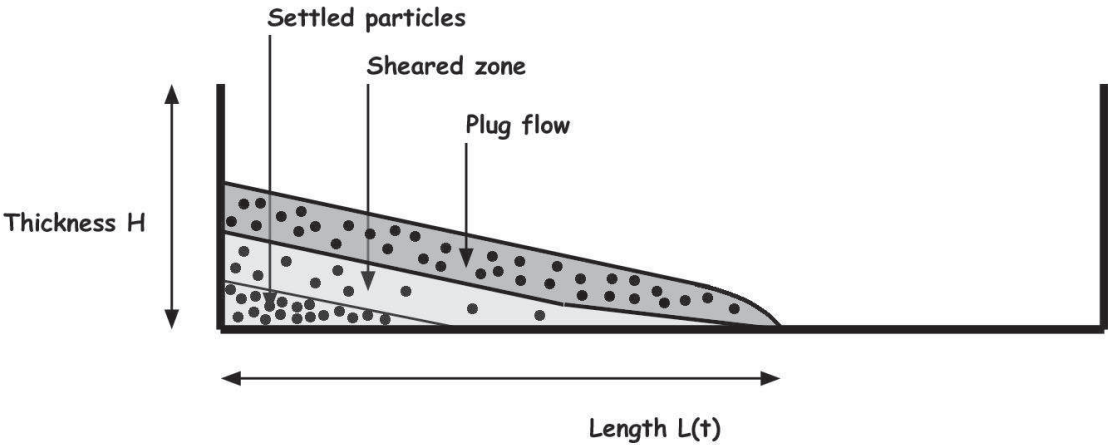


Figure 5. Multilayer structure in the transient flow regime

Figure(s)

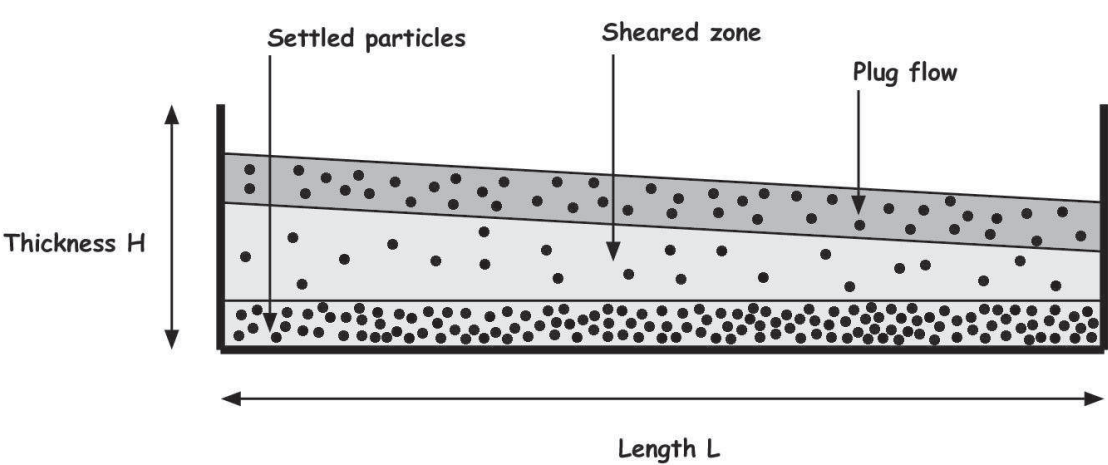


Figure 6. Multilayer structure in the steady flow regime

Figure(s)

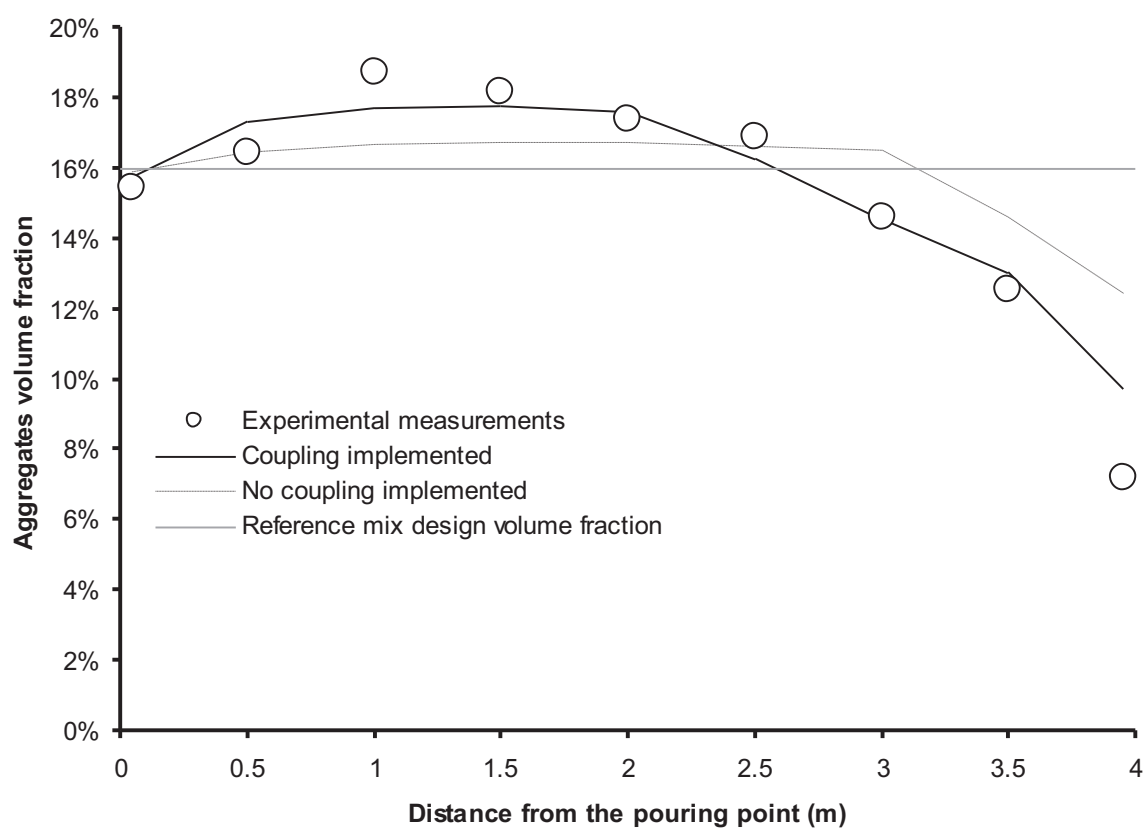


Figure 7. Aggregate volume fraction as a function of the distance from the pouring end of the beam for low casting speed. Experimental measurements and numerical prediction with or without coupling.

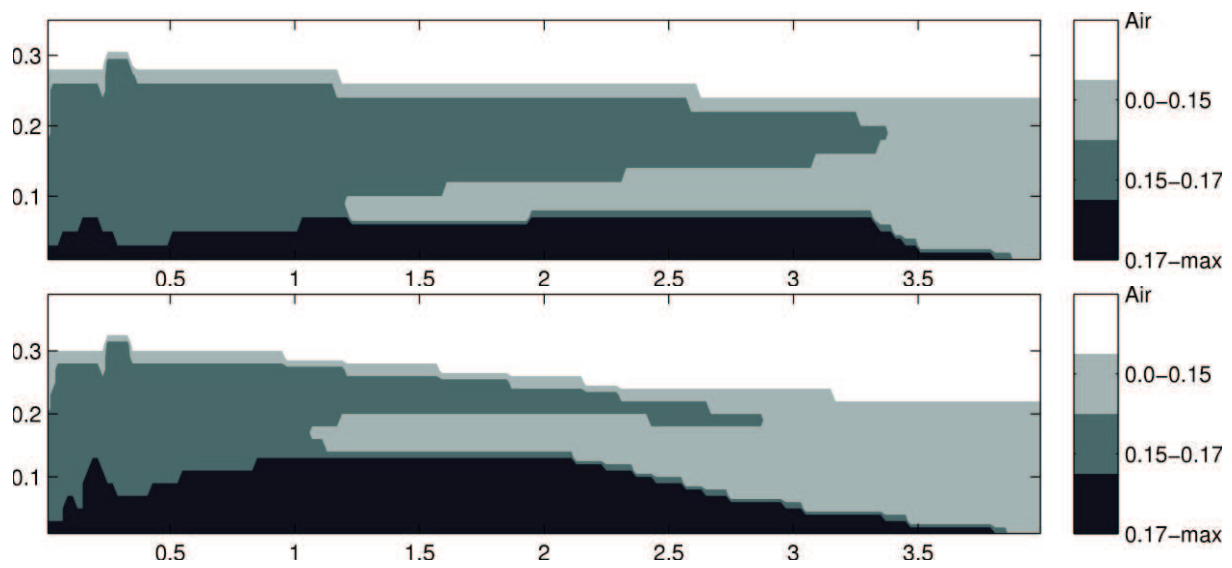


Figure 8. Cartography of local aggregates volume fraction. (top) simulations with no coupling implemented (bottom) simulations with coupling implemented. Vertical and horizontal distances are in (m).

Figure(s)

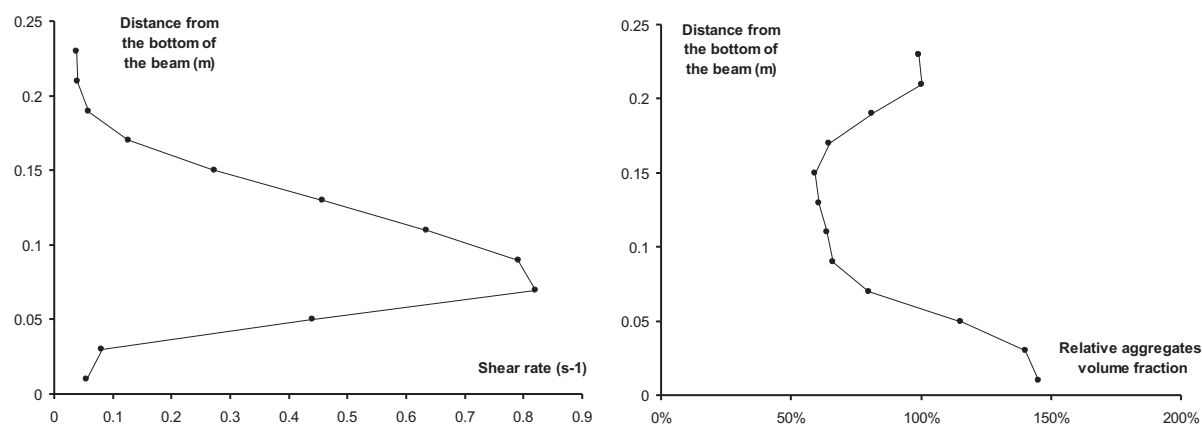


Figure 9. (left) Shear rate profile at the centre of the beam (right) Ratio between aggregates concentration and reference mix design concentration at the centre of the beam.

Figure(s)

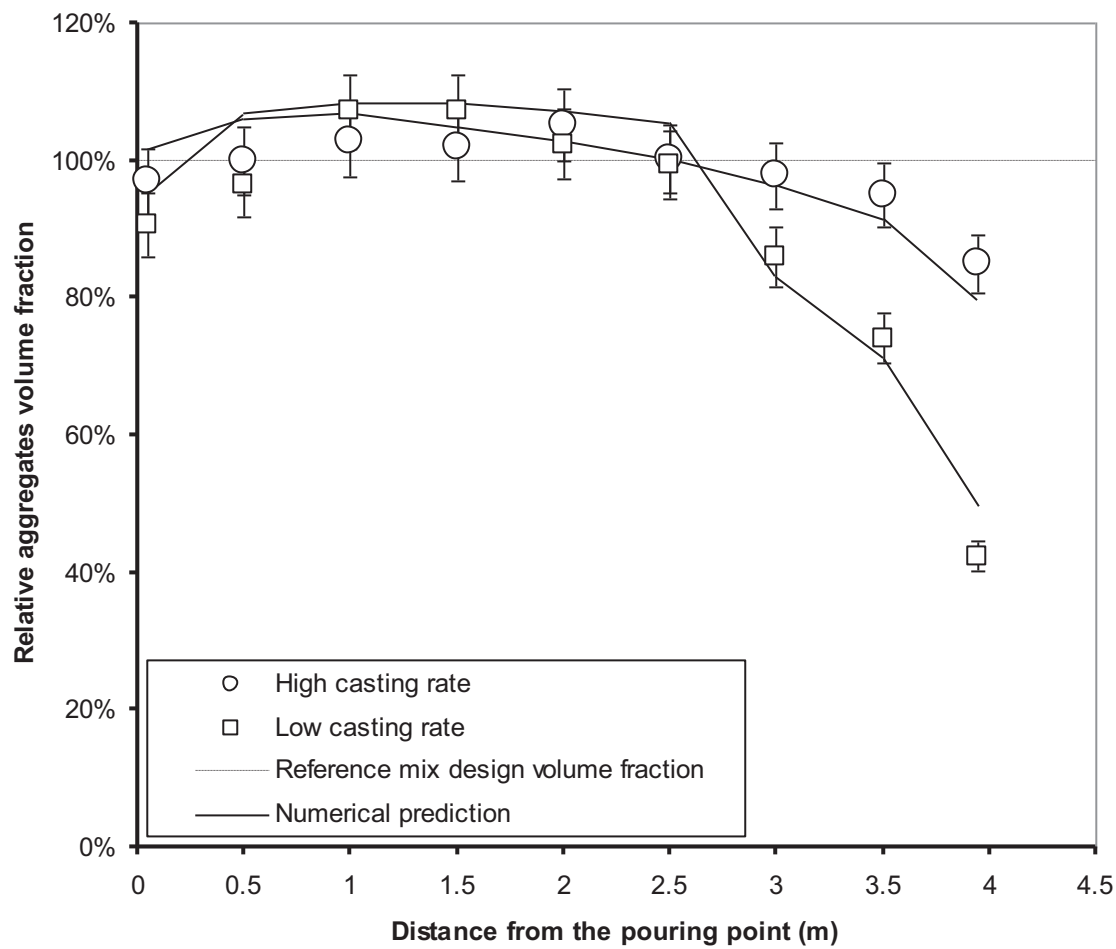


Figure 10. Relative aggregates volume fraction (*i.e.* ratio between local aggregates volume fraction and reference mix design volume fraction) as a function of the distance from the pouring end for the low and high casting rate.

D PAPER-IV

J. Spangenberg, C. Tutum, J. Hattel, N. Roussel, and M. Geiker (2011). Optimization of casting process parameters for homogeneous aggregate distribution in self-compacting concrete: A feasibility study. In *Evolutionary Computation (CEC), 2011 IEEE Congress on*, pp. 2163-2169.

Optimization of Casting Process Parameters for Homogeneous Aggregate Distribution in Self-Compacting Concrete: *A Feasibility Study*

Jon Spangenberg

Department of Mechanical Engineering
Technical University of Denmark
Lyngby, Denmark
josp@mek.dtu.dk

Cem Celal Tutum

Department of Mechanical Engineering
Technical University of Denmark
Lyngby, Denmark
cctu@mek.dtu.dk

Jesper Henri Hattel

Department of Mechanical Engineering
Technical University of Denmark
Lyngby, Denmark
jhat@mek.dtu.dk

Nicolas Roussel

Laboratoire Central des Ponts et Chaussées
Université Paris Est
Paris, France
Nicolas.Roussel@lcpc.fr

Mette Rica Geiker

Department of Civil Engineering
Technical University of Denmark
Lyngby, Denmark
mge@byg.dtu.dk

Department of Structural Engineering

Norwegian University of Science and Technology
Trondheim, Norway
mette.geiker@ntnu.no

Abstract—The use of self-compacting concrete (SCC) as a construction material has been getting more attention from the industry. Its application area varies from standard structural elements in bridges and skyscrapers to modern architecture having geometrical challenges. However, heterogeneities induced during the casting process may lead to variations of local mechanical properties and hence to a potential decrease in load carrying capacity of the structure. This paper presents a methodology for optimization of SCC casting aiming at having a homogeneous aggregate distribution; a beam has been used as geometric example. The aggregate distribution is predicted by a numerical flow model coupled with a user defined volume fraction subroutine. The process parameters in casting with SCC in general are horizontal and vertical positions, movement, as well as the size of the inlet, and the duration of the filling etc.,

however since this work is the initial feasibility study in this field, only three process parameters are considered. Despite the reduction in the number of process parameters, the complexity involved in the considered casting process results in a non trivial optimal design set.

Keywords—component; Self-Compacting Concrete, Flow simulation, Simulation based optimization, Genetic algorithms.

I. INTRODUCTION

Structural concrete elements compose a large amount in all structures worldwide. In addition, almost one tenth of them are in Europe carried out with SCC and the number is increasing every year. SCC consists of aggregates bound by cement paste

and differs from original concrete by an addition of a special form of super-plasticizer which increases the fluidity of the fresh concrete. The higher fluidity allows SCC to fill out the formwork under its own weight; thus SCC does not require external compaction (e.g. vibration) as conventional concrete. However, the drawback of using SCC is also its higher fluidity which decreases its segregation resistance, in other words an inhomogeneous aggregate distribution may be induced during casting. This situation may lead to variations of local mechanical properties and consequently a potential decrease in the load carrying capacity of the structure. For potential use in design and planning, a numerical simulation approach to predict the distribution of aggregates, which is desired to be homogeneous, was demonstrated in [1]. Previously, numerical simulations were used to identify the minimum amount of fluidity needed to ensure proper filling [2, 3]. Furthermore, Thrane et al. [4] illustrated how numerical simulations can be used to detect free surface, dead zones and particle paths.

Literature shows that no coupling between optimization and numerical simulations of SCC flow have been carried out before. In addition, only a limited work is published for optimization of manufacturing processes in general. One limiting factor is computational power which inhibits running multiple simulations with high accuracy within reasonable time. Another is that only a limited number of simulation software packages are coupled with optimization modules. These limitations eventually determine what is in fact possible today and hence determine what the “state-of-the-art” is. Some examples of exploiting numerical simulation together with numerical optimization have resulted in, for instance, (i) reducing the residual stresses in a welded mechanical component together with a simultaneous improvement of the production efficiency (e.g. higher welding speed) in case of friction stir welding [5-6], (ii) increasing the casting yield via riser optimization meanwhile reducing the porosity in a gravity sand-cast steel part [7] or (iii) optimizing the chemistry of bulk metallic glasses for improved thermal stability [8]. These are some of the very limited number of already analyzed examples among many potential real world optimization problems in manufacturing.

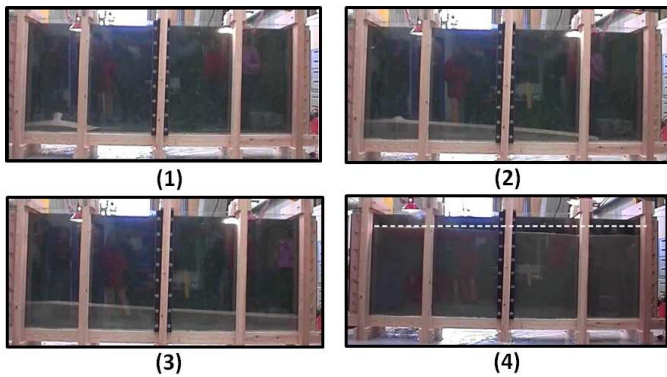


Figure 1: Example of form filling with SCC, form [15]

The objective of this paper is to optimize process parameters in SCC casting (see Fig. 1) to minimize dynamic segregation, in other words to obtain the most uniform distribution of aggregates. More specifically, the choices of

mass rate, inlet size and inlet position are sought to achieve the goal mentioned above using an evolutionary optimization algorithm, i.e. a single-objective genetic algorithm (SOGA). First, the numerical flow model is presented along with a brief overview of the governing equations and the assumptions needed to simulate the segregation phenomena during casting of SCC. Following this, the optimization procedure is given in more detail together with some aspects of process integration. Next, the results of the optimization study are presented and a discussion on sensitivity and robustness of the optimal solution with respect to operation conditions is provided. Finally, the conclusion gives guidelines and future perspectives in this rapidly growing application field.

II. NUMERICAL MODEL

A. Theory and Governing Equations

Dynamic segregation during casting of SCC is a highly non-linear problem which is governed by several complex physical phenomena among which the numerical model presented in the present work takes the following three major effects into account:

1. The global non-Newtonian flow of SCC.
2. The interaction between matrix¹ and the large aggregates.
3. The interaction between the aggregates.

The global non-Newtonian flow is captured by solving the continuity equation given in Eqn. (1) together with the momentum equations given in Eqn. (2).

$$\frac{\partial \rho}{\partial t} + \text{div}(\rho u) = 0 \quad (1)$$

$$\frac{\partial}{\partial t}(\rho u) + \text{div}(\rho u u) = \text{div}(\mu \text{grad } u) - \frac{\partial p}{\partial x} + B_x + V_x \quad (2)$$

where ρ is the density of the SCC, u is the velocity, t is the time, p is the pressure, B_x is the x-direction body force per unit volume, and V_x stands for the viscous terms that are in addition to those expressed by $\text{div}(\mu \text{grad } u)$. The material model used when solving the two equations is a Bingham material model which is an acceptable rheological model to describe the non-Newtonian flow behavior of SCC. Mathematically the Bingham material model is described by the expression in Eqn. (3) and (4).

$$\dot{\gamma} = 0 \quad \text{for} \quad \tau < \tau_0 \quad (3)$$

$$\tau = \tau_0 + \mu_{pl} \dot{\gamma} \quad \text{for} \quad \tau \geq \tau_0 \quad (4)$$

where $\dot{\gamma}$ is the shear strain rate, τ is the shear stress, τ_0 is the yield shear stress, and μ_{pl} is the plastic viscosity. Fluids simulated by the Bingham material model are assumed to start to move when the yield stress is exceeded. As soon as this takes place, the fluid flows according to the plastic viscosity and it stops again when the yield stress is no longer exceeded. In Fig. 2 the Bingham material model is illustrated.

¹ Matrix = cement paste and aggregates which are less than 8mm (in this case).

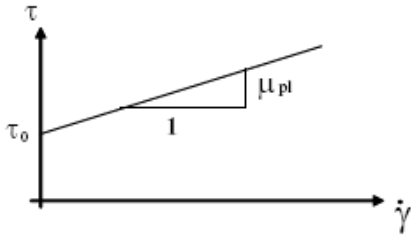


Figure 2: Bingham material model

The interaction between the matrix and the large aggregates is captured by solving the expression for the settling velocity of a spherical particle (aggregate) in a non-Newtonian fluid (SCC) given in Eqn. (5).

$$u^s = \frac{d^2 g (\rho_a - \rho)}{18 \mu_{app} C} \quad (5)$$

where d is the diameter of the aggregate, g is the gravity, ρ_a is the density of the aggregate, μ_{app} is the apparent viscosity, and C is the drag force multiplier. The settling velocity describes the relative velocity between the aggregate and the SCC and it is a result of the force equilibrium between the gravity, buoyancy and Stokes drag force. The coupling between the aggregate and the SCC lies within the apparent viscosity, which is obtained when solving the global flow. The coupling is a one way momentum coupling, which means that the aggregate 'feels' the SCC but not vice versa. The drag force multiplier is included in Eqn. (5) in order to take into account that locally the aggregate experiences a viscosity which is lower than the viscosity of the global flow; in this case 10 times lower. The reason for selecting this value is that SCC has a plastic viscosity and a yield stress of the order 50-100 Pa.s and 50-100 Pa, respectively, while the same properties for the matrix are of the order 5-10 Pa.s and 5-10 Pa.

The interaction between the aggregates is more qualitatively taken into account in this numerical model. It is known that the interaction between aggregates prevents them from settling. However, exactly how much it prevents varies from mixture to mixture. Therefore, it is assumed for this investigation that the aggregate interaction effect changes the drag force multiplier from being 0.1, due to the local/global viscosity effect, to 0.5.

B. Implementation of Model in Flow3D

The global non-Newtonian flow of SCC is calculated by the commercial Computational Fluid Dynamics (CFD) software Flow3D [9]. The software solves Eqn. (1) and (2) by the use of the Finite Volume Method (FVM) coupled with the Volume of Fluid (VOF) method. In addition, the Generalized Minimum Residual Solver (GMRES) is used to solve the pressure and the velocities implicitly. Furthermore, a user defined subroutine is developed in Flow3D to capture the interaction between the aggregates and the SCC. The subroutine evaluates a volume fraction scalar and the settling of this volume fraction scalar is derived based on a mass change consideration on a finite volume grid, see Eqn. (6).

$$\frac{\partial M_i}{\partial t} = \dot{M}_{in} - \dot{M}_{out} \quad (6)$$

where M_i is the mass of the aggregates in the evaluated cell, \dot{M}_{in} and \dot{M}_{out} are the mass fluxes in and out of the evaluated cell, respectively. By the use of the explicit Euler scheme it is possible to derive Eqn. (7) which describes the volume fraction of the aggregates in the new time step. Note that Eqn. (7) is valid for the two dimensional case on a structured grid.

$$\phi_i^{\Delta t + t} = \phi_i^t \left(1 - u_i^s \frac{\Delta t}{\Delta y} \right) + \phi_{i+1}^t u_{i+1}^s \frac{\Delta t}{\Delta y} \frac{VOF_{i+1}}{VOF_i} \quad (7)$$

VOF is the volume of fluid, ϕ is the volume fraction of aggregates and $\Delta x/\Delta y$ are the lengths of the control volume in each direction. This numerical technique was validated in [10] where a good correlation between experimental results of a SCC like suspension (carbopol and glass beads) and the numerical predictions were found.

The investigation is carried out on a 0.5 m high and 3 m long beam and is simulated in these two dimensions, since it speeds up the calculation and still gives the same trends as observed for a three dimensional simulation. The chosen 2D assumption also implies the reinforcement bars within the beam basically cannot be modeled. The length and the height of the control volumes are 0.01 m which gives a total of 15000 control volumes. The modeled boundary conditions are wall (zero velocity) at the left, right and bottom boundary (see Fig. 3). The symmetry boundary condition is used on the front, back and top boundary. The symmetry boundary is used at the top of the beam to ensure that a segregation layer is not created.

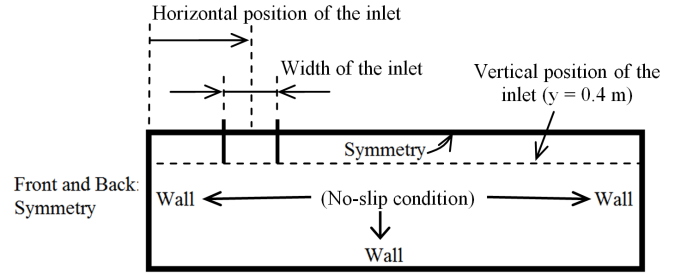


Figure 3: Boundary conditions

The modeled plastic viscosity and yield stress for the Bingham material model are 50 Pa.s and 50 Pa, respectively. The density of the SCC is 2200 kg/m³ and the density of the aggregates is 2700 kg/m³. The aggregates considered for the dynamic segregation calculation correspond to the 25% coarsest particles in the material. The volume fraction of these particles is estimated to be in the order of 15-20% in practice and can be associated to a characteristic average diameter of 14 mm. By doing so, it is assumed that the 75% finest aggregate particles are sufficiently small to be stable and do not segregate during flow.

The vertical position of the inlet is 0.4 m from the bottom of the mould in all simulations, while its horizontal position is one of the three process parameters, which is varied for the optimization investigation. The horizontal position of the inlet is varied between 0.1 m and 1.5 m (which is the middle of the beam). The second varied process parameter is the inlet size

and it is varied between 0.05 m and 0.08 m, which is an reasonable interval for a casting of a beam with the before mentioned dimensions. The final process parameter is the mass rate and it is varied between 1.0 kg/s and 1.66 kg/s, which correspond to a filling duration between 20 s and 35 s. These process parameters are only a few of the parameters which potentially could be optimized when casting with SCC. Despite, the limited process parameters, an optimization is still required, since conflicting physical behavior takes place when varying each of the considered process parameters and hence hinders the solution to be predicted on beforehand. E.g., the conflicting physical behavior when varying the mass rate is that a high mass rate generates a low apparent viscosity and thereby a high settling velocity in a large region of the flow domain, however the duration in which the settling takes place is short as compared to when using a low mass rate. Analogous, a low mass rate generates a high apparent viscosity and thereby a low settling velocity in a small region of the flow domain, however the duration in which the settling takes place is long as compared to when using a high mass rate.

When optimizing SCC flows by numerical simulation within a reasonable time frame some compromises regarding grid and/or maximum number of iterations for the solvers are inevitable, if a super computer is not used. In this study the maximum number of iterations are compromised, while the number of grid point reflects the amount used when a very accurate simulation is carried out. The maximum number of iterations is decreased from 9999 (normally used by author) to 100 and by doing so some accuracy is lost. Therefore, it is of great importance to carry out a test case where the accuracy loss is measured between the simulations with the high and low maximum number of iterations. In this study an accuracy loss of approximately 1% was observed. However, this accuracy loss should be weighed against the purpose of the simulation as well as the decreased calculation time. So since this study is a feasibility study and its primary target is to capture trends rather than full accuracy, it was chosen to accept the accuracy loss. In addition, it should be mentioned that this choice decreased the calculation time from 4 hours to 1-1.5 hours depending on the mass rate used for the particular simulation.

III. OPTIMIZATION METHODOLOGY

A. Optimization Algorithm

In this paper an evolutionary single objective genetic algorithm (SOGA) is applied to optimize the aggregate distribution while casting with SCC in order to get a uniform distribution of aggregates, in mathematical terms as to minimize the standard deviation of the volume fraction scalar at the end of the process.

$$\begin{aligned} \text{Minimize: } & \sqrt{\left(\frac{1}{n_{cv}-1}\right) \sum_{i=1}^{n_{cv}} (v_{frac,i} - \bar{v}_{frac})^2} \\ & 1.00 \leq \dot{m} \leq 1.66 \left(\frac{kg}{s}\right) \\ & 0.1 \leq x_{pos} \leq 1.5 (m) \\ & 0.05 \leq w \leq 0.08 (m) \end{aligned} \quad (8)$$

Evolutionary algorithms (EAs) are non-deterministic (stochastic) methods that mimic evolutionary principles, e.g. natural selection and the survival of the fittest, to constitute their optimization strategy. They work with a set of solutions (population) instead of a single point as in traditional (classical) methods and this gives an opportunity to attack a complex problem (discontinuous, noisy, multi-modal, etc.) in different directions allowing the algorithm to explore as well as exploit the search space. This capability gives an advantage for having a more robust search strategy compared to traditional mathematical programming algorithms. Since they do not need any gradient information, they are very suitable for black-box (e.g. commercial software) optimization applications, as in this specific case as well, i.e. coupling with Flow3D.

SOGA is a generic single objective genetic algorithm (GA) which uses binary encoding for the representation of the design variables. The initial population, represented by binary strings of different lengths for each design variable, is composed of randomly distributed solutions in the design space. The algorithm is based on several genetic operators: binary tournament selection, single-point crossover and uniform mutation. Moreover it is an elitist algorithm which means that the best solutions found so far are preserved to accelerate convergence towards true or near optimum while still having explorative search to avoid premature convergence. Binary tournament selection implemented in SOGA is composed of two tournaments in which every individual compete only once in each. The other genetic operators are implemented in a standard way [11]. SOGA has actually been converted from mNSGA-II (MATLAB implementation of NSGA-II [12] that is a similar replication of the original algorithm [13]) which has been successfully applied elsewhere [14]. Therefore, non-dominated sorting and crowding distance operators together with simulated binary crossover and polynomial mutation operators (built for real coded GAs) have been removed.

B. Optimization Procedure and Process Integration

The optimization procedure (see Fig. 4), which includes a process integration of the Flow3D software and the optimization algorithm SOGA was handled by using MATLAB. The optimization cycle was initiated by creating an initial population of 20 randomly distributed set of design variables, i.e. the horizontal position and the size of the inlet as well as the mass rate. The total number of generations was 10. The probabilities for the single point crossover and mutation operators were, 0.65 and $1/l_i$ (l_i : total string length). The parametric input file for simulating the SCC flow was executed in batch mode. Integration of Flow3D and the optimization algorithm was done in MATLAB environment.

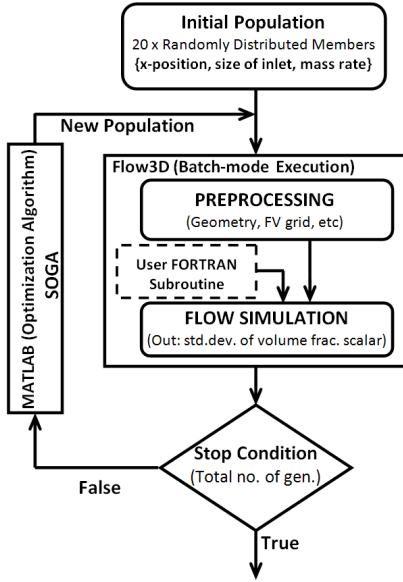


Figure 4: Flowchart of the optimization problem

The design variables were updated by the optimization algorithm (i.e. SOGA) and were provided as an input for the flow simulation. Then the volume fraction scalar in each control volume was saved at the end of the simulation. The standard deviation of the volume fraction was afterwards calculated by the optimization algorithm and used as the fitness of the design set to be minimized. This optimization cycle ran until the stopping criterion, i.e. the total number of generations, was reached.

IV. RESULTS AND DISCUSSIONS

The results obtained from the optimization study are seen in Fig. 5. The figure shows the generations as function of the standard deviation (fitness) for the best individual and for the average of all individuals.

Fig. 5 shows that the algorithm found an improved solution in the third generation and that the best solution was found in the fifth generation. Furthermore, Fig. 5 shows that if a casting is carried out corresponding to the average of the first generation an improvement of approximately 11% can be obtained. In addition, the optimization data shows that if a casting is carried with process parameters similar to the worst solution an improvement of approximately 20% can be obtained.

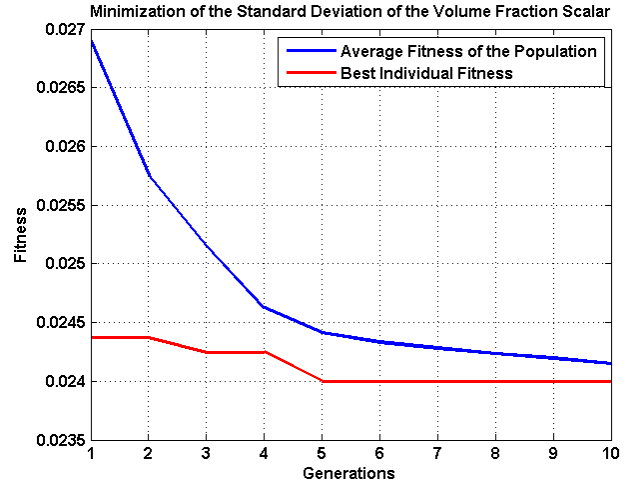


Figure 5: Generations as function of the standard deviation for best individual and average individuals.

The optimum process parameters obtained for the actual case were; a horizontal position of 0.88 m, an inlet size of 0.074 m, and a mass rate of 1.66 kg/s. This indicates that even tough conflicting physical behavior takes place when varying the mass rate; the optimization clearly states that the highest possible mass rate is preferable for the given problem. Regarding the inlet size, the optimization data shows that by increasing the inlet size results in a better solution, if the same horizontal position and mass rate is used. However, the improvement is negligible as compared to the improvement of the solution when increasing the mass rate. Finally, the optimization shows that a more homogeneously aggregate distribution is obtained when casting at 0.88 m as compared to casting in the middle. In Fig 6, the volume fraction is shown in the last time step of the simulation for both the optimal solution (now referred to as beam_{opt}) and for the simulation with the optimum parameters for inlet size and mass rate, but with a horizontal inlet position in the middle of the beam (now referred to as $\text{beam}_{\text{middle}}$). Note, that the maximum contour limit in Fig. 6 is 0.16 which corresponds to the homogeneous value in order to enhance the areas where aggregates are immigrated from.

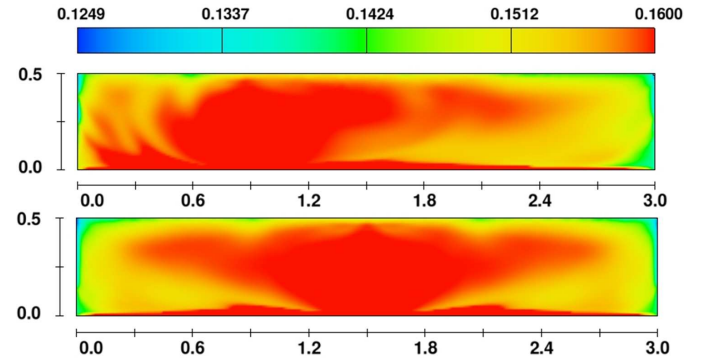


Figure 6: Volume fraction of coarse aggregates in the last step for beam_{opt} and $\text{beam}_{\text{middle}}$.

The improvement by using beam_{opt} as compared to $\text{beam}_{\text{middle}}$ is approximately 3%, but this improvement is difficult to detect in Fig. 6. However, Fig. 6 shows the important issue which is that $\text{beam}_{\text{middle}}$ obtains a zone where the aggregates are immigrated from on both sides of the inlet, while beam_{opt} primarily obtains such zone on the side of the inlet where the longest flow distance to the end of the mould is present. This issue opens the discussion about if the standard deviation is a satisfactory criterion to evaluate the casting process of the beam, e.g. it could be that the size of the immigrated zone is equally or more important for the beam as compared to the standard deviation of the volume fraction. In such case, where conflicting objectives are present, a multi-objective optimization problem formulation and hence a relevant efficient algorithm would be of interest to use. Nevertheless in this investigation the evaluation is carried out based on the standard deviation of the volume fraction and the optimization showed that from that perspective it is preferable to have a flow distance of 0.88 m and 2.12 m as compared to two flow distances of 1.5 m. In order to investigate this further it was chosen to carry out another optimization where the inlets horizontal position and the inlet size was varied in the same interval as for the previous study, while the mass rate now was fixed to its maximum value of 1.66 kg/s. In Fig. 7 the standard deviation is plotted for all the combinations calculated in the study. Note that 10 generation with 20 individuals is again used.

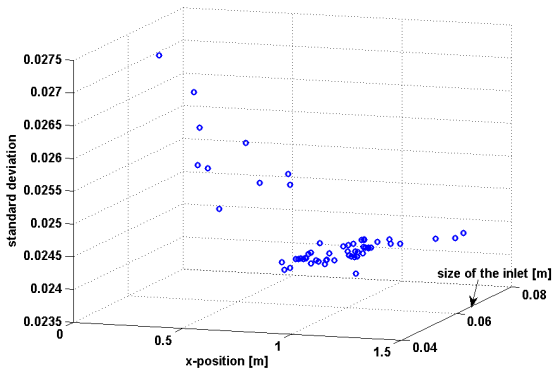


Figure 7: Standard deviation as function of horizontal position and inlet size.

The new optimization data shows that it is possible to obtain a solution which is slightly better than the one found in the first optimization study. The new beam_{opt} is approximately 4% better than $\text{beam}_{\text{middle}}$. The reason why this solution is not found in the first optimization study is probably due the limited number of individuals in the generations. This indicates that if an optimization study of a more industrial SCC casting is carried out and it is not only trends which are the objective as in this feasibility study, it would be necessary to use more than 20 individuals and 10 generations. This statement is especially valid if more than three process parameters are investigated.

Fig. 7 illustrates a very important topic within optimization of SCC castings, which is that a robust solution is very important. In Fig. 7 it is seen that the solution does not change critically if the horizontal position is 0.91 m or 0.81 m instead

of 0.88 m. On the contrary if a small deviation from the optimal process parameter changes the solution critically it is preferable to use a process parameter which is more robust. The robustness issue is especially important in optimization of SCC castings, since it is a process carried out by humans. Meaning, that it is a human being which for instance holds the hose from where the SCC flows into the mould. Therefore, it is of no interest to find an optimal solution which is ruined if the hose is offset in the horizontal position by 0.91 m instead of 0.88 m.

V. CONCLUSION

In this paper it was shown that evolutionary algorithms can be a very useful tool for optimizing of casting process parameters for SCC. For the actual case, this feasibility study showed that within the considered interval of the three investigated process parameters, the most homogenous aggregate distribution is obtained when using the maximum mass rate. In addition, the trend regarding the size of the inlet is that a small improvement of the solution is obtained if it is increased and the two other process parameters are fixed. Finally, the study showed that if the position of the inlet is fixed during the entire casting process, a more homogenous aggregate distribution is obtained if its horizontal position is 0.88 m from either end of the beam instead of in the middle of the beam.

The potential in optimization of SCC properties via evolutionary algorithms is extensive; it could be considered used both as a design and a planning tool. One of the future challenges would be to investigate more process parameters (as compared to 3 presented in this particular work), e.g. varying the horizontal position of the inlet during the casting process and the time spent at each of these horizontal positions. Another perspective would be to introduce an additional objective which could be the minimization of the size of the region from where the particles are immigrated. Adding second or third objective into the optimization problem in general can provide a deeper understanding of the process while having more criteria to evaluate each design, and moreover this would eventually serve for vital knowledge discovery. Finally it should be mentioned that it would also be interesting first to optimize the mechanical properties of the beam (via integrated modeling approach in which a flow simulation, predicting the aggregate distribution, is coupled with a solid mechanics model relating this distribution to local mechanical properties) thus leading to a desired aggregate distribution and then use this as the objective for the SCC casting optimization process instead of having a homogenous distribution as objective.

ACKNOWLEDGMENT

The work is funded by the Danish Agency for Science Technology and Innovation (project 09-065049/FTP: Prediction of flow induced inhomogeneities in self compacting concrete).

REFERENCES

- [1] J. Spangenberg, N. Roussel, J.H. Hattel, J. Thorborg, M.R. Geiker, H. Stang, and J. Skocek, "Prediction of the impact of flow induced inhomogeneities in self compacting concrete (sc),," Proceedings of the 6th international RILEM symposium on SCC, vol. 1, pp. 209–215, 2010.

- [2] N. Roussel, M.R. Geiker, F. Dufour, L.N. Thrane, P. Szabo, "Computational modeling of concrete flow: general overview, *Cement and Concrete Research*, vol. 37(9), pp. 1298-1307, 2007.
- [3] N. Roussel, L. D'Aloia Staquet, L. Schwarzenruber, R. Le Roy, and F. Toutlemonde, "SCC casting prediction for the realisation of prototype VHPC precast composite beams," *Materials and Structures*, vol. 40(9), pp. 271-350, 2007.
- [4] L. N. Thrane, P. Szabo, M. R. Geiker, M. Glavind, and H. Stang, "Simulation and verification of flow in SCC test methods," *Proc. Of 4th int. RILEM Symp on SCC*, 2005.
- [5] C.C. Tutum, and J.H. Hattel "Optimisation of process parameters in friction stir welding based on residual stress analysis: a feasibility study," *Journal of Science and Technology of Welding and Joining*, vol. 15(5), pp. 369-377, 2010.
- [6] C.C. Tutum, and J.H. Hattel, "A multi-objective optimization application in friction stir welding: Considering thermo-mechanical aspects," *IEEE Congress on Evolutionary Computation (IEEE CEC 2010)*, pp. 427-437.
- [7] P. Kotas, C.C. Tutum, O. Snajdrova, J. Thorborg, and J.H. Hattel, "A casting yield optimization case study: Forging ram," *International Journal of Metal Casting*, vol. 4(4), pp. 61-76, 2010.
- [8] G.S. Dulikravich, V.K. Sikka, and G. Muralidharan, "Optimizing chemistry of bulk metallic glasses for improved thermal stability," *Modelling and Simulation in Materials Science and Engineering*, vol. 16(7), pp. 1-19, 2008.
- [9] Flow3d version 8.1, user manual 1, 2004.
- [10] J. Spangenberg, N. Roussel, J.H. Hattel, M.R. Geiker, "Dynamic segregation during self-compacting concrete (scc) casting: Theoretical frame and experimental results on model fluids," unpublished.
- [11] Deb, K., *Multi-Objective Optimization using Evolutionary Algorithms*. John Wiley and Sons, Ltd, Chichester, UK (2001).
- [12] Tutum, C. C., *Optimization of thermomechanical conditions in friction stir welding*. PhD thesis, Technical University of Denmark, Kgs. Lyngby, Denmark, ISBN:978-87-89502-89-2 (2009).
- [13] Deb, K., Agarwal, S., Pratap, A., Meyarivan, T.: A fast and elitist non-dominated sorting genetic algorithm for multi-objective optimization: NSGA-II. *IEEE Transactions on Evolutionary Computation*, vol. 6, pp. 182-197 (2002).
- [14] C. C. Tutum, K. Deb and J. H. Hattel: 'Hybrid Search for Faster Production and Safer Process Conditions in Friction Stir Welding', *Proc. 8th Simulated Evolution and Learning (SEAL)*, Indian Institute of Technology Kanpur, India, December 2010, *Springer-Verlag, Lecture Note in Computer Science*, **6457**, 603-612.
- [15] L.N. Thrane, "Form Filling with Self-Compacting Concrete," Ph.D. Thesis, Technical University of Denmark, ISBN 97-8877-8772-473, 2007

F TECHNICAL REPORT-I

J. Spangenberg, and J. H. Hattel (2012). A CFD Solver for Simulation of Flow of Self Compacting Concrete.

Technical Report - I

A CFD Solver for Simulation of Flow of Self Compacting Concrete

Jon Spangenberg and Jesper H. Hattel

**Department of Mechanical Engineering
Technical University of Denmark
March, 2012**

Copyright (c), Jon Spangenberg, 2012
Department of Mechanical Engineering
Technical University of Denmark

Table of Contents

1	Introduction	1
2	Governing Equations	3
2.1	Mass Conservation	3
2.2	Momentum Conservation	4
2.3	Pressure Equation	5
3	Discretization	7
3.1	Pressure Equation	7
3.2	Velocity Equations	11
4	Boundary Conditions	13
4.1	Pressure	13
4.2	Velocity	13
	Bibliography	15

Chapter 1

Introduction

In this technical report it is described how to develop a two dimensional non-Newtonian Computational Fluid Dynamics (CFD) solver for an incompressible fluid, such as Self Compacting Concrete (SCC). The CFD solver is solving the mass conservation (continuity) equation together with the momentum equations with the use of the Finite Volume Method (FVM) and the staggered grid formulation.

The technical report is divided into three parts. The first part gives an overview of the governing equations, while the second part describes the discretization of them. Finally, the third part presents the wall boundary condition.

The content of this technical report is based on [1], [2], and [3].

Chapter 2

Governing Equations

The flow of SCC is non-Newtonian and in order to describe this, one has to consider the mass conservation equation also known as the continuity equation as well as the momentum conservation equations. In the following three sections, these governing equations are presented and processed in order to obtain the final equations for the velocities and pressure, which are actually solved by the CFD-solver.

2.1 Mass Conservation

Conservation of mass means that the mass of a considered volume does not change in time. Mathematically that can be written as:

$$\frac{d}{dt} \int_{\Omega} \rho \, d\Omega = 0 \quad (2.1)$$

Where t is the time, Ω is the volume, and ρ is the density. Applying Reynolds Transport Theorem on Eqn. (2.1) yields:

$$\int_{\Omega} \left\{ \frac{\partial \rho}{\partial t} + \frac{\partial}{\partial x_j} (\rho u_j) \right\} d\Omega = 0 \quad (2.2)$$

Where x_j is the spatial component vector, j is the notation denoting the direction, and u_j is the velocity vector. Eqn. (2.2) is the integral form of the mass conservation. However, the volume size is arbitrary, therefore, the law must also hold point wise in the fluid. Consequently, this leads to the mass conservation on differential form:

$$\frac{\partial \rho}{\partial t} + \frac{\partial}{\partial x_j} (\rho u_j) = 0 \quad (2.3)$$

Eqn. (2.3) can also be written as:

$$\frac{\partial \rho}{\partial t} + u_j \frac{\partial \rho}{\partial x_j} + \rho \frac{\partial u_j}{\partial x_j} = 0 \quad (2.4)$$

In literature it is shown that SCC can be treated as an incompressible fluid, cf. [4] and [5]. This assumption is also applied for this CFD solver, meaning that the density of the fluid does not change in space and time. The assumption makes Eqn. (2.4) simplify into the divergence of the velocities:

$$\frac{\partial u_j}{\partial x_j} = 0 \quad (2.5)$$

Eqn. (2.5) is used to obtain the equations for the velocities in section 2.2 by simplifying the momentum conservation equations and it is also used when deriving an equation for the pressure in section 2.3.

2.2 Momentum Conservation

Conservation of momentum states that the rate of change of fluid momentum must be balanced by the total force applied to the fluid. The total force is the sum of the contributions from the pressure, the viscous stresses and the gravitational force. The momentum conservation equations express a force equilibrium:

$$\frac{d}{dt} \int_{\Omega} \rho u_i d\Omega = \int_S T_{ij} n_j dS + \int_{\Omega} S_i d\Omega \quad (2.6)$$

Where S is the surface, T_{ij} is the stress tensor, and S_i is the gravitational force vector ($S_i = [0, 0, -\rho g]$). The notation i denotes a scalar equation for each of the three dimensions. The equations express conservation of momentum along each of the coordinate directions. In order to obtain the momentum conservation equations on differential form, the Reynolds Transport Theorem is applied on the left hand side of Eqn. (2.6), which yields:

$$\int_{\Omega} \left\{ \frac{\partial(\rho u_i)}{\partial t} + \frac{\partial}{\partial x_j}(\rho u_i u_j) \right\} d\Omega = \int_S T_{ij} n_j dS + \int_{\Omega} S_i d\Omega \quad (2.7)$$

Furthermore, the divergence theorem is used to convert the stress term from a surface integral into a volume integral:

$$\int_{\Omega} \left\{ \frac{\partial(\rho u_i)}{\partial t} + \frac{\partial}{\partial x_j}(\rho u_i u_j) \right\} d\Omega = \int_{\Omega} \frac{\partial T_{ij}}{\partial x_j} d\Omega + \int_{\Omega} S_i d\Omega \quad (2.8)$$

Finally, the same argument as in the previous section regarding the arbitrary volume is used to transform the mass conservation equation from integral to differential form:

$$\frac{\partial(\rho u_i)}{\partial t} + \frac{\partial}{\partial x_j}(\rho u_i u_j) = \frac{\partial T_{ij}}{\partial x_j} + S_i \quad (2.9)$$

The stress tensor includes the pressure and the viscous stresses:

$$T_{ij} = - \left(p + \frac{2}{3} \mu \frac{\partial u_k}{\partial x_k} \right) \delta_{ij} + \mu \left(\frac{\partial u_i}{\partial x_j} + \frac{\partial u_j}{\partial x_i} \right) \quad (2.10)$$

Where $k = 1, 2, 3$ and δ_{ij} is the Kronecker delta function. Eqn. (2.10) simplifies into the following when applying the statement that the divergence of the velocities is equal to zero, see Eqn. (2.5):

$$T_{ij} = -p\delta_{ij} + \mu \left(\frac{\partial u_i}{\partial x_j} + \frac{\partial u_j}{\partial x_i} \right) = -p\delta_{ij} + \tau_{ij} \quad (2.11)$$

Where the viscous stresses are:

$$\tau_{ij} = \mu \left(\frac{\partial u_i}{\partial x_j} + \frac{\partial u_j}{\partial x_i} \right) \quad (2.12)$$

The momentum conservation equations can now be rewritten into:

$$\rho \frac{\partial u_i}{\partial t} + \rho \frac{\partial(u_i u_j)}{\partial x_j} = -\frac{\partial p}{\partial x_i} + \frac{\partial \tau_{ij}}{\partial x_j} + S_i \quad (2.13)$$

Eqns. (2.13) form the equations which after the discretization process allow for the velocities to be obtained.

2.3 Pressure Equation

As mentioned in the previous section the momentum equations are a set of three equations. However, they involve four unknowns; three velocities (one for each dimension) and the pressure. Therefore, it is of interest to find the pressure by another equation. The pressure equation is found by taking the divergence of the momentum equations and invoking continuity. Note that Eqn. (2.13) is divided by ρ and that all the terms are moved to the left hand side.

$$\frac{\partial}{\partial x_i} \left(\frac{\partial u_i}{\partial t} + \frac{\partial u_i u_j}{\partial x_j} - \frac{1}{\rho} \frac{\partial \tau_{ij}}{\partial x_j} + \frac{1}{\rho} \frac{\partial p}{\partial x_i} - \frac{1}{\rho} S_i \right) = 0. \quad (2.14)$$

By assuming that the velocities are continuous functions of time the spatial and temporal derivatives can be interchanged to eliminate the time derivative terms using the statement that the divergence of the velocities are equal to zero, cf. [2]. Eqn. (2.14) simplifies to the following:

$$\frac{\partial}{\partial x_i} \left(\frac{\partial u_i u_j}{\partial x_j} - \frac{1}{\rho} \frac{\partial \tau_{ij}}{\partial x_j} + \frac{1}{\rho} \frac{\partial p}{\partial x_i} - \frac{1}{\rho} S_i \right) = 0. \quad (2.15)$$

After the discretization process of Eqn. (2.15) it is possible to find the pressure.

Chapter 3

Discretization

The discretization of the governing equations is carried out in two dimensions and it is not shown for either an implicit or an explicit solver therefore only the discretization of the time derivative term is shown with respect to time. The discretization carried out in order to obtain the velocity equation is only illustrated for one direction.

3.1 Pressure Equation

Eqn. (2.15) is rearranged to:

$$\frac{\partial}{\partial x_i} \left(\frac{1}{\rho} \frac{\partial p}{\partial x_i} \right) = \frac{\partial}{\partial x_i} \left(-\frac{\partial u_i u_j}{\partial x_j} + \frac{1}{\rho} \frac{\partial \tau_{ij}}{\partial x_j} + \frac{1}{\rho} S_i \right) \quad (3.1)$$

Integrating Eqn. (3.1) over the volume yields:

$$\int_{\Omega} \frac{\partial}{\partial x_i} \left(\frac{1}{\rho} \frac{\partial p}{\partial x_i} \right) d\Omega = \int_{\Omega} \frac{\partial}{\partial x_i} \left(-\frac{\partial u_i u_j}{\partial x_j} + \frac{1}{\rho} \frac{\partial \tau_{ij}}{\partial x_j} + \frac{1}{\rho} S_i \right) d\Omega \quad (3.2)$$

Converting the volume integrals in Eqn. (3.2) to surface integrals:

$$\int_S \hat{n}_i \left(\frac{1}{\rho} \frac{\partial p}{\partial x_i} \right) dS = \int_S \hat{n}_i \left(-\frac{\partial u_i u_j}{\partial x_j} + \frac{1}{\rho} \frac{\partial \tau_{ij}}{\partial x_j} + \frac{1}{\rho} S_i \right) dS \quad (3.3)$$

The stencil used to discretize the pressure equation is shown in Fig. 3.1. The left column and bottom row are ghost cells and therefore the discretization is carried out for $p_{(3,3)}$ in order not to be effected by any pressure boundaries. Note that the pressure, density and viscosities are obtained from the center of the control volumes which are represented by parentheses on the figure.

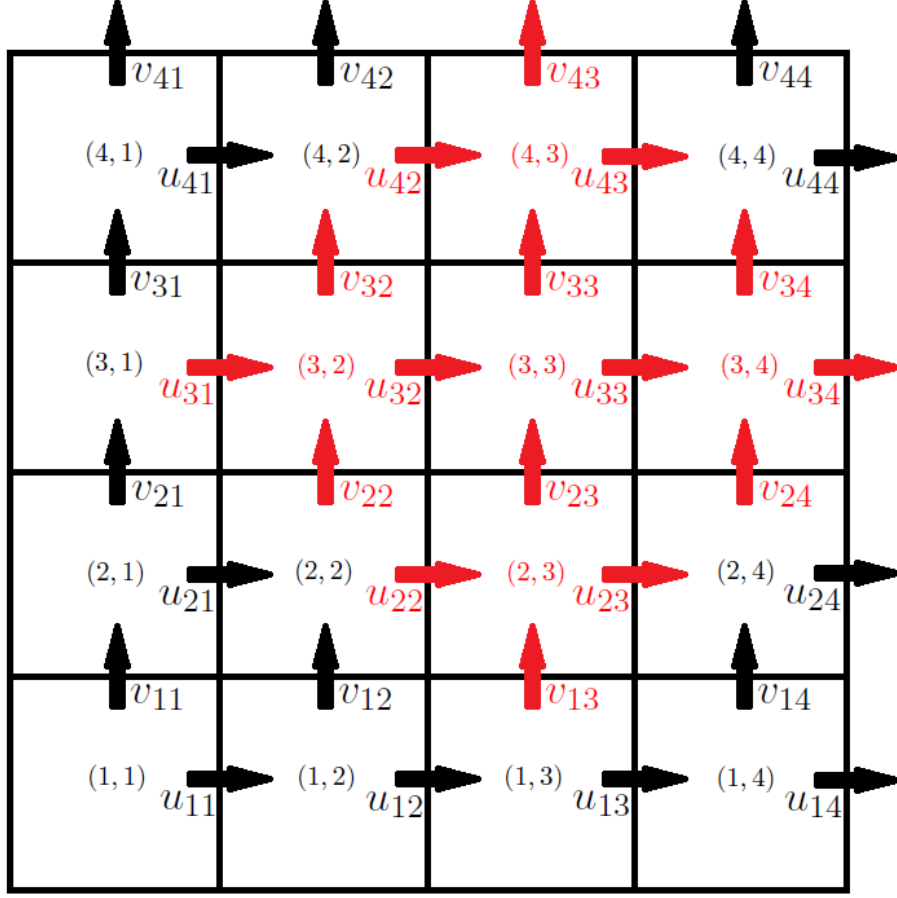


Figure 3.1: The stencil used for discretization of the pressure equation.

The pressure term is discretized as follows:

$$\int_S \hat{n}_i \left(\frac{1}{\rho} \frac{\partial p}{\partial x_i} \right) dS = \frac{1}{\rho} \frac{\partial p}{\partial x} \Big|_w^e \Delta y + \frac{1}{\rho} \frac{\partial p}{\partial y} \Big|_s^n \Delta x \quad (3.4)$$

where

$$\frac{1}{\rho} \frac{\partial p}{\partial x} \Big|_w^e \Delta y = \quad (3.5)$$

$$\frac{2}{\rho_{(3,4)} + \rho_{(3,3)}} \frac{p_{(3,4)} - p_{(3,3)}}{\Delta x} \Delta y - \frac{2}{\rho_{(3,3)} + \rho_{(3,2)}} \frac{p_{(3,3)} - p_{(3,2)}}{\Delta x} \Delta y$$

$$\frac{1}{\rho} \frac{\partial p}{\partial y} \Big|_s^n \Delta x = \quad (3.6)$$

$$\frac{2}{\rho_{(4,3)} + \rho_{(3,3)}} \frac{p_{(4,3)} - p_{(3,3)}}{\Delta y} \Delta x - \frac{2}{\rho_{(3,3)} + \rho_{(2,3)}} \frac{p_{(3,3)} - p_{(2,3)}}{\Delta y} \Delta x$$

The convection terms are discretized as follows (an upwind scheme is used):

$$\int_S \hat{n}_i \left(-\frac{\partial u_i u_j}{\partial x_j} \right) dS = -\frac{\partial uu}{\partial x} \Big|_w^e \Delta y - \frac{\partial uv}{\partial y} \Big|_w^e \Delta y - \frac{\partial vu}{\partial x} \Big|_s^n \Delta x - \frac{\partial vv}{\partial y} \Big|_s^n \Delta x \quad (3.7)$$

where

$$-\frac{\partial uu}{\partial x} \Big|_w^e \Delta y = - \left(\frac{u_{33}^2 - u_{32}^2}{\Delta x} - \frac{u_{32}^2 - u_{31}^2}{\Delta x} \right) \Delta y \quad (3.8)$$

$$-\frac{\partial uv}{\partial y} \Big|_w^e \Delta y = \quad (3.9)$$

$$- \left(\frac{(v_{34} + v_{33})u_{33}}{2\Delta y} - \frac{(v_{24} + v_{23})u_{23}}{2\Delta y} - \left(\frac{(v_{33} + v_{32})u_{32}}{2\Delta y} - \frac{(v_{23} + v_{22})u_{22}}{2\Delta y} \right) \right) \Delta y$$

$$-\frac{\partial vu}{\partial x} \Big|_s^n \Delta x = \quad (3.10)$$

$$- \left(\frac{(u_{43} + u_{33})v_{33}}{2\Delta x} - \frac{(u_{42} + u_{32})v_{32}}{2\Delta x} - \left(\frac{(u_{33} + u_{23})v_{23}}{2\Delta x} - \frac{(u_{32} + u_{22})v_{22}}{2\Delta x} \right) \right) \Delta x$$

$$-\frac{\partial vv}{\partial y} \Big|_s^n \Delta x = - \left(\frac{v_{33}^2 - v_{23}^2}{\Delta y} - \frac{v_{23}^2 - v_{13}^2}{\Delta y} \right) \Delta x \quad (3.11)$$

The diffusion terms are discretized as follows:

$$\begin{aligned} \int_S \hat{n}_i \left(\frac{1}{\rho} \frac{\partial}{\partial x_j} \left(\mu \left(\frac{\partial u_i}{\partial x_j} + \frac{\partial u_j}{\partial x_i} \right) \right) \right) dS = \\ \frac{1}{\rho} \frac{\partial}{\partial x} \left(\mu 2 \frac{\partial u}{\partial x} \right) \Big|_w^e \Delta y + \frac{1}{\rho} \frac{\partial}{\partial y} \left(\mu \left(\frac{\partial u}{\partial y} + \frac{\partial v}{\partial x} \right) \right) \Big|_w^e \Delta y \\ + \frac{1}{\rho} \frac{\partial}{\partial x} \left(\mu \left(\frac{\partial v}{\partial x} + \frac{\partial u}{\partial y} \right) \right) \Big|_s^n \Delta x + \frac{1}{\rho} \frac{\partial}{\partial y} \left(\mu 2 \frac{\partial v}{\partial y} \right) \Big|_s^n \Delta x \end{aligned} \quad (3.12)$$

where

$$\frac{1}{\rho} \frac{\partial}{\partial x} \left(\mu 2 \frac{\partial u}{\partial x} \right) \Big|_w^e \Delta y = \quad (3.13)$$

$$\begin{aligned} & \left[\frac{1}{0.5(\rho_{(3,4)} + \rho_{(3,3)})} \frac{1}{\Delta x} \left(\mu_{(3,4)} 2 \frac{u_{34} - u_{33}}{\Delta x} - \mu_{(3,3)} 2 \frac{u_{33} - u_{32}}{\Delta x} \right) \right. \\ & \left. - \left(\frac{1}{0.5(\rho_{(3,3)} + \rho_{(3,2)})} \frac{1}{\Delta x} \left(\mu_{(3,3)} 2 \frac{u_{33} - u_{32}}{\Delta x} - \mu_{(3,2)} 2 \frac{u_{32} - u_{31}}{\Delta x} \right) \right) \right] \Delta y \\ & \frac{1}{\rho} \frac{\partial}{\partial y} \left(\mu \left(\frac{\partial u}{\partial y} + \frac{\partial v}{\partial x} \right) \right) \Big|_w^e \Delta y = \end{aligned} \quad (3.14)$$

$$\begin{aligned} & \left[\frac{1}{0.5(\rho_{(3,4)} + \rho_{(3,3)})} \frac{1}{\Delta y} \left(\frac{\mu_{(3,3)} + \mu_{(3,4)} + \mu_{(4,3)} + \mu_{(4,4)}}{4} \left(\frac{u_{43} - u_{33}}{\Delta y} + \frac{v_{34} - v_{33}}{\Delta x} \right) \right. \right. \\ & \quad \left. \left. - \frac{\mu_{(3,3)} + \mu_{(3,4)} + \mu_{(2,3)} + \mu_{(2,4)}}{4} \left(\frac{u_{33} - u_{23}}{\Delta y} + \frac{v_{24} - v_{23}}{\Delta x} \right) \right) \right. \\ & \left. - \left(\frac{1}{0.5(\rho_{(3,3)} + \rho_{(3,2)})} \frac{1}{\Delta y} \left(\frac{\mu_{(3,2)} + \mu_{(3,3)} + \mu_{(4,2)} + \mu_{(4,3)}}{4} \left(\frac{u_{42} - u_{32}}{\Delta y} + \frac{v_{33} - v_{32}}{\Delta x} \right) \right. \right. \right. \\ & \quad \left. \left. - \frac{\mu_{(3,2)} + \mu_{(3,3)} + \mu_{(2,2)} + \mu_{(2,3)}}{4} \left(\frac{u_{32} - u_{22}}{\Delta y} + \frac{v_{23} - v_{22}}{\Delta x} \right) \right) \right) \right] \Delta y \\ & \frac{1}{\rho} \frac{\partial}{\partial x} \left(\mu \left(\frac{\partial v}{\partial x} + \frac{\partial u}{\partial y} \right) \right) \Big|_s^n \Delta x = \end{aligned} \quad (3.15)$$

$$\begin{aligned} & \left[\frac{1}{0.5(\rho_{(4,3)} + \rho_{(3,3)})} \frac{1}{\Delta x} \left(\frac{\mu_{(3,3)} + \mu_{(3,4)} + \mu_{(4,3)} + \mu_{(4,4)}}{4} \left(\frac{v_{34} - v_{33}}{\Delta x} + \frac{u_{43} - u_{33}}{\Delta y} \right) \right. \right. \\ & \quad \left. \left. - \frac{\mu_{(3,2)} + \mu_{(3,3)} + \mu_{(4,2)} + \mu_{(4,3)}}{4} \left(\frac{v_{33} - v_{32}}{\Delta x} + \frac{u_{42} - u_{32}}{\Delta y} \right) \right) \right. \\ & \left. - \left(\frac{1}{0.5(\rho_{(3,3)} + \rho_{(2,3)})} \frac{1}{\Delta x} \left(\frac{\mu_{(3,3)} + \mu_{(3,4)} + \mu_{(2,3)} + \mu_{(2,4)}}{4} \left(\frac{v_{24} - v_{23}}{\Delta x} + \frac{u_{33} - u_{23}}{\Delta y} \right) \right. \right. \right. \\ & \quad \left. \left. - \frac{\mu_{(3,2)} + \mu_{(3,3)} + \mu_{(2,2)} + \mu_{(2,3)}}{4} \left(\frac{v_{23} - v_{22}}{\Delta x} + \frac{u_{32} - u_{22}}{\Delta y} \right) \right) \right) \right] \Delta x \end{aligned}$$

$$\frac{1}{\rho} \frac{\partial}{\partial y} \left(\mu 2 \frac{\partial v}{\partial y} \right) \Big|_s^n \Delta x = \quad (3.16)$$

$$\begin{aligned} & \left[\frac{1}{0.5(\rho_{(4,3)} + \rho_{(3,3)})} \frac{1}{\Delta y} \left(\mu_{(4,3)} 2 \frac{v_{43} - v_{33}}{\Delta y} - \mu_{(3,3)} 2 \frac{v_{33} - v_{23}}{\Delta y} \right) \right. \\ & \left. - \left(\frac{1}{0.5(\rho_{(3,3)} + \rho_{(2,3)})} \frac{1}{\Delta y} \left(\mu_{(3,3)} 2 \frac{v_{33} - v_{23}}{\Delta y} - \mu_{(2,3)} 2 \frac{v_{23} - v_{13}}{\Delta y} \right) \right) \right] \Delta x \end{aligned}$$

The gravity term is discretized as follows:

$$\int_S \hat{n}_i \left(\frac{1}{\rho} S_i \right) dS = g_y \Big|_s^n \Delta x \quad (3.17)$$

3.2 Velocity Equations

Eqn. (2.13) is rearranged:

$$\frac{\partial u_i}{\partial t} = -\frac{\partial(u_i u_j)}{\partial x_j} - \frac{1}{\rho} \frac{\partial p}{\partial x_i} + \frac{1}{\rho} \frac{\partial \tau_{ij}}{\partial x_j} + \frac{1}{\rho} S_i. \quad (3.18)$$

The stencil used for the discretization of the velocity equation is shown in Fig. 3.2. The left column and bottom row are ghost cells and therefore the discretization is carried out for u_{33} in order not to be effected by any boundaries.

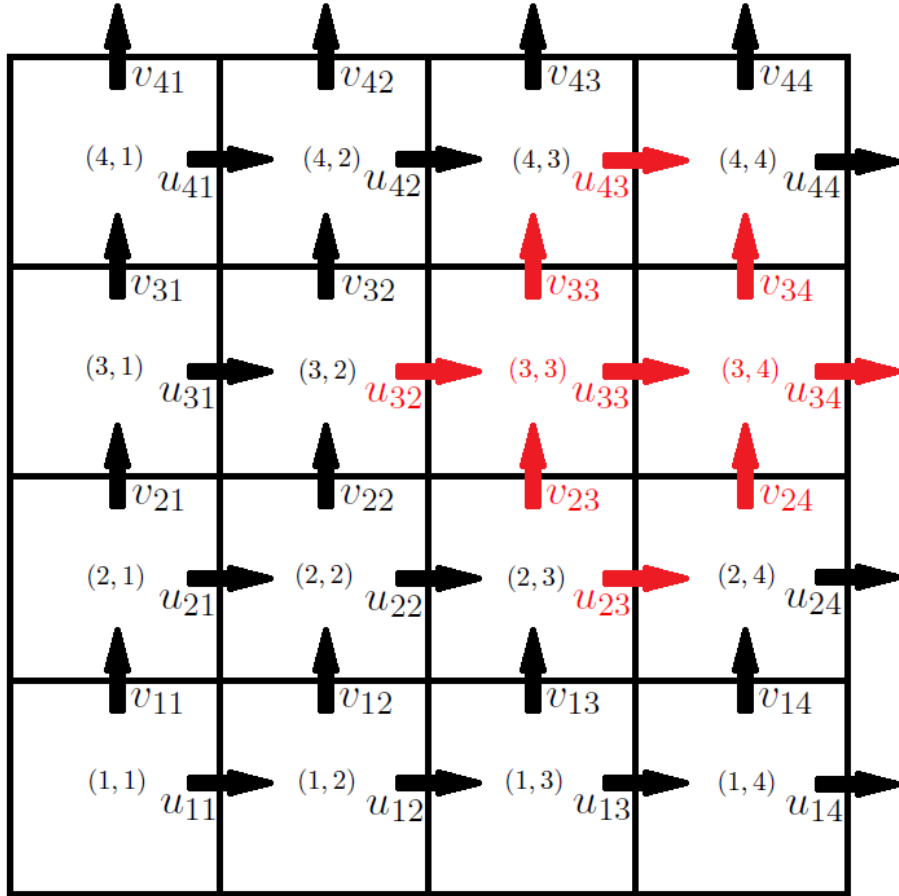


Figure 3.2: The stencil used for discretization of the velocity equations.

The discretization is only carried out in the u direction, which makes Eqns. (3.18) turn into:

$$\frac{\partial u}{\partial t} = -\frac{\partial(u^2)}{\partial x} - \frac{\partial(uv)}{\partial y} - \frac{1}{\rho} \frac{\partial p}{\partial x} + \frac{1}{\rho} \frac{\partial}{\partial x} \left(\mu^2 \frac{\partial u}{\partial x} \right) + \frac{1}{\rho} \frac{\partial}{\partial y} \left(\mu \left(\frac{\partial u}{\partial y} + \frac{\partial v}{\partial x} \right) \right) \quad (3.19)$$

Integrating Eqn. (3.19) over the volume yields:

$$\int_{\Omega} \frac{\partial u}{\partial t} d\Omega = \int_{\Omega} \left(-\frac{\partial(u^2)}{\partial x} - \frac{\partial(uv)}{\partial y} - \frac{1}{\rho} \frac{\partial p}{\partial x} + \frac{1}{\rho} \frac{\partial}{\partial x} \left(\mu 2 \frac{\partial u}{\partial x} \right) + \frac{1}{\rho} \frac{\partial}{\partial y} \left(\mu \left(\frac{\partial u}{\partial y} + \frac{\partial v}{\partial x} \right) \right) \right) d\Omega \quad (3.20)$$

The time derivative term is discretized as follows:

$$\int_{\Omega} \frac{\partial u}{\partial t} d\Omega = \frac{u_{33}^{t+\Delta t} - u_{33}^t}{\Delta t} \Delta x \Delta y \quad (3.21)$$

The convection terms are discretized as follows (an upwind scheme is used):

$$\int_{\Omega} \left(-\frac{\partial(u^2)}{\partial x} \right) d\Omega = \int_S \hat{n} \left(-\frac{\partial(u^2)}{\partial x} \right) dS = -u|_w^e \Delta y = -(u_{33}^2 - u_{32}^2) \Delta y \quad (3.22)$$

$$\begin{aligned} \int_{\Omega} \left(-\frac{\partial(uv)}{\partial y} \right) d\Omega &= \int_S \hat{n} \left(-\frac{\partial(uv)}{\partial y} \right) dS = \\ &= -uv|_s^n \Delta x = - \left(\frac{(v_{34} + v_{33})u_{33}}{2} - \frac{(v_{24} + v_{23})u_{23}}{2} \right) \Delta x \end{aligned} \quad (3.23)$$

The pressure term is discretized as follows:

$$\begin{aligned} \int_{\Omega} \left(-\frac{1}{\rho} \frac{\partial p}{\partial x} \right) d\Omega &= \int_S \hat{n} \left(-\frac{1}{\rho} \frac{\partial p}{\partial x} \right) dS = - \frac{1}{\rho} p|_w^e \Delta y = \\ &= - \frac{2}{\rho_{(3,4)} + \rho_{(3,3)}} (p_{(3,4)} - p_{(3,3)}) \Delta y \end{aligned} \quad (3.24)$$

The diffusion terms are discretized as follows:

$$\int_{\Omega} \left(\frac{1}{\rho} \frac{\partial}{\partial x} \left(\mu 2 \frac{\partial u}{\partial x} \right) \right) d\Omega = \int_S \hat{n} \left(\frac{1}{\rho} \frac{\partial}{\partial x} \left(\mu 2 \frac{\partial u}{\partial x} \right) \right) dS = \frac{1}{\rho} \left(\mu 2 \frac{\partial u}{\partial x} \right) \Big|_w^e \Delta y = \quad (3.25)$$

$$\begin{aligned} &= \frac{1}{0.5(\rho_{(3,4)} + \rho_{(3,3)})} \left(\mu_{(3,4)} 2 \frac{u_{34} - u_{33}}{\Delta x} - \mu_{(3,3)} 2 \frac{u_{33} - u_{32}}{\Delta x} \right) \Delta y \\ \int_{\Omega} \left(\frac{1}{\rho} \frac{\partial}{\partial y} \left(\mu \left(\frac{\partial u}{\partial y} + \frac{\partial v}{\partial x} \right) \right) \right) d\Omega &= \\ \int_S \hat{n} \left(\frac{1}{\rho} \frac{\partial}{\partial y} \left(\mu \left(\frac{\partial u}{\partial y} + \frac{\partial v}{\partial x} \right) \right) \right) dS &= \\ \frac{1}{\rho} \left(\mu \left(\frac{\partial u}{\partial y} + \frac{\partial v}{\partial x} \right) \right) \Big|_s^n \Delta x &= \\ \frac{1}{0.5(\rho_{(3,4)} + \rho_{(3,3)})} \left(\frac{\mu_{(3,3)} + \mu_{(3,4)} + \mu_{(4,3)} + \mu_{(4,4)}}{4} \left(\frac{u_{43} - u_{33}}{\Delta y} + \frac{v_{34} - v_{33}}{\Delta x} \right) \right. \\ &\quad \left. - \frac{\mu_{(3,3)} + \mu_{(3,4)} + \mu_{(2,3)} + \mu_{(2,4)}}{4} \left(\frac{u_{33} - u_{23}}{\Delta y} + \frac{v_{24} - v_{23}}{\Delta x} \right) \right) \Delta x \end{aligned} \quad (3.26)$$

Chapter 4

Boundary Conditions

The boundary condition presented in this technical report is the wall boundary condition (no slip).

4.1 Pressure

The pressure boundary condition can be expressed as:

$$\frac{\partial P}{\partial x} = 0, \text{ on a vertical wall} \quad (4.1)$$

$$\frac{\partial P}{\partial y} = 0, \text{ on a horizontal wall} \quad (4.2)$$

In order to understand the implementation on discretized form e.g. consider the pressure term in Eqn. (3.3). When integrating this term one obtains contributions from east, west, south, and north as seen in Eqns. (3.5) and (3.6). However, now let's assume that the considered control volume lies at the left boundary. In that case the west contribution would vanish and that may be implemented with a ghost cell e.g. $p_{(3,2)} = p_{(3,3)}$ in Eqn. (3.5).

4.2 Velocity

The wall condition is implemented by introducing zero velocity in both directions (2D) on the boundary. The zero velocity in the normal direction is straight forwardly implemented. The zero velocity in the tangential direction may also be implemented with a ghost cell, cf. Fig 4.1 and Eqn. (4.3). In Fig. 4.1 the horizontal velocity inside the domain and in the ghostcells are shown.

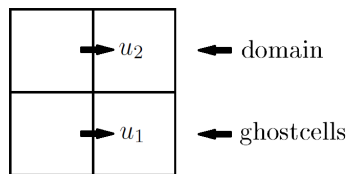


Figure 4.1: Illustration of velocities in the domain and ghostcells.

Realizing that the velocity in the midpoint between u_1 by u_2 should be zero and expressing u_1 by u_2 , then enables the tangential velocity to be implemented:

$$u_1 = -u_2 \tag{4.3}$$

Bibliography

- [1] J. H. Hattel. *Fundamentals of Numerical Modelling of Casting Processes*. Polyteknisk Forlag, 2005.
- [2] H. B. Bingham. Computational fluid dynamics: Lecture note for course no. 41319. 2009.
- [3] K. M. Kalland. A navier-stokes solver for single- and two-phase flow. Master's thesis, University of Oslo, 2008.
- [4] Annika Gram. *Numerical modelling of Self-Compacting Concrete Flow*. PhD thesis, Royal Institute of Technology (KTH), 2009.
- [5] Lars N. Thrane. *Form Filling with Self-Compacting Concrete*. PhD thesis, Technical University of Denmark (DTU), 2007.

F TECHNICAL REPORT-II

J. Spangenberg, C. C. Tutum, and J. H. Hattel (2012). Optimization of Casting Process Parameters for Homogeneous Aggregate Distribution in Self-Compacting Concrete: A Case Study.

Technical Report - II

**Optimization of Casting Process Parameters for Homogeneous
Aggregate Distribution in SCC: A Case Study**

Jon Spangenberg, Cem C. Tutum, and Jesper H. Hattel

**Department of Mechanical Engineering
Technical University of Denmark
March, 2012**

Copyright (c), Jon Spangenberg, 2012
Department of Mechanical Engineering
Technical University of Denmark

Table of Contents

1	Abstract	1
2	Introduction	3
3	Numerical Model	5
3.1	Theory and Governing Equations	5
3.2	Implementation of Model in Matlab	7
4	Optimization Methodology	9
4.1	Optimization Algorithm	9
4.2	Optimization Procedure and Process Integration	10
5	Results and Discussions	13
6	Conclusion	15
	Bibliography	17

Chapter 1

Abstract

Self-compacting concrete (SCC) is a common construction material of which applications cover from classical house building to super structures (e.g. skyscrapers). SCC costs less than conventional concrete in many application areas, such as beam or wall castings, under the assumption of avoidance of heterogeneities during the casting process. This technical report illustrates how the applied casting technique, i.e. scheduling of the inlets (order and active durations of the inlets), for an SCC beam can be optimized in order to increase the homogeneity of the aggregate distribution while maintaining a smooth geometry of the casted beam at the end of the process. The optimization algorithm, i.e. constrained single objective genetic algorithm (SOGA), is coupled with a two dimensional computational fluid dynamics (CFD) model, which predicts the aggregate distribution. The process parameters included in the optimization are the number of inlets which varies from one to three and the filling duration of each of the inlets. In this case study the optimization algorithm improved the casting technique with 20%.

Chapter 2

Introduction

Conventional concrete consists of cement, water, aggregates and possibly micro silica, fly ash as well as different chemical agents as air and retarder. SCC consists of the same ingredients, however a special form of super-plasticizer is also added to increase the fluidity. The advantage of the higher fluidity is the cancellation of the vibration process, since SCC fills out the formwork under its own weight. On the other hand, the disadvantage is that the SCC gets more prone to dynamic segregation during the casting, which may lead to a heterogeneous aggregate distribution and the worst case scenario; a decreased load carrying capacity of the structural element. Lately, numerical models have been developed to predict the aggregate distribution in order to produce a tool for planning and design of SCC castings. Estimation of particle paths based on numerical obtained flow fields were illustrated in [1], while discrete particle paths inside a non-Newtonian fluid were demonstrated in [2]. Another study showed how a CFD model coupled with a scalar based particle evaluation could capture the main trends of the aggregate distribution in a casting with an SCC like suspension fluid, see [3]. In addition, recently a slightly modified version of the numerical model in [4] was found to be capable of capturing the aggregate distribution in a real SCC casting of a beam.

In the present technical report the latter mentioned numerical model is coupled with a single objective genetic algorithm, whose aim is to obtain the most uniform distribution of aggregates. This technical report is a case study illustrating how an optimization algorithm can improve the homogeneity of the aggregate distribution by rescheduling the casting technique. The study is a follow up to the feasibility study carried out in [5] and the three primary differences between the two studies are the use of the modified numerical model, the use of up to three inlets with varying filling durations instead of one inlet, and also the addition of three constraints.

The technical report presents first the numerical method used to calculate the non-Newtonian flow behaviour of the SCC and the flow induced migration of the aggregates. Next, the optimization algorithm is described together with the constraint handling procedure. Afterwards, the results of the optimization are presented together with a discussion of the best casting technique obtained. Finally, the conclusion sums up the study and describes future perspectives in this application field.

Chapter 3

Numerical Model

3.1 Theory and Governing Equations

Dealing with dynamic segregation in a suspension fluid like SCC is a multi physical problem. The numerical model captures the highly non-linear phenomena by taking the following three effects into account:

1. The global non-Newtonian flow of SCC.
2. The interaction between matrix¹ and the large aggregates.
3. The interaction between the aggregates.

The global non-Newtonian flow is captured by solving the continuity equation given in Eqn. (3.1) together with the momentum equations given in Eqn. (3.2).

$$\frac{\partial \rho}{\partial t} + \frac{\partial}{\partial x_j}(\rho u_j) = 0 \quad (3.1)$$

$$\frac{\partial(\rho u_i)}{\partial t} + \frac{\partial}{\partial x_j}(\rho u_i u_j) = \frac{\partial T_{ij}}{\partial x_j} + S_i \quad (3.2)$$

where ρ is the density of the SCC, u is the velocity vector, t is the time, x is the spatial components, j is the notation direction, T is the stress tensor which includes the pressure and the viscous stresses, i is the notation denoting a scalar equation for each of the three dimensions, and S is the gravitational force. The bi-viscosity material model in Eqns. (3.3) and (3.4) is used as constitutive law to solve Eqns. (3.1) and (3.2).

$$\tau^{ref} = \mu_{init} \dot{\gamma}^{ref} \quad \text{for } \dot{\gamma}^{ref} < \dot{\gamma}_0^{ref} \quad (3.3)$$

$$\tau^{ref} = \tau_0 + \mu_p \dot{\gamma}^{ref} \quad \text{for } \dot{\gamma}^{ref} \geq \dot{\gamma}_0^{ref} \quad (3.4)$$

Where τ^{ref} is reference shear stress, μ_{init} is the initial viscosity, $\dot{\gamma}^{ref}$ is the reference shear rate, $\dot{\gamma}_0^{ref}$ is the shifting reference shear rate between the two equations, τ_0 is the yield stress, and μ_p is the plastic viscosity. In Eqns. (3.3) and (3.4) the shear rates and shear stresses are described as reference shear rates and reference shear stresses, respectively, because it is a material law which is valid for a multi-dimensional stress state. The CFD solver couples to the material law based on the Von Mises yield criterion:

$$\dot{\gamma}^{ref} = \sqrt{\frac{1}{2} \dot{\gamma}_{ij} \dot{\gamma}_{ij}} \quad (3.5)$$

¹Matrix = cement paste and aggregates which are less than 11mm (in this case).

A sketch of the bi-viscosity model is shown in Fig. 3.1.

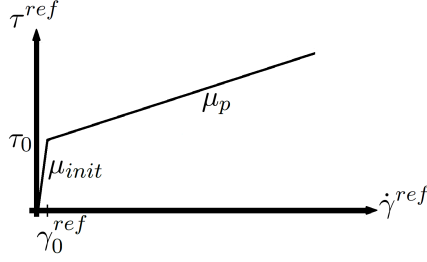


Figure 3.1: *The bi-viscosity material model.*

The interaction between the matrix and the large aggregates is captured by solving a settling velocity expression based on evaluating how gravity, buoyancy and Stokes drag force affect a spherical particle (aggregate). The settling velocity V^s in Eqn. (3.6) describes the relative velocity between the aggregate and the SCC.

$$V^s = \frac{d_a^2 g (\rho_a - \rho_f) \alpha}{18 \mu_{app}} \quad (3.6)$$

Where d_a is the diameter of the aggregate, g is the gravity, ρ_a is the density of the aggregate, α is a parameter found to be equal to 1.45 in [4] (for this particularly SCC), and μ_{app} is the apparent viscosity. The apparent viscosity is the actual viscosity applied in the CFD solver and it is expressed in Eqns. (3.7) and (3.8) for the bi-viscosity shown in Eqns. (3.3) and (3.4). This connection between the global flow and the aggregates forms the first of two momentum couplings between the SCC and the aggregates.

$$\mu^{app} = \mu_{init} \quad \text{for } \dot{\gamma}^{ref} < \dot{\gamma}_0^{ref} \quad (3.7)$$

$$\mu^{app} = \frac{\tau_0}{\dot{\gamma}^{ref}} + \mu_p \quad \text{for } \dot{\gamma}^{ref} \geq \dot{\gamma}_0^{ref} \quad (3.8)$$

The second momentum coupling is carried out by the local aggregate volume fraction's effect on the rheological parameters. The yield stress and plastic viscosity's dependency of the local aggregate volume fraction is based on Chateau et al. [6] and Krieger et al. [7], see Fig 3.2. The aggregate volume fraction considered to effect the rheological parameters are the aggregates from 6 to 16 mm in [4], whose volume fraction corresponds to 0.33 when homogeneous. The aggregates allowed to settle in the numerical simulations though are only the aggregates from 11 to 16 mm and they have a volume fraction of 0.16. This change is made in order to decrease memory use and the calculation time of the simulation. The simulated aggregates are modelled as spheres with a diameter of 14 mm.

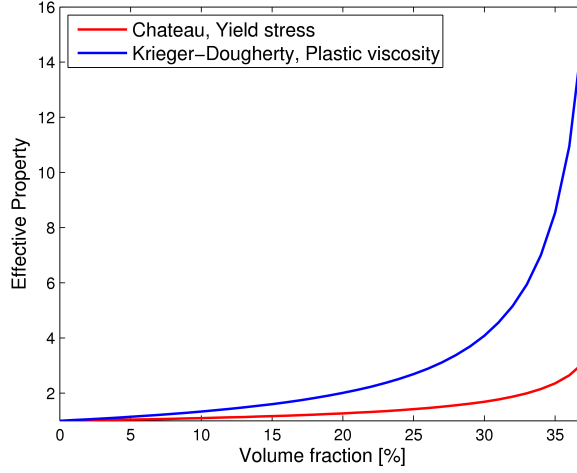


Figure 3.2: *The bi-viscosity material model.*

The other material properties used in this study are similar to the ones found in [4]. The bi-viscosity rheological parameters are a yield stress of 40 Pa and a plastic viscosity of 100 Pas. The density of the SCC is 2346 kg/m³ and the density of the aggregates is 2712 kg/m³.

The interaction between the aggregates is more qualitatively taken into account in this numerical model. The considered aggregates are prevented from reaching a volume fraction higher than the maximum volume fraction of 0.39.

3.2 Implementation of Model in Matlab

The global non-Newtonian flow of SCC is calculated by a CFD-solver developed in Matlab. The CFD-solver uses the Finite Volume Method (FVM) to find the pressure and velocity field on a staggered grid and the Volume Of Fluid (VOF) method to track the free surface. The pressure and viscous stresses are calculated implicitly with a direct solver, while the convective terms in the momentum equations and the free surface are updated explicitly. The migration of the aggregates is captured by an advection and settling calculation. The advection procedure is carried out by solving the transport equation in Eqn. (3.9).

$$\frac{\partial \phi}{\partial t} + \nabla(\phi u_i) = 0 \quad (3.9)$$

Where ϕ is the volume fraction of the aggregates. The settling calculation is performed with the discretized equation in Eqn. (3.10), which is based on a mass conservation on a finite volume grid. Note that Eqn. (3.10) is only valid for a two dimensional case on a structured grid.

$$\phi_k^{t+\Delta t} = \phi_k \left(1 - V_k^s \frac{\Delta t}{\Delta y} \right) + \phi_{k+1}^t + V_{k+1}^s \frac{\Delta t}{\Delta y} \frac{F_{k+1}}{F_k} \quad (3.10)$$

Where F is the volume of fluid, $\Delta x/\Delta y$ are the lengths of the control volume in each direction, and k is the notation denoting the cell number in the vertical direction.

The optimization algorithm is applied on a casting of a 0.3 m high and 3 m long beam. Due to computational speed the aggregate distribution in the beam casting is predicted based on a two dimensional simulation, thus the reinforcement is assumed to be arranged in such a way that it has negligible effect on the dynamic segregation pattern. The length and height of each control volume is 0.02 m and the number of used control volumes varies between 3000 and 3600 depending on the casting technique. The calculation time for each simulation is approximately 1 hour. All the boundaries are modelled as walls with zero velocity at the surface; however, since the mould is not closed in real life at the top, the upper boundary does not come into play. The three inlets are placed at 0.5 m, 1.5 m, and 2.5 m from the one end of the beam and the width of the inlets are 0.1 m each, see Fig. 3.3.

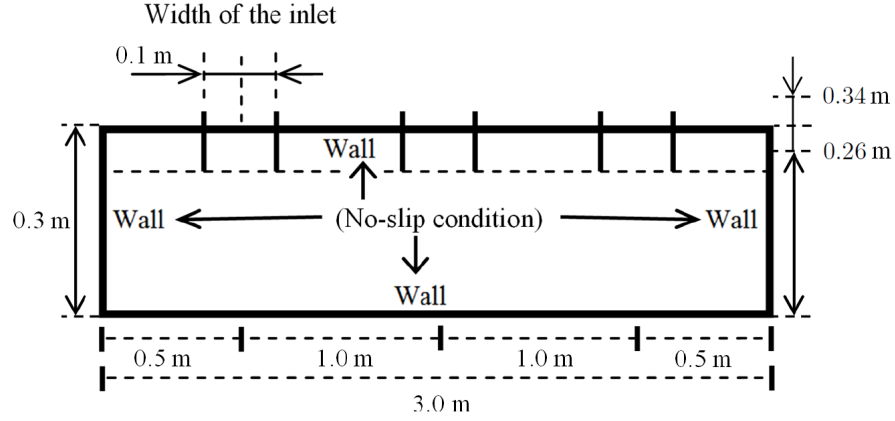


Figure 3.3: Inlet position and boundary condition.

The process parameters varied in this optimization study are the sequence of which the inlets are filling and their individual filling duration. The total filling duration is 28.8 s for all of the simulation and the mass rate is kept constant. Three constraints are taken into account in order to find realistic and usable casting scenarios. The first constraint is a limitation on the free surface height of the SCC, because the yield stress behavior makes the free surface differ from a horizontal straight line. Consequentially, a casting scenario could occur where SCC would flow beyond the edge of the mould in real life. The overflow of the mould is not taken into account in the numerical model, but in order to prevent such a scenario the simulation is terminated if the free surface of the SCC reaches a height greater than 4 cm above the edge of the mould. The second constraint is a limitation on the minimum height. A casting scenario where the minimum height of the free surface at the end of the casting is less than 4 cm from the mould edge is also prohibited. The third and final constraint is a minimum volume fraction limitation. The volume fraction of the coarsest aggregates is not allowed to be less than 10% anywhere at the end of the simulation.

Chapter 4

Optimization Methodology

4.1 Optimization Algorithm

In this technical report an evolutionary single objective genetic algorithm (SOGA) is applied to solve the constrained optimization problem given in the following. The objective is to get a uniform distribution of aggregates which is subject to the constraints: (a) the maximum height of the material that is poured into the mould (this is a dynamic constraint and it is checked every time step of the casting simulation. The simulation is stopped if it is violated and a flag is put to that particular design or individual to state that it is an infeasible solution), (b) the minimum value for the volume fraction should be higher than 0.10 (this is a static constraint), (c) the minimum height of the material poured should be higher than 0.26 m as indicated in Fig. 3.3. In mathematical terms, this optimization problem can be written as minimization of the standard deviation of the volume fraction scalar (ϕ) at the end of the process, which is subjected to the aforementioned process specific constraints, see Eqn. (4.1).

$$\begin{aligned} \text{Minimize : } & \sqrt{\frac{1}{(n_{cv})} \sum_{i=1}^{n_{cv}} (\phi - \bar{\phi})^2} \\ & (\phi_i) > 0.10 \\ \text{subjected to : } & h_{min} > 0.26 \\ & h_{max} < 0.34 \end{aligned} \tag{4.1}$$

Genetic algorithms (GAs), as a popular class of nature inspired optimization algorithms, are stochastic methods that mimic evolutionary principles, e.g. natural selection and the survival of the fittest, to constitute their search procedure. As opposed to classical algorithms (e.g. mathematical programming algorithms), they work with a set of solutions (population) instead of a single point and this gives them a robust search capability to explore a complex landscape (discontinuous, noisy, multi-modal, multi-funnel, etc.). The combination of different operators adjust the weighting between exploration and exploitation of different parts of the search space. Since they do not need any gradient information, they are very much suitable for black-box (e.g. commercial software) optimization applications as well as implicit function evaluations where the dependence of the response explored is not an explicit function of the design variables as in this particular case presented [8].

SOGA is a generic constrained single objective genetic algorithm (GA) which uses binary encoding for the representation of the design variables. The initial population, represented by binary strings of different lengths for each design variable, is composed of randomly distributed solutions in the design space. The algorithm is based on several genetic operators: constrained binary tournament selection [9], twopoint crossover and uniform mutation. Moreover it is an elitist algorithm which means that the best solutions found so far are preserved to accelerate convergence towards true or near optimum while still having explorative search to avoid premature convergence. Elitism is implemented in a way that both parent and children populations are combined to form a mixed population (before selection) at the end of the reproduction operations and this gives an opportunity to build the next generation from the best of the two populations. Constrained Binary tournament selection implemented in SOGA is composed of two tournaments in which every individual compete only once in each. The other genetic operators are implemented in a standard way [9]. SOGA has actually been converted from mNSGA-II (MATLAB implementation of NSGA-II [10] that is a similar replication of the original algorithm [11]) which has been successfully applied elsewhere [12]. Therefore, non-dominated sorting and crowding distance operators together with simulated binary crossover and polynomial mutation operators (built for real coded GAs) have been removed.

4.2 Optimization Procedure and Process Integration

The flowchart of the optimization procedure is shown in Fig. 4.1, which includes a process integration of the 2-D CFD code developed in MATLAB and the optimization algorithm SOGA which is also implemented in MATLAB. The optimization cycle was initiated by creating an initial population of 10 randomly distributed set of design variables, i.e. the number and order of the inlets as well as the filling duration for each (i.e. active ones). The size of the population could be argued. This is because the computation time of each function evaluation is approximately 1 hour using 12 cores (Intel Xeon CPU, 12 cores, X5690 @3.47 GHz), hence calculation cost is too high to use a larger population, consequently getting a better solution as compared to the initial design is aimed to be satisfactory. The total number of generations was 10. The probabilities for the single point crossover and mutation operators were, 0.65 and $1/li$ (li : total string length). The number and the order of the inlets were represented with the floating values rounded integers of 1 or 2 for the first bit, and the next bit (representing the next inlet) 2 or 1 correspondingly.

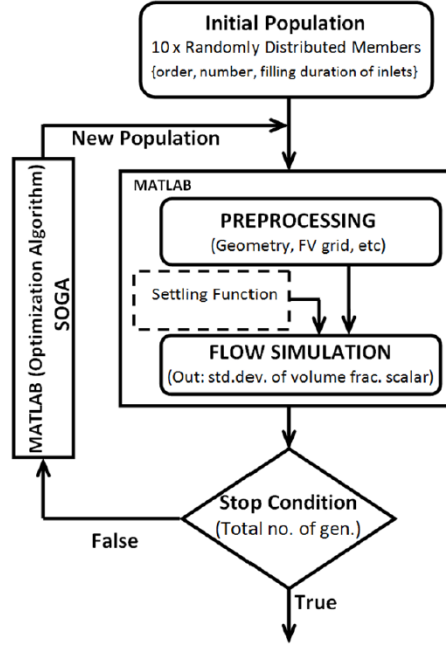


Figure 4.1: *Flowchart of the optimization problem.*

As mentioned in the previous section, the maximum height constraint is checked at every time step of the simulation and the simulation is stopped (indicating the design is infeasible and the total constraint violation is assigned an infinitely big number to make that design disappear in the selection procedure) if the constraint is violated.

Chapter 5

Results and Discussions

The numerical results of a form filling with one inlet (i.e. middle) are illustrated in Fig. 5.1. The evolution of the casting process is shown at three different times.

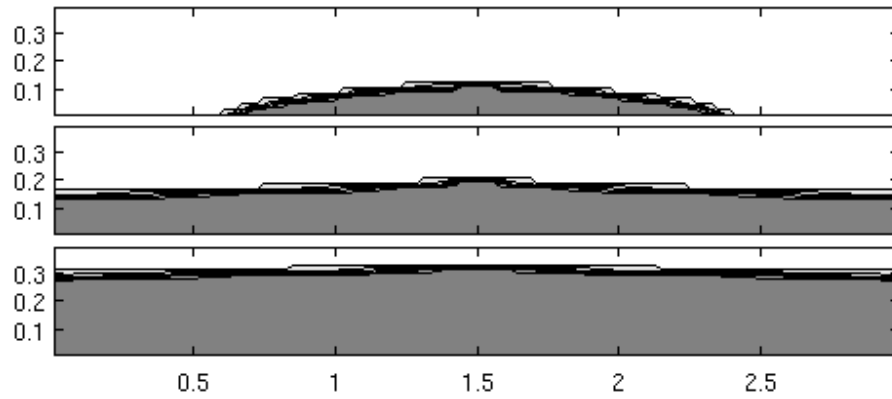


Figure 5.1: *The evolution of the casting process.*

The objective and constraint results obtained for the case shown in Fig. 5.1 are presented in Tab. 5.1 together with results from simulations carried out using two and three inlets. The simulation carried out with two inlets initiated the form filling with the middle inlet and finalized with the left one. Each is active for 14.4 s. The simulation with three inlets is also initiated with the middle inlet and finalized with the right inlet. Each of them is filling for 9.6 s.

Model	Std. dev. ϕ	Min. ϕ	Max. Height	Min. Height
One Inlet	0.0156	0.1204	Ok	0.29
Two Inlets	0.0168	0.1216	Ok	0.28
Three Inlets	0.0154	0.1148	Ok	0.27

Table 5.1: Table with results from parameter study.

The brief parameter study shown in Tab. 5.1 clearly indicates the high non-linearity involved in the process and therefore how difficult it is to predict the best casting technique, e.g. one would expect that it is preferable to use two inlets as compared to one. However, in this specific case the results show that the standard deviation is lower when using the single inlet (the middle). In addition, the table shows that the standard deviation and

minimum aggregate volume fraction are not fully correlated. In order to understand the correlation between the standard deviation and the minimum volume fraction a multi objective optimization study could be carried out in which the minimum volume fraction constraint is converted to an objective on its own. However, in this study the single objective is kept and in Fig. 5.2 the results of this optimization analysis are shown. The figure shows the standard deviation as a function of the generations for the best individual and the average of all individuals. Note, that the infeasible solutions are not being taking into account when finding the average value.

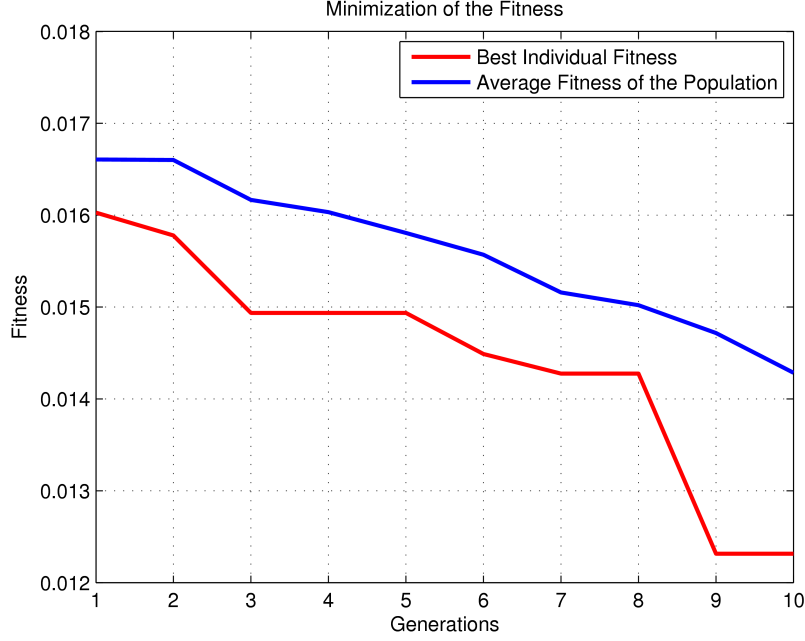


Figure 5.2: *Generations as a function of the standard deviation for best individual and average individuals.*

Fig. 5.2 shows that the best solution improves five times within the ten generations and ends up with the final result at the ninth generation. Most likely, it is possible to obtain a better solution if the number of generations and individuals in each generations are increase. However, in order to run the optimization study within a reasonable time, ten generations and ten individuals are used in this study. The process parameters for the best solution are; a casting initiation at the left inlet, followed by the middle inlet and finalizing with the right inlet. The casting durations are 8.6s at the left inlet, 17.1s at the middle inlet, and 3.1s at the right inlet. This casting scenario leads to a standard deviation of 0.0123, a minimum volume fraction of 0.13, an acceptable maximum height, and a minimum height of 0.28m. The best casting scenario obtained improves the standard deviation with 20% and the minimum volume fraction with 13% as compared to using three inlets with the same filling duration, cf. Tab. 5.1. Another interesting observation is that the best solution is obtained when the third (the right) inlet is almost inactive, which is also a non-intuitively pattern.

Chapter 6

Conclusion

In this technical report it was shown that a GA can be an excellent tool for improving the technique used when casting with SCC. In this specific case it was shown that an improvement of 20% could be obtained by changing the sequence and filling duration of the inlets. Furthermore, the investigation showed that the standard deviation and minimum volume fraction is not fully correlated and it could therefore be of interest to carry out a multiple objective optimization study to understand the correlation further.

For future work it would be interesting to investigate how the best solution changes depending on the height of the mould. However, as the height of the mould increases, the calculation domain (i.e. therefore calculation time) increases as well. Hence, it would be beneficial to apply a suitable metamodeling technique (e.g. Kriging, Artificial Neural Network or Response Surface Modeling) to reduce the number of "real" function evaluations. Another way to reduce the total computational time of the optimization study is to parallelize the optimization algorithm, SOGA, by distributing the individuals of each generation into a cluster of nodes.

Bibliography

- [1] Lars N. Thrane. *Form Filling with Self-Compacting Concrete*. PhD thesis, Technical University of Denmark (DTU), 2007.
- [2] Jon Spangenberg, Nicolas Roussel, Jesper H. Hattel, Jesper Thorborg, Mette R. Geiker, Henrik Stang, and Jan Skocek. Prediction of the impact of flow induced inhomogeneities in self compacting concrete (scc). In *Design, Production and Placement of Self-Consolidating Concrete, Proceedings of SCC2010*.
- [3] J. Spangenberg, N. Roussel, J.H. Hattel, H. Stang, J. Skocek, and M.R. Geiker. Flow induced particle migration in fresh concrete: Theoretical frame, numerical simulations and experimental results on model fluids. *Cement and Concrete Research*, 42(4):633 – 641, 2012.
- [4] J. Spangenberg, N. Roussel, J.H. Hattel, E.V. Sarmiento, G. Zirgulis, and M.R. Geiker. Patterns of gravity induced aggregate migration during casting of fluid concretes. *Cement and Concrete Research*, page Submitted, 2012.
- [5] J. Spangenberg, C.C. Tutum, J.H. Hattel, N. Roussel, and M.R. Geiker. Optimization of casting process parameters for homogeneous aggregate distribution in self-compacting concrete: A feasibility study. In *Evolutionary Computation (CEC), 2011 IEEE Congress on*, pages 2163 –2169, june 2011.
- [6] Xavier Chateau, Guillaume Ovarlez, and Kien Luu Trung. Homogenization approach to the behavior of suspensions of noncolloidal particles in yield stress fluids. *Journal of Rheology*, 52:489–506, 2008.
- [7] I.M. Krieger and T.J. Dougherty. A mechanism for non-newtonian flow in suspensions of rigid spheres. *Transactions of the society of rheology*, 3:137–152, 1959.
- [8] C.C. Tutum and J.H Hattel. *Multi-objective Evolutionary Optimisation for Product Design and Manufacturing*, chapter 3: State-of-the-art Multi-objective Optimisation of Manufacturing Processes Based on Thermomechanical Simulations. Springer, 2011.
- [9] K. Deb. *Multi-Objective Optimization using Evolutionary Algorithms*. John Wiley and Sons, Ltd, Chichester, UK, 2001.
- [10] C. C. Tutum. *Optimization of thermomechanical conditions in friction stir welding*. PhD thesis, Technical University of Denmark, 2009.
- [11] K. Deb, S. Agarwal, A. Pratap, and T. Meyarivan. A fast and elitist nondominated sorting genetic algorithm for multi-objective optimization: Nsga-ii. *IEEE Transactions on Evolutionary Computation*, 2002.

- [12] C.C. Tutum, K. Deb, and J. H. Hattel. Hybrid search for faster production and safer process conditions in friction stir welding. In *Proc. 8th Simulated Evolution and Learning (SEAL)*.